Reliability-Driven Experimental and Theoretical Study of Low-Frequency Noise Characteristics of AlGaN/GaN HFETs

Farzin Manouchehri

A Thesis

In the Department

of

Electrical and Computer Engineering

Presented in partial fulfillment of the degree requirements

For the Degree of

Doctor of Philosophy (Electrical and Computer Engineering) at

Concordia University

Montreal, Quebec, Canada

April 2014

© Farzin Manouchehri, 2014

CONCORDIA UNIVERSITY
SCHOOL OF GRADUATE STUDIES

This is to certify that the thesis prepared

By: Farzin Manouchehri

Entitled: Reliability-Driven Experimental and Theoretical Study of Low-Frequency Noise Characteristics of AlGaN/GaN HFETs

and submitted in partial fulfillment of the requirements for the degree of

DOCTOR OF PHILOSOPHY (Electrical and Computer Engineering)

complies with the regulations of the University and meets the accepted standards with respect to originality and quality.

Signed by the final examining committee:

Dr. Zezhong Chen	Chair
Dr. Zetian Mi	External Examiner
Dr. A. Ben Hamza	External to Program
Dr. Mojtaba Kahrizi	Examiner
Dr. Dongyu Qiu	Examiner
Dr. Pouya Valizadeh and Dr. M. Zahangir Kabir	Thesis Supervisor

Approved by

____
Chair of Department or Graduate Program Director

__________ ______________________________
Dean of Faculty

ABSTRACT

Reliability-Driven Experimental and Theoretical Study of Low-Frequency Noise Characteristics of AlGaN/GaN HFETs

Farzin Manouchehri, Concordia University, 2014

Silicon technology, which is the most mainstream semiconductor technology, poses serious limitations on fulfilling the market demands in high-frequency and high-power applications. In response to these limitations, wide bandgap III-nitride devices, including $Al_xGa_{1-x}N$/GaN heterojunction field effect transistors (HFETs), were introduced at about two decades ago to satisfy these rapidly growing market demands for high-power/high-frequency amplifiers and high-voltage/high-temperature switches. The most appealing features of III-nitride technologies, and particularly $Al_xGa_{1-x}N$/GaN HFETs, in these applications, are the polarization-induced high sheet-carrier-concentration, high breakdown-voltage, high electron saturation-velocity, and high maximum operating temperature. Therefore, the development of enhancement-mode AlGaN/GaN HFETs is one of the most important endeavours in the past two decades.

Low-frequency noise (LFN) spectroscopy, empowered by a proper physics-based model, is received as a capable tool for reliability studies. As a result, devising a physics-based LFN model for AlGaN/GaN HFETs can be capable of not only evaluating the alternative techniques proposed for realization of enhancement-mode AlGaN/GaN HFETs, but also more importantly forecasting the reliability, and noise performance of these devices.

In this dissertation, for the first time, a physics-based model for the low-frequency drain noise-current of AlGaN/GaN HFETs is proposed. The proposed model, through including the thermally-activated and quantum tunneling processes of trapping/de-trapping of electrons of channel into and out of the trap-sites located both in the barrier- and buffer-

layer of these HFETs, provides a descriptive picture for the LFN behavior of these devices. This work also aims to experimentally investigate the low-frequency noise-current characteristics of both conventional and newly-proposed devices (i.e., fin-, and island-isolated AlGaN/GaN HFETs) at various temperatures (i.e., 150, 300, and 450 K) and bias points in order to address the possible difficulties in performance of these devices. Matching of the trends proposed by the physics-based model to the experimentally recorded LFN spectra of AlGaN/GaN HFETs designed according to a newly-proposed technological variant for positive-shifting the threshold-voltage, confirms the accuracy and predicting power of the proposed model. The insights gained from this model on the latter group of devices provide evidence for the challenges of the aforementioned technological variants, and as a result offer assistance in proposing remedies for those challenges.

In formulating the LFN model, a massive discrepancy between the predictions of the existing analytical relationships used by others in evaluating the subband energy levels of AlGaN/GaN HFETs and the realities of the polarization-induced electron concentration of these HFETs was spotted. Careful evaluation of the polarization properties of these heterostructures unmasked the inaccuracy of the assumption of zero penetration of the electron wave into both the AlGaN barrier-layer and the GaN buffer-layer as the culprit in this discrepancy. In response to this observation, a model based on the variational-method for calculating the first and second subband energy levels of AlGaN/GaN HFETs is developed. On the basis of this model, more accurate analytical frameworks for calculating these subband energy levels in AlGaN/GaN HFETs for a variety of barrier thicknesses and Al mole-fractions in the barrier-layer are proposed.

Acknowledgment

Foremost, I would like to extend my deepest gratitude to my parents for their unconditional and ongoing support which has given me hope and courage to pursue my personal dreams and professional goals throughout my life. I am also indeed deeply grateful to my supervisors Dr. Pouya Valizadeh and Dr. M. Zahangir Kabir for their truly constructive supervision and enduring support during the course of my studies at Concordia University. Last but definitely not least, I would like to thank my committee members Dr. Zetian Mi, Prof. Mojtaba Kahrizi, Dr. Dongyu Qiu, and Dr. A. Ben Hamza for their helpful comments and instructions.

All the devices used in the experimental part of this research were fabricated by Canadian Microelectronics Corporation.

This research work was financially supported by the NSERC discovery grant program.

Contents

List of Figures viii
List of Tables xii
List of Symbols xiii
List of Abbreviations xvi
Chapter 1 1
Introduction 1
1.1 Overview of III-nitride technology 1
1.2 III-nitride semiconductor properties 4
1.3 AlGaN/GaN heterojunction field effect transistors 6
1.4 Research motivation 8
1.5 Proposed research objectives and framework 10
1.6 Thesis layout 11
1.7 List of publications 12
Chapter 2 14
Literature review and background theories 14
2.1 Crystal structures of III-nitrides 14
2.2 Epitaxial growth of III-nitride semiconductors 15
2.3 Challenges and difficulties of III-nitride technology 19
2.4 Polarization effect in III-nitrides 20
2.5 Polarization-induced two dimensional carrier concentration 23
2.6 Low-frequency noise in semiconductor devices 28
Chapter 3 35
Determination of the subband energy levels and the 2DEG characteristics of $Al_xGa_{1-x}N/GaN$ heterojunctions using variational method 35
3.1 Introduction 35
3.2 Theoretical model 37
3.3 Results and discussions 44
3.4 Conclusion 54

Chapter 4 55
Temperature-dependent investigation of low-frequency noise characteristics of Mesa-, Fin, and Island-Isolated AlGaN/GaN HFETs 55
4.1 Introduction 55
4.2 Device specifications and experimental setup 58
4.3 Experimental results and analysis 62
4.4 Conclusion 74
Chapter 5 76
Physics-based analysis of low-frequency drain noise-current in $Al_xGa_{1-x}N$/GaN HFETs 76
5.1 Introduction 76
5.2 Theoretical model 78
5.2.1 Carrier-concentrations in 2DEG 79
5.2.2 Low-frequency drain noise-current 83
5.2.2.1 Tunneling process 84
5.2.2.2 Thermally-activated process 86
5.3 Results and discussions 88
5.4 Conclusion 98
Chapter 6 99
Concluding remarks, contributions, and future work suggestions 99
6.1 Concluding remarks 100
6.2 Contributions 102
6.3 Future work suggestions 104
Bibliography 107

List of Figures

Figure 1.1 Comparison of GaN, GaAs, and Silicon FETs in high operating temperature, high-frequency, and high-power applications [7]. 4

Figure 1.2 A cross-sectional view of a typical polar AlGaN/GaN heterostructure (a) along with the associated conduction-band diagram at thermal equilibrium condition (b). A quantum well is created in the channel/buffer-layer and in the vicinity of the heterointerface. 7

Figure 2.1 The hexagonal close pack (hcp) lattice points. 15

Figure 2.2 Two-step growth using low-temperature GaN NL, (a) NL growth at low temperature, (b) NL growth during annealing, (c) NL when re-crystallized, (d) lateral 3D growth of islands, (e) coalescence of the islands, and (f) 2D step-flow growth, [27]....................................19

Figure 2.3 (Al)GaN crystalline structure in two different growth directions of Ga- and N-face. The direction of the spontaneous polarization vector depends on the crystal face [1], [6]. The positive direction is assumed to be from Ga (the metal) to the nearest N along the c axis. 21

Figure 2.4 Four different topologies of both Ga- and N-face AlGaN/GaN and inverted GaN/AlGaN heterostructures along with their associated directions of spontaneous and piezoelectric polarization vectors. 24

Figure 2.5 (a) A cross-sectional schematic of an AlGaN/GaN HFET. An overall polarization effect causes induction of a significant polar 2DEG at the heterointerface in GaN layer. As shown in this figure for the Ga-face AlGaN/GaN both piezoelectric (i.e., Ppz) and spontaneous polarization (i.e., Psp) vectors are in the same direction. (b) The conduction-band edge diagram of a heterojunction system without polarization effect, (for the case of AlGaAs/GaAs HFET show in dashed line and with polarization effect for the case of a polar AlGaN/GaN HFET show in solid line. Figures are not in scale....................................25

Figure 2.6 G-R Lorentzian power spectral density with the indication of corner frequency (f_c). 30

Figure 2.7 1/f noise as a result of the accumulative effect of the carrier Generation-Recombination Lorentzian profiles with a fairly dense distribution of

fluctuation time constants. The frequency exponent (i.e., γ) of the $1/f^{\gamma}$ spectrum is between 0 and 1.2. 32

Figure 3.1 Overall flowchart of the method used in the calculation of the first and second subband energy levels (E_0 and E_1), and Fermi level (E_F). 43

Figure 3.2 Calculated conduction-band diagram of a gated AlGaN/GaN heterostructure with Al mole-fraction of 0.3 and barrier thickness of 20 nm, at V_G = 0. Calculations are presented in terms of the variational method and the triangular quantum well approximation. 45

Figure 3.3 Variation of the first (solid line) and second (dashed line) subband energy levels (E_0 and E_1) and Fermi energy level E_F (dash-dotted line) with Al mole-fraction at V_G = 0. 47

Figure 3.4 (a) Variation of the first (solid line) and second (dashed line) subband energy levels (E_0 and E_1) and Fermi energy level E_F (dash-dotted line) with barrier thickness at V_G = 0 for Al mole-fractions of 0.2 and 0.3. (b) Variation of the 2DEG carrier concentration as a function of barrier thickness for Al mole-fractions of 0.1-1. 48

Figure 3.5 Comparison of the simulated 2DEG concentrations and experimental data obtained from [39] for AlGaN/GaN heterojunctions with barrier thickness (d_{AlGaN}) of 30 nm. The relaxation of the built-in strain in the barrier is not taken into account in the present model. 50

Figure 3.6 Variation of the Fermi level (dash-dotted line), first (solid line) and second (dashed line) subband energy levels with background donor concentration in an AlGaN/GaN heterojunction with Al mole-fraction of 0.2 and barrier thickness of 20 nm. 51

Figure 3.7 Variation of the 2DEG carrier concentration (dashed line), first (solid line) and second (dotted line) subband energy levels (E_0 and E_1), and Fermi energy level E_F (dash-dotted line) of a gated AlGaN/GaN heterojunction with gate voltage. 52

Figure 4.1 Scaled extrinsic gate transconductance versus gate voltage for three different device types of conventional mesa size (solid line), fin-isolated (dashed line), and island-isolated (dotted line) at room temperature, VDS is equal to 5 V [18]. 57

Figure 4.2 Three dimensional schematic of a conventional mesa-isolated device (a), a fin-isolated device (b), and an island-isolated device (c). Schematics illustrate

that a proportionally larger overlap exists between the gate and ohmic electrodes and the additionally etched surfaces in the island-isolated devices. In case of the island-isolated device, the schematic is showing only the connection to two of the islands. Drawings are not in scale. 59

Figure 4.3 Standard low frequency noise measurement setup. 61

Figure 4.4 Variation of the normalized drain noise-current level and frequency exponent (i.e., γ) at 10 Hz versus temperature for mesa-isolated (solid line), fin-isolated (dashed line), and island-isolated devices (dotted line) at two different bias points, V_{GS} = 0, V_{DS} = 0.4 V and V_{GS} = -2, V_{DS} = 0.4 V (a). Drain noise-current power spectral density is presented in (b)..63

Figure 4.5 (a) Variation of the normalized drain noise-current level at 10 Hz versus normalized effective gate-source voltage, at room temperature, for V_{GS} = 0, -1, and -2 V and V_{DS} = 0.4 V, for mesa- , fin- , and island-isolated devices. (b) Variation of the normalized drain noise-current level at 10 Hz versus normalized effective gate-source voltage, at 150 and 450 K for the same devices as (a). Mesa-, fin-, and island-isolated devices are represented by solid-, dashed-, and dotted-lines, respectively. 65

Figure 4.6 A comparison of room temperature drain noise-current spectral density among the three different device structures biased at V_{GS} = -1 V, V_{DS} = 0.2 V………………………………………………………………………...67

Figure 4.7 Drain noise-current level of the island-isolated HFET at 300, 350, 400, and 450 K. A G–R bulge signature is detected at room temperature. 68

Figure 4.8 Gate noise-current power spectral density of mesa-, fin-, and island-isolated devices at T = 150, 300, and 450 K at V_{GS} = -1 V and V_{DS} = 0.2 V (a). The normalized characteristics are presented in (b). 71

Figure 5.1 Cross-sectional view of a non-self-aligned polar AlGaN/GaN HFET. The lengths of gated-channel, source- and drain-access regions are identified as L_g, L_{gs}, and L_{gd}, respectively. 80

Figure 5.2 Overall flowchart indicating the method used in the calculation of the first and second subband energy levels (E_0 and E_1), Fermi level (E_F), threshold-voltage (V_T), and quasi Fermi level (i.e., E_{Fn}). These calculations are carried out before evaluation of low-frequency noise profile. Process P is repeated for all three regions of the channel under thermal equilibrium and non-thermal equilibrium according to the potential drop in each region. 82

Figure 5.3 (a) Calculated conduction-band diagram of an AlGaN/GaN heterojunction with indication of the first and second subband energy levels and (b) Comparison of the barrier seen by an impinging electron at relatively low and high frequency ranges in the tunneling model of the LFN. At very low frequencies (e.g., f <10 Hz) the height difference in conduction-band edge of the barrier becomes comparable to the barrier (e.g., $\Delta E_C - E_i$). 85

Figure 5.4 Hypothetical trap distributions in the barrier-layer (i.e., AlGaN) illustrating parabolic profiles as a function of energy with respect to the bottom of the conduction-band and distance with respect to the heterointerface. (a), (b) Parabolic trap distributions with a minimum and maximum value as a function of z and E, respectively. (c) Saddle-shape trap distribution as a function of z and E. 91

Figure 5.5 (a) Calculated LFN profiles according to the two processes of thermally-activated and tunneling. (b) Comparison of the simulation result (dashed-black line) and experimental data (red). Both figures belong to island-isolated device biased at V_{GS} = -1 V and V_{DS} = 0.2 V at room temperature.................92

Figure 5.6 Calculated LFN contribution of thermally-activated process at elevated temperatures (i.e., T = 350, 400, and 450 K). The device and bias point are the same as in Figure 5.5...93

Figure 5.7 Comparison of theoretically calculated LFN spectrum (dashed black line) and experimental drain noise-current spectrum of the island-isolated HFET biased at V_{GS} = -1 V and V_{DS} = 0.2 V, at elevated temperatures (i.e., T = 350, 400, and 450 K)...94

Figure 5.8 Comparison of the simulation results (dashed-black line) and experimental data (red) of drain noise-current at room temperature and two different bias points of V_{GS} = 0 V and -2 V with identical drain voltage of 0.2 V. All other parameters are the same as in Figure 5.5. 96

Figure 5.9 Calculated LFN contributions of the thermally-activated process at T = 300 (solid-blue), 350 (dotted-red), 400 (dashed-green), and 450 K (dashed-dotted purple) for the device biased at V_{GS} = -1 V and V_{DS} = 0.2 V. The calculations consider three different distribution functions for the buffer-layer trap levels…. 97

List of Tables

Table 1.1 Material properties of GaN and AlN at room temperature for two different crystalline forms of Wz and Zb [8]. 5

Table 3.1 The first and second subband energy levels as functions of 2DEG concentration, n_s (cm^{-2}), for different Al mole-fractions and barrier thicknesses. The functions are extracted through the interpolation of calculated values according to the proposed model. The spontaneous and piezoelectric constants used in these calculations are based on corrected values in [35]..53

Table 4.1 Summary of the criteria developed in [26] for determination of the dominant noise source S_R and dominant resistance along the channel R of a non-self-aligned FET. 68

Table 4.2 Reported values of trap levels due to ICP dry etching of the buffer-layer. 73

Table 4.3 Calculated time constants at 300 and 450 K based on the relaxation time constant at 150 K and relatively shallow trap levels. 73

List of Symbols

Symbol	Description	Unit (SI)
$\hbar$	Modified Planck's constant	Js
Δd_i	Average thickness of the i-th subband energy level	m
ΔE_C	Conduction-band offset	J
$\overline{\Delta N^2}$	Variance of the number of total trapped carriers	-
ϵ_0	Vacuum permittivity	F/m
λ	Standard deviation of the Gaussian trap distribution in the buffer layer	s
$\nu_0(T)$	Attempt-to-escape frequency	Hz
σ	Polarization-induced sheet charge density	C/m^2
τ	Fluctuation time constant	s
τ_0	Fluctuation time constant associated with the dominant trap level in the buffer-layer	s
τ_{th}	Fluctuation time constant associated with thermally-activated process	s
τ_{tn_i}	Fluctuation time constant associated with tunneling process	s
C_0	Capture coefficient	$m^{-3}s^{-1}$
C_i	Capture probability	-
D_{GaN}	2D GaN density of states	$J^{-1}m^{-2}$
e	Elementary charge	C
$e\varphi_b$	Schottky barrier height	J
E_0	First subband energy level of AlGaN/GaN heterojunction	J
E_1	Second subband energy level of AlGaN/GaN heterojunction	J

E_A	Activation energy of a trap level inside the buffer layer	J
E_{C-GaN}	Conduction-band edge of GaN	J
E_F	Fermi energy level	J
E_{Ft}	Quasi Fermi energy level of a trap center	J
Eg	Bandgap energy	J
E_{V-GaN}	Valence-band edge of GaN	J
f	Frequency	Hz
h	Planck's constant	Js
I_D	DC Drain current	A
k	Boltzmann constant	J/K
L_g	Gate length	m
L_{gd}	Gate-drain separation	m
L_{gs}	Gate-source separation	m
m_0	Mass of a free electron	Kg
m^*_{AlGaN}	Effective electron mass in AlGaN	Kg
m^*_{GaN}	Effective electron mass in GaN	Kg
N	Total number of carriers inside the channel	-
$N_{C(AlGaN)}$	Effective AlGaN density of states at the conduction band edge	m^{-3}
N_D	Background dopant concentration of the buffer layer	m^{-3}
n_i	Intrinsic carrier-concentration	m^{-3}
n_s	Two dimensional electron gas (2DEG) concentration	m^{-2}
N_{t-th}	2D trap density	m^{-2}
N_{T-tn}	Trap density of states inside the barrier-layer	$J^{-1}m^{-3}$

$\boldsymbol{P}_{\mathrm{PZ}}$	Piezoelectric polarization vector	C/m^2
$\boldsymbol{P}_{\mathrm{SP}}$	Spontaneous polarization vector	C/m^2
$\boldsymbol{P}_{\mathrm{tot}}$	Total polarization vector	C/m^2
S_{I-TH}	Noise power spectral density due to thermally-activated process	A^2/Hz
S_{I-TN}	Noise power spectral density due to tunneling process	A^2/Hz
T	Absolute temperature	K
V_{DS}	Drain-source voltage	V
V_{GS}	Gate-source voltage	V
V_{T}	Threshold-voltage	V
W	Effective gate width	m
x	Al mole-fraction	-

List of Abbreviations

Abbreviation	Description
2DEG	Two dimensional electron gas
DOS	Density of states
G-R	Generation-recombination
HBT	Heterojunction bipolar transistor
HCP	Hexagonal close pack
HFET	Heterojunction field effect transistor
HNPS	High nitrogen pressure solution
HR	High resistivity
HVPE	Hydride vapor phase epitaxy
ICP	Inductively coupled plasma
LFN	Low-frequency noise
LNA	Low-noise amplifier
MBE	Molecular beam epitaxy
MOCVD	Metal-organic chemical vapor deposition
MOSFET	Metal oxide semiconductor field effect transistor
PSD	Power spectral density
RF	Radio frequency
RHEED	Reflection high-energy electron diffraction
RIE	Reactive ion etching
RMS	Root mean square

SI	Semi insulating
UHV	Ultra high vacuum
VCO	Voltage-controlled oscillator
Wz	Wurtzite
Zb	Zinc-blende

Chapter 1

Introduction

1.1 Overview of III-nitride technology

Semiconductor science and technology have been continuously expanding at a stunning pace over the past few decades. Whereas silicon, and to a lesser degree a few other semiconductor contenders such as GaAs, have managed to furnish the required media for this expansion, fundamental limitations of these materials up until recently had halted the expansion of semiconductor electronics into markets such as base-stations of mobile telecommunication systems (needing very high power levels at relatively high frequencies), and also efficient incorporation of electronic control circuitry in high-temperature environments such as under the hood of hybrid vehicles [1], [2]. It had been in light of these unfulfilled demands that at about two decades ago intensive research on

wide bandgap III-nitride technology gained momentum. The wider bandgap of many of the semiconductors belonging to this family compared to the other main semiconductor contenders, and also their superb polarization and charge transport properties have gained this group of semiconductors sufficient traction to make strong promises for fulfilling the aforementioned market demands. Whereas an intensive research over the past two decades has successfully delivered some of these promises, work in a number of other fronts, including reliability, is still in progress.

Although lack of a native substrate, aggravated the usual crystal growth problems at the early stages of research on III-nitride compound semiconductors (i.e., AlN, GaN, InN, and their alloys), improved understanding of the crystal growth problems of these semiconductors and their heterostructures has been continuously resulting in reduction of their originally forbiddingly high levels of dislocation density to the levels affordable in device fabrication [3]. As a result of these improvements, III-nitride devices have been commercialized in both optoelectronics and high-frequency/high-power electronic applications. For instance, GaN-based power devices have been commercialized by a good number of industry leaders such as TriQuint Semiconductor Inc. for typical applications including avionics, civilian/military radar, professional/military radio, and test instrumentation. TriQuint Inc. has commercialized discrete GaN-based transistors including a 90 W device with operating frequency range between DC and 18 GHz (for broadband wireless and military applications) and an 18 W device with operating frequency range between DC and 6 GHz (for civilian/military radar, general purpose of radio frequency (RF) power, and test instrumentation applications) [4].

Besides the wider bandgap, the other key features of III-nitride semiconductors that make them superior to the mainstream III-V technology of GaAs are their very strong spontaneous and piezoelectric polarizations [5], [6], which will be further discussed in chapter 2. From a device stand-point, the most tangible effect of these polarization components is the induction of a large sheet-carrier-concentration at III-nitride heterointerfaces, even in the absence of intentional doping. Such a mechanism of charge induction offers the channel of field effect transistors, realized in this technology, an electron concentration at least an order of magnitude stronger than the other contenders. In case of GaN channel, this high electron concentration in conjunction with the superb saturation-velocity and the broader peak electron velocity yields drain current-densities exceeding 1 A/mm (i.e., per millimeter width of the field effect transistor), and considerable gain at microwave frequencies.

On the basis of these unique properties, as illustrated in Figure 1.1, comparison between GaN and the two main semiconductor contenders (i.e., Si and GaAs) demonstrate the operation of GaN transistors to be superior from the viewpoint of a number of important device properties including operating temperature, breakdown field, maximum current-density, noise-figure, and maximum oscillation-frequency.

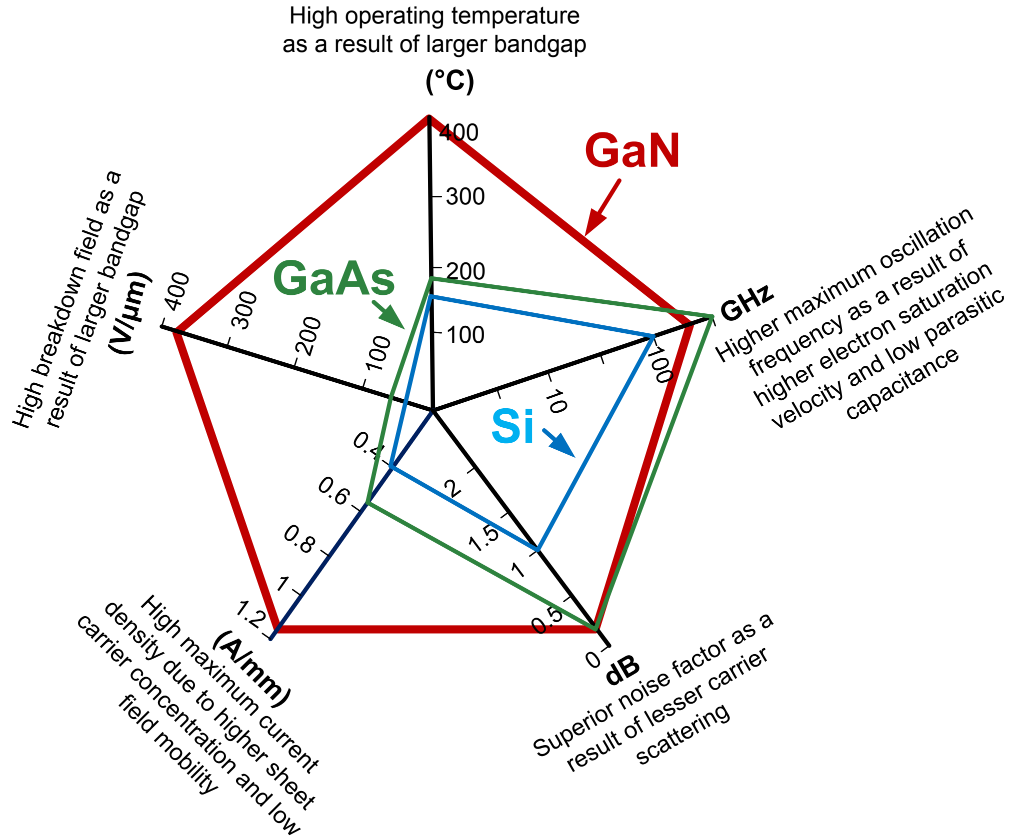

Figure 1.1 Comparison of GaN, GaAs, and Silicon FETs in high operating temperature, high-frequency, and high-power applications [7].

1.2 III-nitride semiconductor properties

III-nitride semiconductors can be grown in two different crystalline forms of hexagonal Wurtzite (Wz) and cubic Zinc-blende (Zb). However, the aforementioned polarization properties of III-nitride semiconductors are attributed to their Wz crystalline form. As a result, this is the crystalline form in which many of the devices realized in this technology have been materialized. The heterojunction field effect transistors (HFETs), realized in this crystalline form, are often referred to as polar HFETs.

Table 1.1 provides a list of important properties of GaN (in both crystalline forms) and AlN (in the Wz form), which are pivotal to understanding the behavior of electronic devices realized in this technology.

Table 1.1 Material properties of GaN and AlN at room temperature for two different crystalline forms of Wz and Zb [8].

	GaN		**AlN**
	Wz	**Zb**	**Wz**
Number of atoms in cm^3	8.9×10^{22}	8.9×10^{22}	9.58×10^{22}
Debye temperature (K)	600	600	1150
Density (g/cm^3)	6.15	6.15	3.23
Dielectric constant (static)	8.9	9.7	8.5
Dielectric constant (high frequency)	5.35	5.3	4.6
Effective electron mass ($\times m_0$)	0.2	0.13	0.4
Electron affinity (eV)	4.1	4.1	0.6
Lattice constant (Å)	a = 3.189 c = 5.186	4.52	a = 3.112 c = 4.982
Optical phonon energy (meV)	91.2	87.3	99
Bandgap (eV)	3.39	3.2	6.2
Effective conduction-band density of states (cm^{-3})	2.3×10^{18}	1.2×10^{18}	6.3×10^{18}
Effective valence-band density of states (cm^{-3})	4.6×10^{19}	4.1×10^{19}	4.8×10^{20}
Breakdown field ($V\ cm^{-1}$)	$\sim 5 \times 10^6$	$\sim 5 \times 10^6$	$(1.2 - 1.8) \times 10^6$
Electron low-field mobility ($cm^2V^{-1}s^{-1}$)	≤ 1000	≤ 1000	300
Hole low-field mobility ($cm^2V^{-1}s^{-1}$)	≤ 200	≤ 350	14
Electron diffusion coefficient (cm^2s^{-1})	25	25	7
Hole diffusion coefficient (cm^2s^{-1})	5	9	0.3
Electron thermal velocity (ms^{-1})	2.6×10^5	3.2×10^5	1.85×10^5
Hole thermal velocity (ms^{-1})	9.4×10^4	9.5×10^4	0.41×10^5
Thermal conductivity ($W\ cm^{-1}\ C^{-1}$)	1.3	1.3	2.85

1.3 AlGaN/GaN heterojunction field effect transistors

As discussed earlier, a combination of factors including high operating temperature, large critical electric-field, high electron saturation-velocity, and high sheet-carrier-concentration have made polar AlGaN/GaN heterojunction field effect transistor a suitable candidate for microwave and power electronic applications [9], [10].

Polar $Al_xGa_{1-x}N$/GaN heterojunctions are often formed by the pseudomorphic growth of a wider bandgap barrier-layer (i.e., $Al_xGa_{1-x}N$) on top of a narrower bandgap channel/buffer-layer (i.e., GaN). In these heterostructures, the difference between the energy bandgaps of the barrier- and buffer-layer results in creation of a quantum well on the channel/buffer side of the heterointerface. Presence of this potential well normally yields an almost two-dimensional electron gas (2DEG) concentration or a sheet of electrons, within this quantum well. It is worth noting that the quantum well characteristics of these polar heterojunctions, in contrast to their non-polar counterparts such as $Al_xGa_{1-x}As$/GaAs heterojunctions, in addition to bandgap discontinuity (which is variable with the Al mole-fraction of the barrier-layer: x), and doping level of the barrier, are also functions of polarization fields. In pseudomorphically grown $Al_xGa_{1-x}N$/GaN heterostructures, the considerable built-in strain along with the large piezoelectric coefficients causes a sizeable piezoelectric polarization effect. The combination of this large piezoelectric polarization and the existence of a large discontinuity of the so-called spontaneous polarizations built into the barrier- and the buffer-layer at the heterointerface, induces a high sheet-carrier-concentration (i.e., in the order of 10^{13} cm^{-2}) at the GaN side of the heterojunction [6]. This discussion is further elaborated in chapters 2 and 3.

Figure 1.2 illustrates a cross-sectional view of a typical polar AlGaN/GaN heterostructure along with the associated conduction-band diagram drawn under the thermal equilibrium condition. The indicated positions of the Fermi energy level, first and second subband energy levels in this figure are purely qualitative.

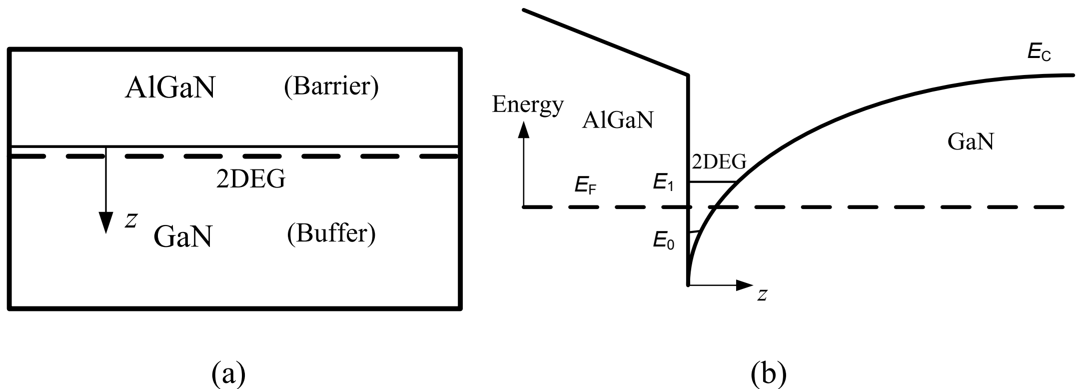

Figure 1.2 A cross-sectional view of a typical polar AlGaN/GaN heterostructure (a) along with the associated conduction-band diagram at thermal equilibrium condition (b). A quantum well is created in the channel/buffer-layer and in the vicinity of the heterointerface.

On a heterostructure such as the one depicted in Fig. 1.2 (a), HFETs are realized through devising source and drain ohmic contacts to the 2DEG, while the depleting effect of a blocking Schottky contact formed to the barrier-layer serves to modify this inherently high-concentration polarization-induced sheet of charge, and as a result channel's conductivity between the two ohmic contacts. Whereas metals of large work-function such as Ni or Pt are used for realization of the blocking characteristics of the gate, use of Ti as the ohmic metal and application of high annealing temperatures (in a rapid thermal annealing context) produce the ohmic contacts to the 2DEG. The ohmic contact formation takes place through forming a conductive alloy within the thickness of the barrier-layer.

While the inherent induction of a high 2DEG concentration on the GaN side of the AlGaN/GaN heterointerface results in a high maximum drain-current density, the same character makes the realization of normally-off HFETs (i.e., a type of HFET in which the creation of the channel between the drain and source is only possible after applying a positive voltage to the gate terminal) very difficult [11], [12]. Because of its ideally zero standby-power consumption, normally-off operation is extremely important to commercialization of any FET technology.

Aimed at achieving normally-off mode of operation, over the past few years a number of different techniques have been introduced to shift the normally negative threshold-voltages (V_T) of AlGaN/GaN HFETs in the positive direction [11] - [18].

1.4 Research motivation

Although understanding the behavior of AlGaN/GaN HFETs requires an accurate evaluation of the subband energy levels formed at the AlGaN/GaN heterointerfaces, and the band-diagram of these heterostructures, so far only a limited amount of work has been presented in this area [19] - [22]. Whereas some of the presented calculations are based on the triangular quantum well approximation, which is often acceptable in non-polar HFETs, due to enhanced conduction-band bending of polar AlGaN/GaN HFETs, this approximation has been observed to result in erroneous evaluation of specially second subband energy level [19], [20]. In the meanwhile, other more sophisticated frameworks such as self-consistent and variational methods have been also applied for evaluation of 2DEG characteristics of these heterostructures [21], [22]. These reports are, however, limited to a specific heterostructure (i.e., of a given Al mole-fraction and thickness of the

barrier-layer). The reported evaluation based on the variational method is even more limited, since it only addresses the calculation of the first subband energy level [22]. Due to the large electron population of 2DEG channel in polar AlGaN/GaN HFETs, and the consequent chance of populating the second subband energy level, this is quite limiting from a device engineering perspective.

Polarization, and as a result, Al mole-fraction and thickness of the barrier, are of prime importance in charge-induction and conduction-band bending in the channel of AlGaN/GaN HFETs. Therefore, without a mathematically manageable and yet extendable framework of calculation for evaluating the conduction-band diagram and the first two subband energy levels for all different possibilities of these heterostructure, general evaluation of device characteristics would not be possible.

Among the device characterization techniques that will suffer in absence of such a model is low-frequency noise (LFN) spectroscopy. This characterization technique has been shown to be very suitable for reliability characterization of many electronic devices including HFETs [23] - [26]. Although even on a purely experimental basis, through comparison of the low-frequency noise of different devices, signatures of reliability concerns can be evaluated, assessment of the roots of these concerns is possible only in presence of a physics-based low-frequency noise model. Such a possibility is extremely important for not only reliability assessment of a technology in development, such as AlGaN/GaN HFET, but also evaluation of the noise limits in performance of these transistors. In spite of availability of physics-based low-frequency noise models for other FET technologies, in presence of polarization in AlGaN/GaN HFETs, these models are not readily extendable to these devices. As new variants of AlGaN/GaN HFET

technology for realization of normally-off mode of operation, and subsequently commercialization of this technology, are gaining traction, absence of this theoretical foundation is further coming into the spotlight.

1.5 Proposed research objectives and framework

In accordance with the discussions of section 1.4, the objectives of this PhD research were set based on the dire absence of proper physics-based insight into the 2DEG characteristics of gated AlGaN/GaN heterojunctions and low-frequency noise properties of charge transport through these channels.

In terms of the prior discussions of section 1.4, it has been the intention of this work to propose and present a complete analytical method for calculating the 2DEG characteristics of gated AlGaN/GaN heterojunctions, including first and second subband energy levels for various Al mole-fractions, barrier thicknesses, background dopant concentrations, and gate voltages.

The developed model has been planned to serve as the backbone of a new physics-based low- frequency noise model for drain-current of AlGaN/GaN HFETs. Based on prior evaluation of the applicable noise theory (i.e., the number-fluctuation noise theory), in this model noise is evaluated through assessing the fluctuation time constants of both the thermal trapping/de-trapping and the tunneling processes to trap-sites within the buffer- and barrier-layer.

The research tasks are categorized as follows,

- Determination of subband energy levels and quantum well characteristics of $Al_xGa_{1-x}N$/GaN heterojunctions using the variational method. The physics-based model

developed in this research follows a generic approach, which can also be applied to other III-nitride technologies. This model is considered as the backbone of theoretical modeling of low-frequency noise.

- Proposition of closed-form relationships between the first and second subband energy levels and 2DEG concentrations for different Al mole-fractions and barrier thicknesses. The proposed empirical expressions can be used in faster modeling of different device characteristics.
- Evaluation and comparison of the possible reliability issues in conventional mesa-isolated AlGaN/GaN HFETs and two newly-proposed variants for modifying the threshold-voltage (i.e., fin-, and island-isolated AlGaN/GaN HFETs). This is accomplished through low-frequency noise spectroscopy under different bias conditions and substrate temperatures.
- Physics-based modeling of the low-frequency drain noise-current characteristics, assessment of variation in noise with bias and substrate temperature, identifying the culprits in generation-recombination bulge signatures, and proposing possible remedies.

1.6 Thesis layout

This thesis is organized into six chapters. Following the introduction (chapter one), literature review and background theories related to GaN crystalline structures, polarization effects in III-nitrides, and low-frequency noise are presented in chapter 2.

Chapter 3 presents the proposed variational model for evaluation of 2DEG characteristics of AlGaN/GaN HFET.

Chapter 4 is dedicated to temperature-dependent experimental investigation of low-frequency noise-current characteristics of the three aforementioned device types (i.e., mesa-, fin, and island-isolated AlGaN/GaN HFETs).

The proposed model for low-frequency drain noise-current characteristics of AlGaN/GaN HFETs according to the number-fluctuation noise theory is presented in chapter 5.

Chapter 6 is devoted to concluding remarks and contributions of this thesis, as well as suggested future works.

1.7 List of publications

The research work of this thesis has resulted in the following publications,

Peer Reviewed Journal Papers,

1. F. Manouchehri, P. Valizadeh, and M. Z. Kabir, "Temperature-dependent investigation of low frequency noise characteristics of mesa-, fin-, and island-isolated AlGaN/GaN HFETs," *Solid-State Electronics*, vol. 89, pp. 1-6, Nov. 2013.

2. F. Manouchehri, P. Valizadeh, and M. Z. Kabir, "Physics-based analysis of low frequency drain noise-current in $Al_xGa_{1-x}N$/GaN HFETs," *J. Phys. D: Appl. Phys.*, vol. 47, pp. 085104-1–085104-8, Feb. 2014.

3. F. Manouchehri, P. Valizadeh, and M. Z. Kabir, "Determination of subband energies and 2DEG characteristics of $Al_xGa_{1-x}N$/GaN heterojunctions using variational method," *J. Vac. Sci. and Technol. A.*, vol. 32, no. 2, pp. 021104-1–021104-8, Mar. 2014.

Peer Reviewed Conference Papers,

1. F. Manouchehri, P. Valizadeh, and M. Z. Kabir, "Non-fundamental low frequency noise theory: Drain noise-current modeling of AlGaN/GaN HFETs," *Proc.21st Int. Conf. Noise and Fluctuations (ICNF)*, June 2011.

2. F. Manouchehri, P. Valizadeh, and M. Z. Kabir, "Low Frequency Drain Noise Characteristics of Polarization-Engineered AlGaN/GaN HFETs," *Int. Conf. Electron Devices and Solid-State Circuits*, June 2013.

3. F. Manouchehri, P. Valizadeh, and M. Z. Kabir, "Experimental and Theoretical Study of Low Frequency Drain Noise-Current Characteristics of AlGaN/GaN HFETs," *Canadian Semiconductor Sci. and Technol. Conf.*, Aug. 2013.

Chapter 2

Literature review and background theories

2.1 Crystal structures of III-nitrides

III-nitride semiconductors including GaN, AlN, InN, and their alloys, are capable of taking-on either Wurtzite or Zinc-blende crystal structures. However, in electronic applications, III-nitride semiconductors are predominantly grown in Wurtzite crystalline form. The Wurtzite crystal structure is a hexagonal close pack structure (i.e., hcp) with a two-atom basis [1]. Figure 2.1 illustrates the arrangement of lattice points in an hcp lattice. The lattice vectors in this figure are shown by **a**, **b**, and **c**. The hcp structure is constructed in terms of two inter-penetrating anion and cation hexagonal sub-lattices with a displacement of **a**/3, **b**/3, and **c**/2, where **a**, **b**, and **c** are the lattice vectors. In a

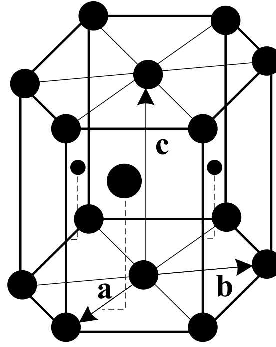

Figure 2.1 The hexagonal close pack (hcp) lattice points.

maximally-packed hcp structure, c/a = $\sqrt{8/3}$ [1], where c is the height of the hexagonal prism and a is the lattice constant of the basal hexagon.

2.2 Epitaxial growth of III-nitride semiconductors

Growth of a crystalline over-layer on a crystalline substrate is known as epitaxial growth. Epitaxial semiconductor growth techniques including metal-organic chemical vapor deposition (MOCVD) and molecular beam epitaxy (MBE) grant atomic-scale control over the growth process, and essentially a sharp interface between the two crystals [1]. Applying these techniques, one can grow junctions between two different semiconductors, which are generally-speaking known as heterojunctions or heterostructures. In case of an AlGaN/GaN heterojunction, caused by the band lineup of AlGaN and GaN, a quantum well is formed on the conduction band of the GaN-side of the heterointerface. In this quantum well, electrons will be confined by the conduction band discontinuity between the smaller bandgap semiconductor (i.e., GaN) and the wide bandgap semiconductor (i.e., AlGaN which is known as the barrier in this heterostructure). In this heterostructure, Al mole-fraction of the III-nitride ternary alloy

(i.e., $Al_xGa_{1-x}N$) and the barrier thickness can be precisely controlled throughout the epitaxial growth. These properties directly influence the electron concentration of the quantum well formed at the heterointerface.

The MOCVD growth system enjoys a simple reactor structure, which does not require an ultra-high vacuum (UHV) condition. The UHV condition, however, is essential to the MBE growth process. Between MBE and MOCVD, the latter has been reported to be the more popular approach in growing III–nitride-based layers such as heterojunction field effect transistors (HFETs) and hetero-junction bipolar transistors (HBTs) [27]. The MOCVD technique operates based on the transportation of gas phase hydrides, metal-organics, and carrier gasses to a substrate kept at very high temperature. The metal-organic precursors used for epitaxial growth of Ga (Al, In)-nitrides are usually liquid sources of Tri-Methyl-Gallium (Aluminum), TMGa (Al), and solid source of Tri-Methyl-Indium (TMIn). As for the nitride precursor, high purity NH_3 (ammonia) is normally used. A carrier gas (hydrogen or nitrogen) is used to transport the metal-organic vapor to the heated substrate. This is done by passing the carrier gas through the liquid/solid metal-organic sources. A significant difference between ammonia and other group V precursors (e.g., PH_3, AsH_3) is its relatively higher bond energy, which leads to a lower decomposition efficiency of ammonia [27]. Therefore, in MOCVD technique, higher growth temperatures (~ 1100 °C) for the growth of III-nitrides are required.

One of the essential requirements of an MBE system is a pure and large material source, which can be used in generating the molecular beam. As mentioned earlier, in conjunction with the formation of the molecular beam, the MBE process is implemented in an ultra high vacuum environment (~10^{-8} Pa). Slow growth rate of MBE allows very

high quality epitaxial growth of semiconductor layers. It should be noted that in the case of the MBE growth technique, relatively lower temperatures are required. This is especially important to epitaxial growth of InN and its alloys, which have a high tendency of losing In at high temperatures.

In-situ monitoring techniques are often used in both MOCVD and MBE growth systems to examine the surface of the growing wafer. A key advantage of MBE technique is the use of in-situ reflection high energy electron diffraction (RHEED) to control the growth process in real time [28].

The growth process of GaN layers suffers from the lack of a commercially-available large native GaN substrate, to yield unstrained latticed-matched growth. In absence of a lattice-matched substrate, so far SiC and sapphire substrates, with drastically different crystalline structures to GaN, have been adopted. In order to minimize the crystal imperfections created in III-nitride epitaxial layers grown on these non-native substrates, low-temperature growth of a thin nucleation layer (NL), in the order of a few nanometers, is required [27], [29]. For fully understanding the significance of the NL, the study of different modes of epitaxy is necessary.

Crystal growth can be categorized into three different modes: Three dimensional (3D, Volmer-Webber), Two dimensional (2D, Frank-van der Merwe), and 2D-to-3D (Stranski-Krastanov) [29]. In 3D growth mode, island-like structures are grown on the substrate. This is due to the weaker bond between the substrate and the growing crystal, compared to the bond strength within this crystal. This mode of epitaxy occurs when the substrate and the growing crystal are highly lattice-mismatched. As opposed to the 3D growth, the 2D growth occurs when strong bonds exist between the atoms of the substrate and the

growing layer. In this case, the incoming atoms “wet” the substrate (i.e., spread across the substrate). Finally, the 2D-to-3D mode occurs when the growing layer tends to release its strain energy due to the existing lattice mismatch [27].

As the lattice mismatch between GaN and sapphire is about 14%, the growth mode is normally 3D [29]. However, in realization of HFET epilayers[1], the 2D growth is the required mode of crystal growth. The transformation from the 3D to the 2D mode is done through a two-step growth. At first, a very thin nucleation layer of GaN or AlN (20-30 nm) is grown on the substrate. This growth is performed at a low-temperature of about 500 °C (Figure 2.2(a)). The reason behind using the low-temperature growth at this stage of growing the NL is that, at reduced temperatures, the degradation in the diffusion constant makes the atoms stick to the point that they have landed on. In this stage, the NL consists of cubic GaN crystals. After growing the NL, the temperature is ramped up to temperatures needed for growing a more hexagonal type of GaN crystal, which is about 1000 to 1100 °C (Figure 2.2(b)). Figure 2.2 (c) illustrates the growth results with an optimized condition, where islands of nucleation sites at a high density are grown on the substrate. These island-like structures ideally possess hexagonal GaN crystal structures. After growing discrete islands on the substrate, incoming Ga and N will “observe” a natural GaN template to grow a crystal on. Therefore, these islands will start to grow vertically as well as laterally (Figure 2.2 (d)). Afterwards, the islands begin to coalesce (Figure 2.2 (e)) and the growth switches to the 2D mode (Figure 2.2(f)).

[1] Epitaxial-Layers

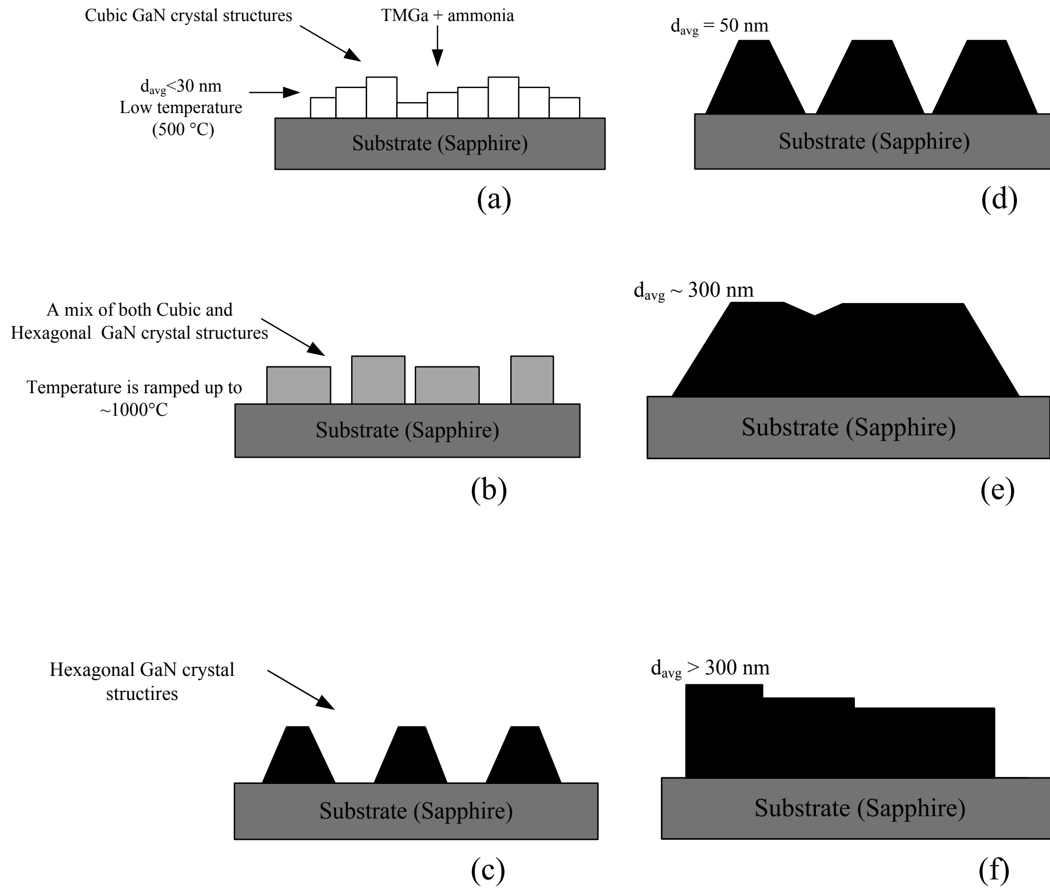

Figure 2.2 Two-step growth using low-temperature GaN NL, (a) NL growth at low temperature, (b) NL growth during annealing, (c) NL when re-crystallized, (d) lateral 3D growth of islands, (e) coalescence of the islands, and (f) 2D step-flow growth, [27].

2.3 Challenges and difficulties of III-nitride technology

Despite the considerable improvement in growth techniques of III-nitride compound semiconductors, these growth processes are still plagued by a large number of difficulties. One of the most important signs of these difficulties is the presence of a relatively high unintentional n-type background dopant concentration (in the range of 10^{14}-10^{16} cm^{-3}) [1].

Whereas high-resistivity (HR) GaN layers are vital to maintaining proper current saturation characteristic in HFETs, low cross-talk between two neighboring devices, and complete channel pinch-off [30], as pointed out earlier in this section, GaN layers are unintentionally n-type doped. This unintentional doping is deemed to be the result of the presence of oxygen or water vapor contamination, and defects propagating from the NL [30], [31]. There are two most accepted methods in achieving compensated high resistivity GaN epilayers. The first method relies on compensating the unintentional donors with intentional introduction of acceptors such as Fe or Cr impurities. The second approach is based on tuning the growth parameters such as NL thickness, final NL annealing temperature, annealing pressure of the NL, etc. [30], [32].

The inhibitingly high melting temperature of GaN (2500 °C) can be correctly identified as the culprit in many of these substrate-related difficulties. A novel GaN crystal growth technique has been shown by Bockowski et al. [33]. In this technique, 2-inch 1-mm thick HVPE[2]-GaN crystals (which are mechanically and machano-chemically polished to free-standing crystals) are used as seeds in a multi feed-seed crucible of HNPS[3] system. A recent result of this method has been reported to produce high quality GaN substrates with dislocation densities of about 5×10^5 cm^{-2} [34].

2.4 Polarization effect in III-nitrides

As mentioned earlier in chapter 1, in addition to the wide bandgap, strong polarization effect is one of the appealing features of III-nitride semiconductors. Unstrained III-nitride semiconductors can exhibit net polarization due to a shift between the anion and cation

[2] Hydride vapor phase epitaxy
[3] High nitrogen pressure solution

sub-lattices. The shift between anion and cation sub-lattices only exists in Wz crystalline structure, as opposed to Zb crystalline structure. These spontaneously-induced polarizations in III-nitride semiconductors which are represented by the spontaneous polarization vectors ($\boldsymbol{P}_{SP}$) are important to III-nitride heterojunctions and associated devices (e.g., HFETs) [1], [6]. The magnitudes of these spontaneous polarization vectors have been evaluated to be considerably larger than other semiconductors. This magnitude increases from GaN to InN, and to AlN [6].

Wurtzite GaN crystalline structure can be grown along two different growth directions known as [0001] and [000$\bar{1}$], which are also referred to as Ga- (metal) and N-face, respectively. The most common growth direction of AlGaN/GaN material systems is the Ga-face. It is note-worthy that in defining the orientations of the polarization vector, the positive direction is defined from the metal (Ga) to the nearest nitrogen atom along the c-axis. In addition, the sign of the spontaneous polarization for group III-V semiconductors

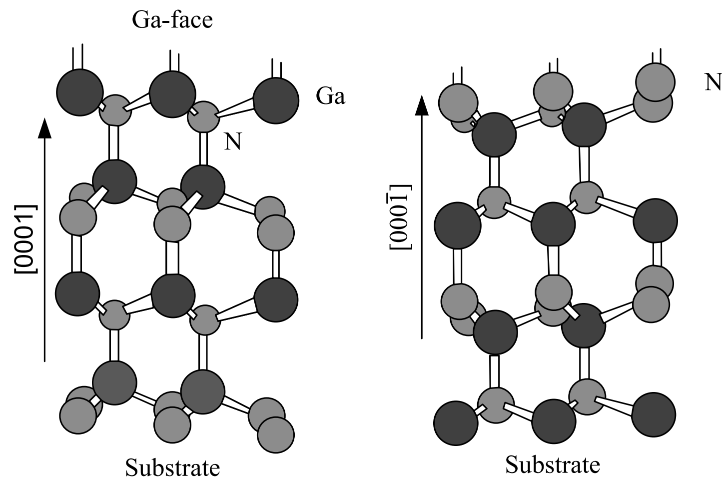

Figure 2.3 (Al)GaN crystalline structure in two different growth directions of Ga- and N-face. The direction of the spontaneous polarization vector depends on the crystal face [1], [6]. The positive direction is assumed to be from Ga (the metal) to the nearest N along the c axis.

is found to be negative and therefore, the direction of this polarization is from N to the nearest Ga atom. This direction can be determined by the crystal face.

For the Ga(Al)-face layers, the orientation of spontaneous polarization is from top to bottom whereas this orientation is from bottom to top for the N-face layers. These directions are illustrated in Figure 2.3.

The spontaneous polarization vectors for III-nitrides have been characterized by different methods and tabulated in previously published studies [6], [35]. For ternary alloys (e.g., AlGaN), spontaneous polarization can be calculated using the law of weighted averaging (also known as Vegard's law). The application of Vegard's law in calculation of spontaneous polarization of III-nitride alloys is allowed only if a linear behavior of spontaneous polarization is admissible. The non-linear behavior of the spontaneous polarization is elaborated in section 2.5.

In addition to the spontaneous polarization, a piezoelectric polarization effect is also observed in pseudomorphic Wz III-nitride heterostructures. In particular, for the case of pseudomorphically grown AlGaN barrier-layer on GaN buffer-layer, the considerable piezoelectric polarization of the strained barrier-layer (i.e., AlGaN) is more than five times that of AlGaAs/GaAs heterostructures [6]. The piezoelectric polarization is the result of the mismatch between lattice constants of the barrier- and buffer-layer. It is shown that both spontaneous and piezoelectric polarization vectors (i.e., $\boldsymbol{P}_{SP}$ and $\boldsymbol{P}_{PZ}$, respectively) have a significant influence on the 2DEG characteristics of Wz III-nitride semiconductor heterostructures [36] - [38].

2.5 Polarization-induced two dimensional carrier concentration

As mentioned in section 2.1, the Wurtzite crystalline structure is identified through the edge length a_0, the height of the hexagonal prism c_0, and a dimensionless parameter u in units of c_0 defined as the length of the cation-anion bond parallel to [0001]. The piezoelectric tensor in Wz III-nitride semiconductors possesses three non-vanishing independent elements. Two of these three tensor elements quantify the piezoelectric polarization vector ($\boldsymbol{P}_{PZ}$), which is induced normal to the basal plane and along [0001] direction. This vector, in terms of these elements is quantified as,

$$P_{PZ} = e_{33}\epsilon_z + e_{31}(\epsilon_x + \epsilon_y) \tag{2.1}$$

where e_{33} and $e_{31}$are the piezoelectric coefficients, ϵ_z is the strain along the c axis defined as $\frac{c-c_0}{c_0}$, ϵ_x and ϵ_y are the isotropic in-plane strains defined as $\frac{a-a_0}{a_0}$, (where, a and c are lattice constants of the substrate) [6]. It is note-worthy that the strain tensor is dependent on the mole-fraction in a ternary III-nitride alloy. The relationship between the lattice constants in AlGaN/GaN system is defined by,

$$\frac{c-c_0}{c_0} = -2\frac{C_{13}}{C_{33}}\frac{a-a_0}{a_0} \tag{2.2}$$

where C_{13} and C_{33} are elastic constants. Combining equations (2.1) and (2.2), the piezoelectric polarization along the c axis is expressed as,

$$P_{PZ} = 2\frac{a-a_0}{a_0}(e_{31} - e_{33}\frac{C_{13}}{C_{33}}) \tag{2.3}$$

The direction of the piezoelectric polarization vector depends on both the crystal face (Ga- and N-face) and the sequence of epilayers (i.e., barrier- and buffer-layers grown on a relaxed substrate). Four different topologies of Ga- and N-face AlGaN/GaN and inverted GaN/AlGaN heterostructures along with their associated directions of

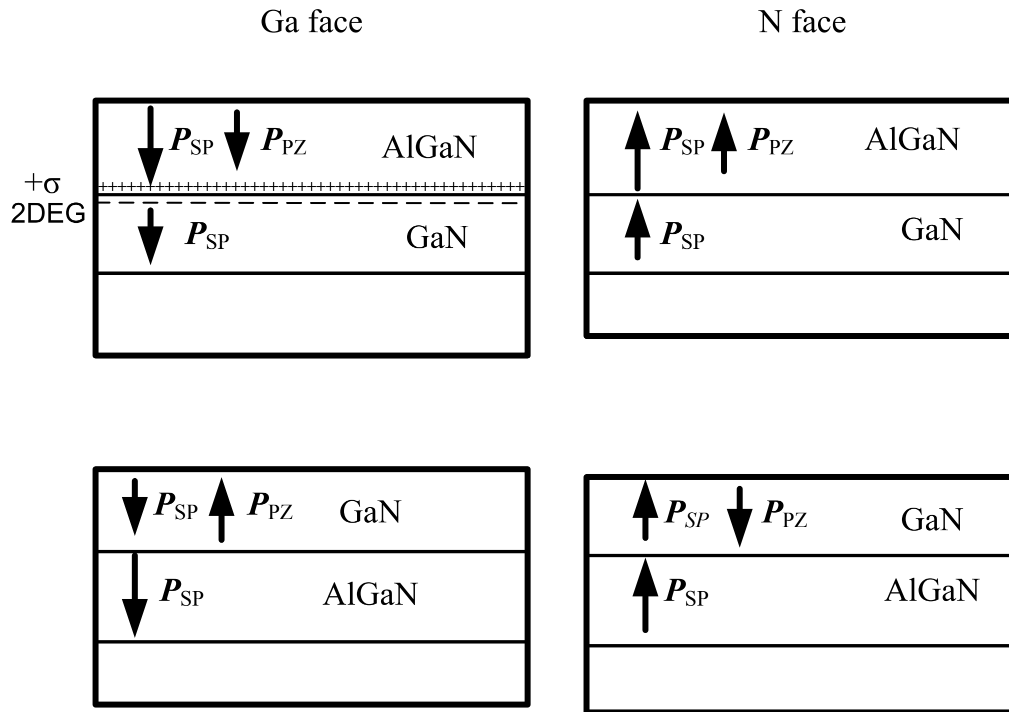

Figure 2.4 Four different topologies of both Ga- and N-face AlGaN/GaN and inverted GaN/AlGaN heterostructures along with their associated directions of spontaneous and piezoelectric polarization vectors.

spontaneous and piezoelectric polarizations are illustrated in Figure 2.4. Growing an unintentionally doped Ga-face AlGaN on GaN induces a large positive fixed sheet of charge (+*σ*) in the barrier-layer (Figure 2.4). The induction of this sheet of charge results from the discontinuity of the polarization vectors across the heterointerface. In this specific structure (i.e., Ga-face AlGaN/GaN), the high charge concentration of this layer is the result of the uni-directionality of the discontinuity in both polarization vectors (i.e., spontaneous and piezoelectric). As a result of establishment of this positive fix charge, free electrons are expected to accumulate at the GaN side of the heterointerface, presumably through unintentional doping of the heterostructure by O, N-vacancies, Si, or surface donors of AlGaN [1]. The 2DEG is also speculated to have originated from the

surface donors of the AlGaN barrier, whose energy level is approximately located about 1.5 eV below the conduction-band edge [1]. The dipole created between the aforementioned positive fixed charge in the barrier-layer and 2DEG in the GaN-layer results in formation of a strong electric-field that can induce further bending to the conduction-band (i.e., compared to that of AlGaAs/GaAs heterointerface). In Ga-face GaN/AlGaN, the spontaneous and piezoelectric polarizations are formed in the opposite directions and hence this does not lead to formation of as large a 2DEG at the heterointerface.

Figure 2.5 (a) illustrates a cross-sectional schematic of a Ga-face AlGaN/GaN HFET, along with the 2DEG channel formed at the heterointerface. As indicated above, the large

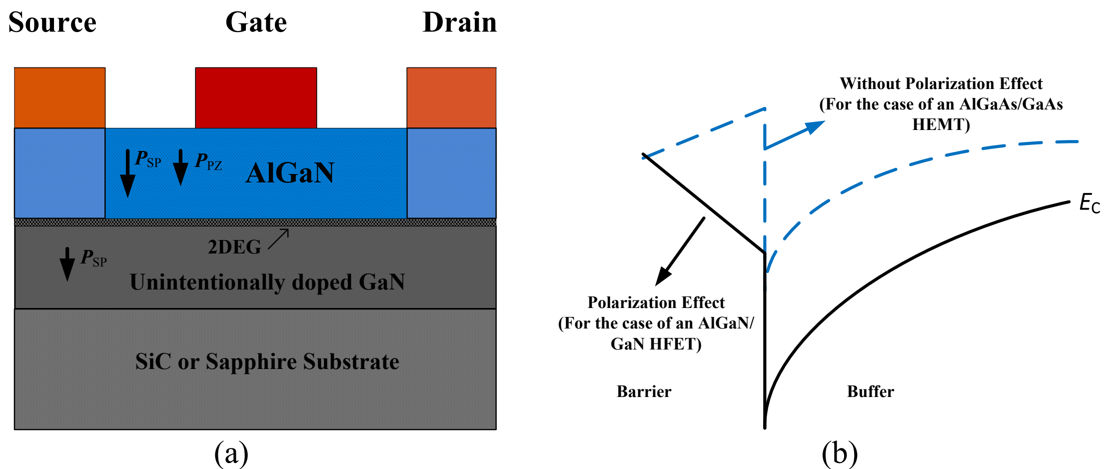

Figure 2.5 (a) A cross-sectional schematic of an AlGaN/GaN HFET. An overall polarization effect causes induction of a significant polar 2DEG at the heterointerface in GaN layer. As shown in this figure for the Ga-face AlGaN/GaN both piezoelectric (i.e., Ppz) and spontaneous polarization (i.e., Psp) vectors are in the same direction. (b) The conduction-band edge diagram of a heterojunction system without polarization effect, (for the case of AlGaAs/GaAs HFET show in dashed line and with polarization effect for the case of a polar AlGaN/GaN HFET show in solid line. Figures are not in scale.

2DEG concentration is formed as a result of both spontaneous and piezoelectric polarizations that are developed in the same direction. Figure 2.5 (b) shows a contrast between the conduction-band diagrams of an AlGaAs/GaAs (dashed line) and an AlGaN/GaN (solid line) heterostructure. The obvious differences observed between the conduction band-bending of these two heterostructures is the result of presence of piezoelectric and spontaneous polarizations in the AlGaN/GaN heterostructures. In contrast to AlGaN/GaN HFETs, in the modulation-doped AlGaAs/GaAs heterojunction the development of channel is attributed to the depletion of the wider bandgap material (i.e., AlGaAs).

The total polarization vector in a material, which is not exposed to any other external forces, is the vector sum of the spontaneous and piezoelectric polarization vectors,

$$\boldsymbol{P}_{tot} = \boldsymbol{P}_{PZ} + \boldsymbol{P}_{SP} \quad (2.4)$$

The polarization-induced charge density is calculated as the divergence of polarization in space,

$$\rho(\boldsymbol{P}_{tot}) = -\nabla.\boldsymbol{P}_{tot} \quad (2.5)$$

As a result of the previously mentioned direction of these polarization vectors normal to the heterointerface, the sheet charge density at a heterointerface is equal to,

$$\sigma(P_{tot}) = P_{tot}(bottom) - P_{tot}(top) \quad (2.6)$$

Polarization vectors of ternary III-nitride alloys were originally assumed to linearly depend on the values determined in the parent binaries of the compound. However, as a result of thorough investigations on polarization effects in III-nitrides by Bernardini et al., non-linearities of both spontaneous and piezoelectric polarizations were proven and evaluated [6], [23], [39] - [41]. Accordingly, they developed empirical expressions to

predict these non-linearities. Based on this study, the spontaneous polarizations of ternary III-nitride alloys are expressed as,

$$\begin{cases} P^{SP}_{Al_xGa_{1-x}N} = -0.090\mathrm{x} - 0.034(1-\mathrm{x}) + 0.019\mathrm{x}(1-\mathrm{x}) \\ P^{SP}_{In_xGa_{1-x}N} = -0.042\mathrm{x} - 0.034(1-\mathrm{x}) + 0.038\mathrm{x}(1-\mathrm{x}) \\ P^{SP}_{Al_xIn_{1-x}N} = -0.090\mathrm{x} - 0.042(1-\mathrm{x}) + 0.071\mathrm{x}(1-\mathrm{x}) \end{cases} \quad (2.7)$$

where the second terms are the common linear interpolations according to the binary compounds and the third bowing terms are representing second order nonlinearities.

It was shown in [40], [41] that for a ternary III-nitride alloy, the piezoelectric polarization can be calculated based on Vegard's interpolation of the bulk piezoelectric polarization, which is strain dependent according to,

$$\begin{cases} P^{PZ}_{AlN} = -1.808\varepsilon(\mathrm{x}) + 5.624\varepsilon(\mathrm{x})^2 \quad \text{for } \varepsilon < 0\text{, compressive strain} \\ P^{PZ}_{AlN} = -1.808\varepsilon(\mathrm{x}) - 7.888\varepsilon(\mathrm{x})^2 \text{ for } \varepsilon > 0\text{, tensile strain} \\ P^{PZ}_{GaN} = -0.918\varepsilon(\mathrm{x}) + 9.541\varepsilon(\mathrm{x})^2 \\ P^{PZ}_{InN} = -1.373\varepsilon(\mathrm{x}) + 7.559\varepsilon(\mathrm{x})^2 \end{cases} \quad (2.8)$$

where $\epsilon(\mathrm{x})$, the basal strain, is a function of mole-fraction x according to,

$$\epsilon(\mathrm{x}) = \frac{a_{Substrate-a(\mathrm{x})}}{a(\mathrm{x})}, \quad (2.9)$$

where $a_{\mathrm{Substrate}}$ and $a(\mathrm{x})$ are the in-plane lattice constants of the substrate and the epilayer, respectively.

For the case of AlGaN/GaN heterostructure, the 2DEG concentration increases with increasing the Al mole-fraction, to values exceeding 10^{13} cm^{-2}. Increase in the Al mole-fraction of the barrier, however, is observed to develop a maximum affordable barrier thickness in conjunction with the built-up of strain. Exceeding this value, for a given Al mole-fraction, results in crack formation in the tensile-strained layers [1].

2.6 Low-frequency noise in semiconductor devices

Performance in all semiconductor devices, although to different degrees, is limited by the presence of a large number of noise sources. These noise sources, in terms of their temporal behavior, are categorized into a number of groups including thermal noise, low-frequency noise (i.e., Generation-Recombination (G-R) and 1/f (flicker) noise), and shot noise [42].

In order to provide a general understanding of the aforementioned noise sources, different types of these noise sources are categorized in the following,

1. Thermal noise (Johnson-Nyquist noise):

If all external sources of a conductive element, for example a finite resistor with resistance R, are disconnected, then the average voltage across that resistor is zero. However, at temperatures above 0 K, a more accurate observation of the root mean square (RMS) value of the voltage across this resistor reveals a certain power spectral density. This is due to the random thermal motion of charge carriers (electrons in case of a metallic resistor), in the conductive element. As a result of this thermal motion, charge carriers collide with the atoms and hence exchange their thermal energy. The current or voltage power spectral density (PSD) of thermal noise shows a white spectrum according to,

$$\begin{cases} S_V(\frac{V^2}{Hz}) = 4kTR \\ \text{and} \\ S_I(\frac{A^2}{Hz}) = \frac{4kT}{R}, \end{cases} \tag{2.10}$$

where k is the Boltzmann constant, T is temperature, and R is the resistance.

2. Shot noise:

Each electron (hole) carries a single discrete charge in a steady current. As a result, each carrier produces a small pulse of current. A DC current consists of a number of pulses produced by carriers with certain spacing. However, the discrete nature of electrons and holes, and fluctuations in carrier temperature, can perturb the uniform spacing of the carriers when flowing through a potential barrier. The mutually independent nature of this mode of carrier transport is the cause for noise induction with a power spectral density of the form,

$$S_I = 2eI \tag{2.11}$$

where e is the unit charge and I is the average current flowing through the barrier.

3. Generation-Recombination (G-R) noise:

Generation-Recombination noise is the result of the fluctuation of the number of carriers (N) in the conduction-band or valence-band, due to trapping/de-trapping into and out of the trap centers in the semiconductor. This kind of behavior results in the fluctuation of the conductance G (resistance R) of the semiconductor. The noise power spectral density of G-R noise can be calculated according to,

$$\frac{S_G}{G^2} = \frac{S_R}{R^2} = \frac{S_I(f)}{I^2} = \frac{S_N(f)}{N^2} = \frac{1}{N^2}\frac{4\overline{\Delta N^2}\tau}{1+4\pi^2 f^2 \tau^2} \tag{2.12}$$

where $\overline{\Delta N^2}$ is the variance of the number of the trapped carriers, τ is the fluctuation time constant of trapping/de-trapping processes, and f is the frequency [43]. It should be mentioned that the G-R power spectral density represented by (2.12) is associated with the carrier number fluctuation caused by a single trap level. The fluctuation time constant of the G-R mechanism is related to the trap energy level according to the modified Arrhenius characteristic, which will be discussed later in chapter 4. Figure

2.6 illustrates the power spectral density of G-R noise caused by a single trap level according to (2.12). As shown in this figure, at very low frequencies, the G-R noise PSD reaches a plateau, whereas it follows a $1/f^2$ spectrum at frequencies higher than a corner frequency (f_c) determined by the fluctuation time constant (τ).

4. 1/f noise:

The 1/f noise is the result of the fluctuation in the conductance of a semiconductor, which can be attributed to the fluctuation of either mobility or number of the carriers. This noise has a power spectral density proportional to $1/f^{\gamma}$, where γ is referred to as frequency exponent that is observed to vary between 0.9 and 1.2 in different device technologies [42]. It should be noted that if the frequency exponent was equal to 1 over the entire frequency range, then such a power spectral density would result in an infinite value of energy. Therefore, it is theoretically unacceptable for the frequency exponent to be exactly equal to 1 in the entire frequency range of 0 to ∞. The

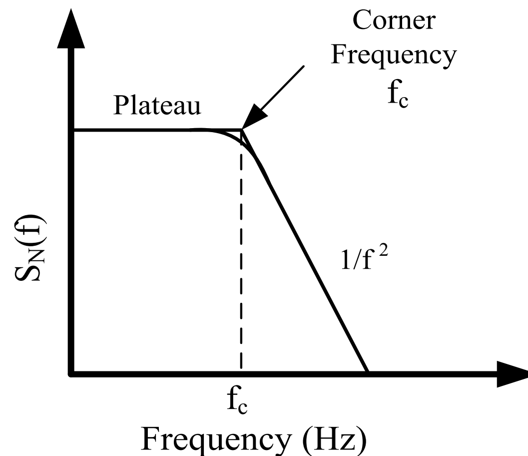

Figure 2.6 G-R Lorentzian power spectral density with the indication of corner frequency (f_c).

frequency exponent must be greater than one at the higher frequency end, while a low-frequency plateau is theoretically expected.

The exact origins of the low-frequency noise, particularly 1/f noise, have been the topic of a vibrant scientific endeavor, which has resulted in a number of competing theories [44]. Among these theories, carrier-number fluctuation [45] and mobility fluctuation [46] are the two most accepted theories proposed by McWhorter and Hooge, respectively. The first theory is based on the superposition of the carrier Generation-Recombination Lorentzian profiles, with a fairly dense distribution of fluctuation time constants. Considering the accumulative effect of a continuous band of trap levels, integration of (2.12) over a range of fluctuation time constants results in a 1/f noise spectrum (Figure 2.7).

The McWhorter model is based on the consideration of a specific distribution function of fluctuation time constants defined for a continuous band of trap levels. Therefore, for this continuous band of trap levels, (2.12) will evolve,

$$S_N(f) = \int_{\tau_l}^{\tau_h} \frac{4\overline{\Delta N^2}\tau g(\tau)d\tau}{1+4\pi^2 f^2 \tau^2}. \tag{2.13}$$

where $g(\tau)d\tau$ is the distribution function of the fluctuation time constants, and τ_l and τ_h are the boundary values of the fluctuation time constants [44].

McWhorter proposed a distribution function defined as,

$$\begin{cases} g(\tau)d\tau = \frac{d\tau}{\tau Ln\left(\frac{\tau_2}{\tau_1}\right)} & \text{for } \tau_1 < \tau < \tau_2 \\ g(\tau)d\tau = 0 & \text{otherwise} \end{cases} \tag{2.14}$$

where τ_1 and τ_2 are defined as the fluctuation time constants associated with the two boundaries of a band of trap centers.

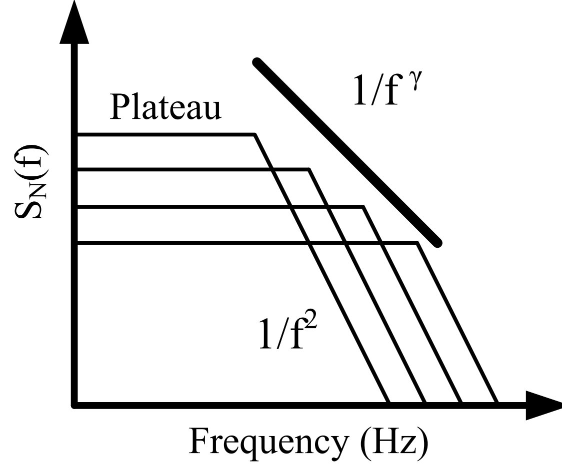

Figure 2.7 1/f noise as a result of the accumulative effect of the carrier Generation-Recombination Lorentzian profiles with a fairly dense distribution of fluctuation time constants. The frequency exponent (i.e., γ) of the $1/f^{\gamma}$ spectrum is between 0 and 1.2.

Considering (2.14) in (2.13), the noise power spectral density $S_N(f)$ can be calculated as [47],

$$\begin{cases} S_N(f) = \int_0^{\infty} \frac{4\overline{\Delta N^2}\tau g(\tau) d\tau}{1+4\pi^2 f^2 \tau^2} = \frac{\overline{\Delta N^2}}{f Ln(\frac{\tau_2}{\tau_1})} \text{ for } 1/\tau_1 < \omega < 1/\tau_2, \\ S_N(f) = \frac{2\overline{\Delta N^2}}{\pi f Ln\left(\frac{\tau_2}{\tau_1}\right)} tan^{-1}(\omega\tau_2) \text{ for } \omega\tau_1 \ll 1, \text{ and} \\ S_N(f) = \frac{\overline{\Delta N^2}}{f Ln\left(\frac{\tau_2}{\tau_1}\right)} [1 - \frac{2tan^{-1}(\omega\tau_1)}{\pi}] \text{ for } \omega\tau_2 \gg 1. \end{cases} \quad (2.15)$$

According to the number fluctuation theory, a low-frequency noise spectrum, that shows a $1/f^{\gamma}$ spectrum in a wide range of frequencies, demands a mechanism, which can be characterized by trapping/de-trapping time constants that varies from relatively low to very large values. This type of low-frequency noise spectrum was observed and reported in Silicon MOSFETs [48]. Different mechanisms were analyzed in order to propose a fluctuation time constant that is large enough to produce such $1/f^{\gamma}$ noise spectrum.

Among these phenomena, a proposed mechanism was based on the statistical carrier fluctuations in the channel and along the interface, which did not lead to a desired fluctuation time constant to reveal 1/f noise spectrum in a wide range of frequencies [48]. In another attempt, McWhorter's approach was applied to Silicon MOSFETs by Christensson *et al*. using the tunneling phenomenon for the impinging carriers from the channel to the trap centers inside the oxide. This model was successful in predicting 1/f noise spectrum in a large frequency range [48].

The second theory of 1/f noise (i.e., mobility fluctuation) is, however, based on an empirical relationship, in which the normalized noise power is evaluated according to,

$$\frac{S_G}{G^2} = \frac{S_R}{R^2} = \frac{S_N(f)}{N^2} = \frac{\alpha_0}{fN}, \tag{2.16}$$

where α_0 is the dimensionless constant, which is referred to as Hooge's parameter. This relationship normalizes noise to one electron. The only assumption in concluding (2.16) is that, whatever mechanisms the electrons are involved in, they take part independently [46].

In high quality semiconductors (e.g., epitaxial layers), the dimensionless Hooge's parameter is reported to vary between 10^{-6} to 10^{-4} [49]. In GaN-based devices, the reported values of Hooge's parameter were larger than 10^{-2} whereas the recently observed α_0 is in the range of 10^{-5} – 10^{-4} [50]. Accordingly, this trend can be an indication of considerable progress in the growth techniques of III-nitride materials and fabrication process of associated devices.

Several studies on a wide range of solid state electronic devices (from Si- and GaAs-based FETs to III-nitride-based HFETs) have confirmed that low-frequency noise including 1/f noise is an extremely sensitive tool, which can be used to investigate the

material quality and imperfections [24], [25]. The linear regime of operation is deemed most useful for the analysis of LFN characteristics. This is because ambiguities contributed by factors present in saturation mode of operation such as velocity saturation, pinch-off, and self-heating render the noise analysis unnecessarily complicated and unreliable.

According to the temperature-dependent characteristics and signatures observed in various profiles of low-frequency noise spectra of a semiconductor or device, semiconductor imperfections and reliability issues of the device can be evaluated. Depending on these observations, proper solutions/remedies can be suggested to improve the device performance. In addition, various low-frequency noise signatures, which can be up-converted to high frequencies, is considered as a figure of merit at the circuit level in electronic and communication systems including both linear (e.g., LNA) and non-linear (e.g., VCO) circuits [51]. Therefore, the investigation of low-frequency noise characteristics and the study of possible origins of this mechanism can be used to evaluate the performance of the devices.

Chapter 3

Determination of the subband energy levels and the 2DEG characteristics of $Al_xGa_{1-x}N/GaN$ heterojunctions using variational method

3.1 Introduction

Polar $Al_xGa_{1-x}N/GaN$ heterojunction field effect transistors enjoy superior device properties including high sheet-carrier-concentration, high breakdown voltage, and high electron saturation velocity compared to their counterparts in Si and GaAs technologies [9], [10]. As a result, over the past two decades, this rapidly growing device technology has managed to draw a great deal of attention for fulfilling market demands in RF and microwave applications [52], [53].

As discussed in chapter 2, in pseudomorphically grown AlGaN/GaN heterostructures, the considerable built-in strain along with the large piezoelectric coefficients causes a sizeable piezoelectric polarization effect. The combination of this large piezoelectric polarization and the existence of a large discontinuity of the spontaneous polarization at the heterointerface induces a high sheet-carrier-concentration (i.e., in the order of 10^{13} cm^{-2}) at the GaN side of the heterojunction [6]. This high sheet-carrier-concentration produces a bending in the conduction-band of the channel/buffer layer (i.e., GaN) which is much larger compared to other HFETs such as AlGaAs/GaAs. Consequently, in physics-based modeling of this material system, applying the simplifying approximation of a triangular potential well in the channel/buffer layer does not lead to a realistic evaluation of the two dimensional electron gas concentration and subband energy levels, especially at higher Al mole-fractions. As made evident in the results and discussions section, at higher Al mole-fractions, on the basis of this simplified approximation, the second subband energy level may be erroneously calculated to be positioned above the conduction-band discontinuity. This is due to the considerable increase of the 2DEG concentration with the Al mole-fraction. In this case, the actual potential profile is required to calculate the subband energy levels.

With the intention of developing an in-depth knowledge about the properties of this relatively new device technology, over the past few years, a number of theoretical investigations based on the triangular quantum well approximation have been reported [19], [20]. The results of these studies, however, are limited by the inherent constraints of the triangular quantum well approximation. In addition to these studies, calculations of the 2DEG characteristics of AlGaN/GaN heterojunctions based on the complicated self-

consistent method [21] and the variational method [22] have been reported. Among these two methods, the latter is more mathematically manageable. Although, employing this method Lee calculated the first subband energy level [22], he did not explore the calculation of the second subband energy level, which is very essential to more accurate evaluation of 2DEG characteristics of the AlGaN/GaN system at higher carrier concentrations. It is, therefore, the intention of this work to propose and present a complete variational method for calculating the 2DEG characteristics of gated AlGaN/GaN heterojunctions (including the first and second subband energy levels for various Al mole-fractions, barrier thicknesses, background dopant concentrations, and gate voltages).

3.2 Theoretical model

As mentioned in section 3.1, the variational method has been adopted to accurately calculate the 2DEG characteristics of AlGaN/GaN heterojunctions. In this model, after [22], [54], the trial functions used for the first and second subband energy levels are,

$$\psi_0(z) = \frac{1}{\sqrt{A}}[u(z)(z+\alpha)e^{-\frac{bz}{2}} + u(-z)\alpha e^{k_b z}] \tag{3.1}$$

and

$$\psi_1(z) = \frac{1}{\sqrt{B}}[u(z)(z+\alpha')(1-Cz)e^{-\frac{bz}{2}} + u(-z)\alpha' e^{k'_b z}] \tag{3.2}$$

respectively, where z is the direction normal to the heterointerface, b is the variational parameter, $u(z)$ is Heaviside step function, A and B are normalization factors, and C is an arbitrary constant calculated by applying the orthogonality condition between $\psi_0(z)$ and $\psi_1(z)$. The constants α and α' are calculated by applying the continuity condition

on $\psi_0(z), \psi_1(z)$, and their normalized first spatial derivatives. The parameters k_b and $k_b^{'}$ are the wave numbers associated with the first and second subband energy levels in the barrier-layer, respectively, and are calculated as,

$$k_b = \frac{\sqrt{2m^*_{\text{AlGaN}}(\Delta E_C - E_0)}}{\hbar} \tag{3.3}$$

and

$$k_b' = \frac{\sqrt{2m^*_{\text{AlGaN}}(\Delta E_C - E_1)}}{\hbar}, \tag{3.4}$$

where $\hbar$ is the modified Planck's constant, m^*_{AlGaN} is the density of states (DOS) effective mass of electrons along the growth direction in the barrier, and ΔE_C is the conduction-band discontinuity at the heterointerface.

The normalization factors *A*, *B*, and arbitrary constant *C*, are calculated as follows,

$$A = \frac{\alpha^2}{2k_b} + \frac{\alpha^2 b^2 + 2\alpha b + 2}{b^3}, \tag{3.5}$$

$$B = \frac{-1}{b^5}\left[-2b^2\left(\alpha'^2 C^2 - 4\alpha' C + 1\right) - b^4\alpha'^2 + 2\alpha' b^3(\alpha' C - 1) - 12bC(\alpha' C - 1) - 24C^2\right] + \frac{\alpha'^2}{2k_b'}, \tag{3.6}$$

and

$$C = \frac{-N_1 + \sqrt{N_1^2 - 4N_2 N_3}}{2N_2}, \tag{3.7}$$

where

$$N_1 = 2\alpha m^*_{\text{AlGaN}} b^2 + 4\alpha b m^*_{\text{GaN}} k_b' + 6m^*_{\text{AlGaN}} b + 12m^*_{\text{GaN}} k_b', \tag{3.8}$$

$$N_2 = 4m^*_{\text{AlGaN}} b\alpha + 12m^*_{\text{AlGaN}}, \tag{3.9}$$

and

$$N_3 = -[2\alpha m^*_{\text{AlGaN}}\left(\frac{k_b+k'_b+b}{k_b+k'_b}\right)b^3 + 3\alpha b^2 m^*_{\text{GaN}}k'_b + \alpha m^*_{\text{AlGaN}}b^3 + 4m^*_{\text{AlGaN}}b^2 + 4bm^*_{\text{GaN}}k'_b]. \quad (3.10)$$

The Hamiltonian *H* of the system is defined as,

$$< H_i > = < T_i > + < V_i >, \quad (3.11)$$

where $< T_i >$ and $< V_i >$ are the expected values of the kinetic and potential energies associated with the *i*-th subband energy level, respectively. These are calculated as [55],

$$< T_i > = \int_{-\infty}^{+\infty} \frac{1}{2m^*}\left|\frac{\hbar}{j}\frac{\partial\psi_i(z)}{\partial z}\right|^2 dz, \quad (3.12)$$

and

$$< V_i > = \int_{-\infty}^{+\infty} V(z)|\psi_i(z)|^2 dz, \quad (3.13)$$

where *V*(z) is the total potential energy profile developed by the presence of 2DEG, polarization fields, and the depletion layer charge. In the barrier- and channel/buffer-layer *V*(z) is appropriately represented by V_{AlGaN} and V_{GaN}, respectively. In terms of (3.12), the expected values of the kinetic energy for the first two subband energy levels can be expanded as,

$$< T_0 > = \frac{\hbar^2}{4Am^*_{\text{GaN}}}[\frac{1}{b} - \alpha + \frac{\alpha^2}{2}\left(b + \frac{2m^*_{\text{GaN}}}{m^*_{\text{AlGaN}}}k_b\right)], \quad (3.14)$$

and

$$< T_1 > = \frac{\hbar^2\alpha'^2 k'_b}{4Bm^*_{\text{AlGaN}}} + \frac{\hbar^2}{8Bm^*_{\text{GaN}}b^3}[2b^2\left(\alpha'^2C^2 + 1\right) + b^4\alpha'^2 + (2\alpha'b^3 + 4bC)(\alpha'C - 1) + 8C^2] \quad (3.15)$$

The potential profile of the barrier-layer (i.e., V_{AlGaN} (z)) is calculated by assuming a constant electric-field inside the barrier. The potential profile of the channel/buffer-layer (i.e., V_{GaN} (z)), which is the potential developed due to the presence of 2DEG (i.e., $V_{\text{GaN-}}$

$_s$(z)) and the depletion layer charge (i.e., $V_{\text{GaN-d}}$ (z)), can be calculated by using the solution of Poisson equation [55],

$$V_{\text{GaN}}(z) = V_{\text{GaN}-s}(z) + V_{\text{GaN}-d}(z), \tag{3.16}$$

$$V_{\text{GaN}-s}(z) = \frac{e^2}{\epsilon_0 \epsilon_{\text{GaN}}} \sum_{i=1}^{2} n_{S_i}[z + \int_0^z (z' - z)\psi_i^2(z')dz'], \tag{3.17}$$

and

$$V_{\text{GaN}-d}(z) = \frac{e^2}{\epsilon_0 \epsilon_{\text{GaN}}} N_D z_d z(1 - \frac{z}{2z_d}), \tag{3.18}$$

where, ϵ_{GaN} is the relative dielectric constant of the buffer, n_{S_i} is the 2DEG concentration of the *i*-th subband energy level, N_D is the background dopant concentration in the depletion layer, z_d is the depletion layer thickness (i.e., $z_d = \sqrt{\frac{4\epsilon_0 \epsilon_{\text{GaN}} \varphi_{fn}}{eN_D}}$), and z is the distance from the heterointerface. In this relationship, the potential $\varphi_{fn} = \frac{kT}{e} Ln(N_D/n_i)$, where n_i is the Wurtzite GaN intrinsic carrier concentration.

The expected values of $V_{\text{AlGaN}}(z)$, $V_{\text{GaN}-s}(z)$, and $V_{\text{GaN}-d}(z)$ for the first two subband energy levels are calculated as follows,

$$< V_{\text{AlGaN}(0)} >= \frac{\alpha^2}{4Ak_b^2}(\frac{-e|\sigma - n_{S1}e|}{\varepsilon_0 \varepsilon_{\text{AlGaN}}} + 2\Delta E_C k_b), \tag{3.19}$$

$$< V_{\text{GaN}-s(0)} >= \frac{e^2 n_{S1}}{4b^4 A^2 \varepsilon_0 \varepsilon_{\text{GaN}}}[4A(\alpha^2 b^2 + 4\alpha b + 6) \ - \frac{1}{b^3}(2\alpha^4 b^4 + 12\alpha^3 b^3 + 30\alpha^2 b^2 +$$

$$30\alpha b + 15)] + \frac{e^2 n_{S2}}{8b^9 AB\varepsilon_0 \varepsilon_{\text{GaN}}}\{-8\alpha^2 Bb^7 - 4(\alpha'^2\alpha^2 - 42B\alpha)b^6 -$$

$$4\{-\alpha'\alpha[-5\alpha + \alpha'(5C\alpha - 1)] + 4[(C\alpha^2 + \alpha)\alpha'^2 - \alpha^2\alpha' - 3B]\}b^5 -$$

$$2\{[17\alpha^2 C^2 - 12\alpha C - 16(\alpha C + 1)(\alpha C - 1) + 1]\alpha'^2 + 2(-2C\alpha^2 + 6\alpha)\alpha' + \alpha^2\}b^4 -$$

$$2\{-C[-23C\alpha + 16(\alpha C + 1) + 7]\alpha'^2 + [3(49\alpha^2 C^2)C^2 - 4(23\alpha)C - 16(9\alpha^2 C^2 -$$

$$4\alpha C - 1) + 7]\alpha' + 3C\alpha^2 - 7\alpha\}b^3 + 6[-5\alpha'^2 C^2 + (-\alpha^2)C^2 + 8\alpha C + 2\alpha'(-4C\alpha +$$

$$10)C-5]b^2+6C[-19\alpha'C-201C\alpha+32(6\alpha C-1)+51]b-141C^2\}, \quad (3.20)$$

$$< V_{\mathrm{GaN}-d(0)} >= \frac{e^2N_D}{2Ab^5\varepsilon_0\varepsilon_{\mathrm{GaN}}}(\alpha^2b^2(2bz_d-2)-2\alpha b(-4bz_d+6)+12bz_d-24), \quad (3.21)$$

$$< V_{\mathrm{AlGaN}(1)} >= \frac{\alpha'^2}{4Bk_b'^2}(\frac{-e|\sigma-n_{S2}e|}{\varepsilon_0\varepsilon_{\mathrm{AlGaN}}}+2\Delta E_C k_b'), \quad (3.22)$$

$$< V_{\mathrm{GaN}-s(1)} >= \frac{e^2n_{S2}}{4b^{11}B^2\varepsilon_0\varepsilon_{\mathrm{GaN}}}\{4B\alpha'^2b^9-2[\alpha'^4+8BC\alpha'^2-8B\alpha']b^8-4(-3C\alpha'^4+3\alpha'^3-6BC^2\alpha'^2+24BC\alpha'-6B)b^7-2(15\alpha'^4C^2-48\alpha'^3C+15\alpha'^2-96BC^2\alpha'+96BC)b^6-2(-15C^3\alpha'^4+150C^2\alpha'^3-150C^2\alpha'^2+15\alpha'-240BC^2)b^5-15(C^4\alpha'^4+4\alpha'^3+76C^2\alpha'^2-24C\alpha'-6C^3+1)b^4-210C(C^3\alpha'^3-8C^2\alpha'^2+8C\alpha'-1)b^3-105C^2(11C^2\alpha'^2-32C\alpha'+11)b^2-2835C^3(\alpha'C-1)b-2835C^4\}+\frac{e^2n_{S1}}{8b^9AB\varepsilon_0\varepsilon_{\mathrm{GaN}}}\{8\alpha'^2Ab^7-4(\alpha^2\alpha'^2+8C\alpha'^2A-8\alpha'A)b^6-4[\alpha\alpha'^2+\alpha^2(-5C\alpha'^2+5\alpha')-12A-12AC^2\alpha'^2+48AC\alpha']b^5-2\{\alpha'^2+\alpha^2[\alpha'^2C^2-4\alpha'C+16(\alpha'^2C^2-4\alpha'C+1)+1]+2\alpha'(-6C\alpha'^2+6\alpha')+192AC+2\alpha'(-96AC^2)\}b^4-2\{-7C\alpha'^2+3C\alpha'^2[\alpha'C+16(3C+\alpha'-3)-1]+7\alpha'+\alpha[7C^2\alpha'^2+28\alpha'C+16(C^2\alpha'^2-48\alpha'C+1)+7]-480AC^2\}b^3-6\{129C^2\alpha^2+5C^2\alpha'^2-20\alpha'C+2\alpha[4\alpha'C+32(\alpha'C-1)-4]C+5\}b^2-6C[201\alpha C+19\alpha'C+32(\alpha'C-1)-19]b-909C^2\}, \quad (3.23)$$

and

$$< V_{\mathrm{GaN}-d(1)} >= \frac{e^2}{2b^7B\epsilon_0\epsilon_{\mathrm{GaN}}}N_D\{2b^4[\alpha'^2(-4Cz_d-1)+4\alpha'z_d]+12b^3[-\alpha'^2C(z_dC+1)+\alpha'(-4z_dC-1)+z_d]-24b^2[\alpha'^2C^2-2\alpha'C(2Cz_d+2)+4Cz_d+1]-2b^5\alpha'(-\alpha'z_d)-240bC(\alpha'C-Cz_d-1)-720C^2\}. \quad (3.24)$$

In order to calculate the proper value of variational parameter (i.e., $b = b_m$), the total energy per electron defined as,

$$\frac{E}{n_S} = < T_0 > + 0.5(< V_{\mathrm{GaN}-s(0)} > + < V_{\mathrm{AlGaN}(0)} >) + < V_{\mathrm{GaN}-d(0)} > \quad (3.25)$$

is minimized. In this definition, the factor 0.5 prevents double-counting of the electron-electron interactions [55]. The minimization of (3.25) is possible by finding a proper value of variational parameter (i.e., $b = b_m$). Following this step, E_0 is calculated by setting $i = 0$ and $b = b_m$ in (3.11). The second subband energy level can be also calculated by setting $i = 1$ and using the same value of b_m in (3.11).

The flowchart of the method used in recursive calculations of n_s and the first two subband energy levels is presented in Figure 3.1. The calculation procedure starts by assuming an initial position for the Fermi energy level (i.e., the lower edge of the conduction-band of GaN at the heterointerface) and calculating the total 2DEG concentration using the following equation [6],

$$n_s = \frac{\sigma}{e} - \left(\frac{\epsilon_0 \epsilon_{\mathrm{AlGaN}}}{d_{\mathrm{AlGaN}} e^2}\right) [e(\varphi_b - V_{GS}) + E_F - \Delta E_c], \quad (3.26)$$

where σ is the polarization-induced 2D charge density at the polar AlGaN/GaN heterointerface, ϵ_{AlGaN} is the relative dielectric constant of AlGaN, d_{AlGaN} is the thickness of the AlGaN barrier, and φ_b is the effective Schottky barrier height.

The polarization-induced 2D charge density at the polar AlGaN/GaN heterointerface is provided by,

$$\sigma = P_{SP}(barrier) - P_{SP}(channel) + P_{PZ} \quad (3.27)$$

Dependence of polarization vectors on the Al mole-fraction, to different degrees of accuracy (i.e., with or without consideration of non-linearities), have been reported in [6], [35], [39] - [41]. Whereas for small values of x (i.e., $x < 0.15$) the non-linearities are

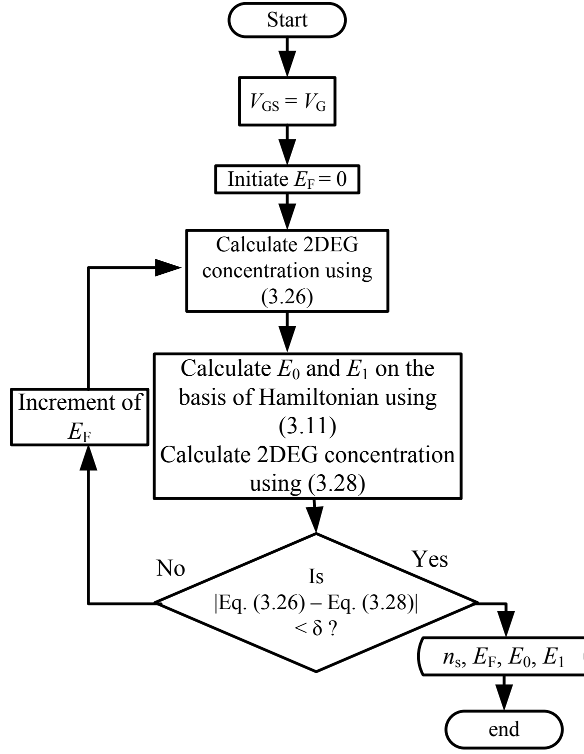

Figure 3.1 Overall flowchart of the method used in the calculation of the first and second subband energy levels (E_0 and E_1), and Fermi level (E_F).

negligible, for larger values it is deemed necessary to adopt the empirical expressions of Fiorentini et al. [41] and corrected constants of Bernardini et al. [35].

In the implementation of the proposed model, the concentration of unintentionally-doped donors is assumed to be in the order of 10^{14} cm^{-3} in the channel/buffer-layer, unless specified otherwise. Considering a Ni Schottky gate contact, φ_b as a function of Al mole-fraction is taken as $e\varphi_b = (1.3x + 0.84)$ eV [6].

In addition, in terms of the density of states function of the first two subband energy levels formed at the polar AlGaN/GaN heterointerface, the following equation must be also satisfied,

$$n_s = D_s \frac{kT}{e} \{\ln\left[1 + \exp\left(\frac{E_F - E_0}{kT}\right)\right] + \ln\left[1 + \exp\left(\frac{E_F - E_1}{kT}\right)\right]\} \tag{3.28}$$

where D_s is 2D density of states (i.e., $em^*/\pi\hbar^2$).

As indicated in Figure 3.1, in the calculation of the position of E_F, at thermal equilibrium, Fermi energy level is gradually increased from its initial position (i.e., the bottom of the conduction-band of GaN at the heterointerface) until (3.26) and (3.28) converge with a relative error defined as $\delta = 0.1\%$.

3.3 Results and discussions

In order to validate the present model, it has been attempted to reproduce the outcomes of the prior self-consistent works in this area (e.g., [21]) using the variational method. Whereas these reports dealt with specific values of Al mole-fraction, barrier thickness, and unintentional doping level, the goal of the present work is to provide a basis for calculating the 2DEG characteristics for the full range of these parameters.

As indicated in section 3.2, piezoelectric and spontaneous polarization vectors express a considerably non-linear dependence on the Al mole-fraction of the barrier, especially at higher values of x. However, in validating the present work versus the results of Lee et al. [21], in compliance with their assumptions, the linear approximations of both piezoelectric and spontaneous polarization vectors are also adopted in the present model [6]. The present model produces results that are in good match with the reported values of Lee et al. for AlGaN/GaN heterostructures of same specifications as those considered in [21] (i.e., with zero doping level of the channel/buffer- and barrier-layers, barrier thickness of 30 nm, Al mole-fractions of 0.2 and 0.3). Whereas for x of 0.2 and 0.3 the present model calculates 2DEG concentrations of ~8.4×10^{12} cm^{-2} and ~1.37×10^{13} cm^{-2}, respectively, the corresponding values from [21] are ~8.1×10^{12} cm^{-2} and ~1.40×10^{13}

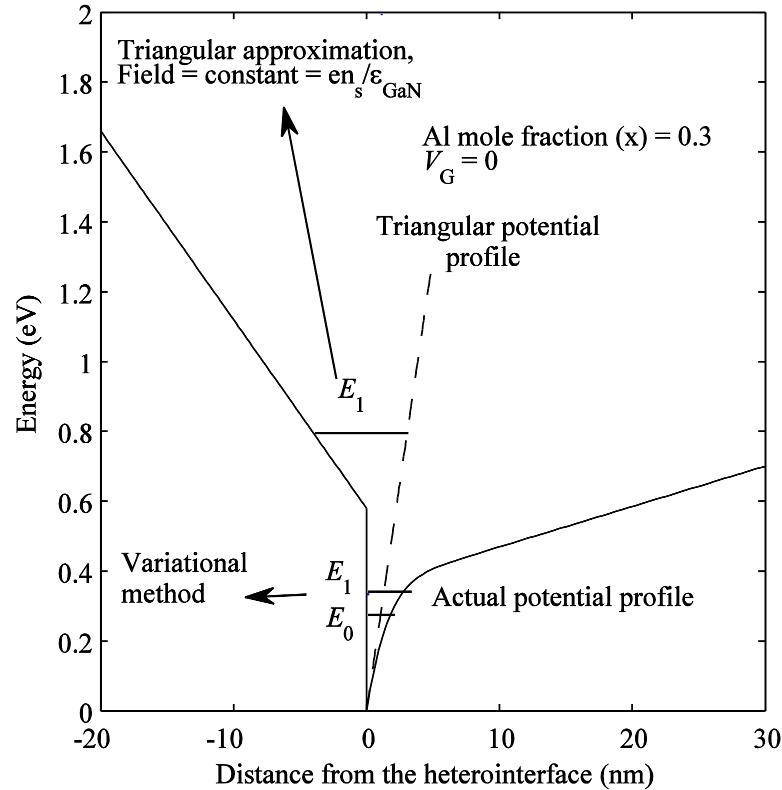

Figure 3.2 Calculated conduction-band diagram of a gated AlGaN/GaN heterostructure with Al mole-fraction of 0.3 and barrier thickness of 20 nm, at $V_G = 0$. Calculations are presented in terms of the variational method and the triangular quantum well approximation.

cm^{-2}. In addition, whereas Lee et al. report only the first and second subband energy levels for the Al mole-fraction of 0.2, their reported values (E_0 and E_1 are 0.19 eV and 0.30 eV, respectively) are in good match with those resulted from the present model (i.e., 0.24 eV and 0.31 eV, respectively).

For the sake of accuracy, the rest of the results presented in this section are calculated using the more accurate framework of [35] and [41], for evaluation of the polarization vectors.

The calculated conduction-band diagram on the basis of the variational method of section 3.2, with the inclusion of the positions of the first two subband energy levels, for a gated

AlGaN/GaN heterojunction with Al mole-fraction of 0.3, and barrier thickness of 20 nm, at zero gate voltage, is illustrated in Figure 3.2. Also in this figure, the predicted form of band bending and the positions of the first two subband energy levels using the triangular quantum well approximation are included. As shown in this figure, the conduction-band bending of the channel/buffer-layer across the quantum well is well pronounced. Therefore, accuracy of the calculations of the 2DEG characteristics based on the assumption of a triangular quantum well, particularly at higher 2DEG concentrations (e.g., 10^{13} cm^{-2}), is questionable. This observation will be further substantiated following the discussion of the 2DEG characteristics according to the variational method.

Figure 3.3 illustrates the variation of the first and second subband energy levels and Fermi energy level with Al mole-fraction ($0.1 \leq x \leq 1$) for the barrier thickness of 20 nm. The subband energy levels, Fermi energy level, and the 2DEG carrier-concentration, all decrease with reducing Al mole-fraction. As shown in Figure 3.3, the Fermi energy level is above E_0 (except for very small x). This figure clearly indicates the origin of the depletion-mode nature of such an AlGaN/GaN HFET.

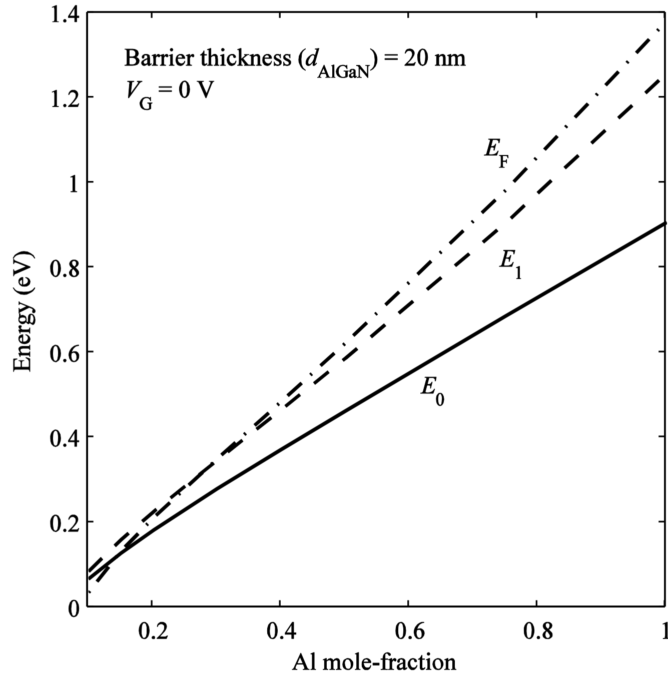

Figure 3.3 Variation of the first (solid line) and second (dashed line) subband energy levels (E_0 and E_1) and Fermi energy level E_F (dash-dotted line) with Al mole-fraction at $V_G = 0$.

For Al mole-fraction of 0.1, at zero gate voltage, the Fermi level is 1.2 *kT* below the first subband energy level whereas this difference is 1.9 *kT* at pinch-off condition (i.e., ~ gate voltage of -0.3 V). In addition, for x = 1, the second subband energy level is about 13 *kT* above the first subband energy level while the Fermi level is about 4.7 *kT* above the second subband energy level. Considering the fact that the third subband energy level will be much higher than the Fermi level and thus have a negligible occupation, for the full range of values of x, the first two subband energy levels should provide a complete basis for all practical calculations.

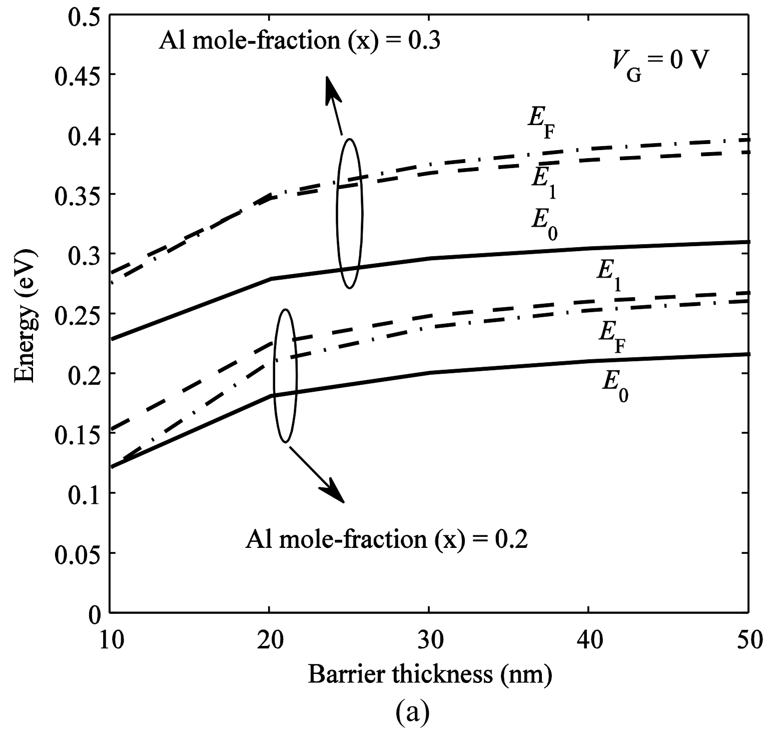

(a)

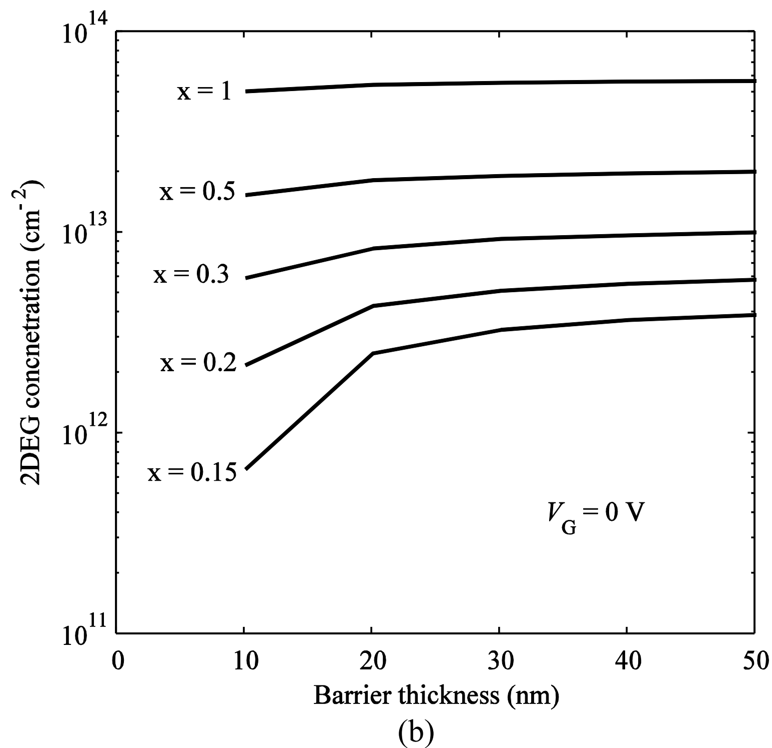

(b)

Figure 3.4 (a) Variation of the first (solid line) and second (dashed line) subband energy levels (E_0 and E_1) and Fermi energy level E_F (dash-dotted line) with barrier thickness at V_G = 0 for Al mole-fractions of 0.2 and 0.3. (b) Variation of the 2DEG carrier concentration as a function of barrier thickness for Al mole-fractions of 0.1-1.

The variations of the first and second subband energy levels and Fermi energy level (E_0, E_1, and E_F) with barrier thickness are shown in Figure 3.4 (a). This figure, as expected by the trends of the evolution of polarization vectors, demonstrates the rise in the position of the subband energy levels with increasing barrier thickness. For Al mole-fraction of 0.2, the Fermi energy level is lower than the second subband energy level. However, for Al mole-fraction of 0.3, Fermi level resides above the second subband energy level for larger barrier thicknesses, which is indicative of enhanced 2DEG concentration. The 2DEG concentration, as a function of the barrier thickness and Al mole-fraction, is also presented in Figure 3.4 (b). As shown in this figure, as a result of a more pronounced Schottky depletion effect with the reduction of the barrier thickness, the channel will be further depleted of free carriers.

The calculated 2DEG concentrations of AlGaN/GaN heterojunctions based on the present model are compared with the experimental data obtained from [41] (Figure 3.5). According to [41], these experimental data were acquired by CV measurements performed on AlGaN/GaN heterojunctions with the barrier thickness of 30 nm and for Al mole-fractions less than 0.5. As illustrated in this figure, with the exception of visible divergence at higher Al mole-fractions, theoretical results and experimental data demonstrate a good level of agreement. Strain-relaxation at higher Al mole-fractions, and the resulting reduction in piezoelectric polarization, is expected to be the culprit in the observed saturation of the experimentally reported values of 2DEG concentration in Figure 3.5. Since strain relaxation in tensile strained AlGaN barrier results in formation of defects in this layer, AlGaN/GaN heterojunctions of thick barriers, which are exposed to strain relaxation, are not fit for device fabrication. As a result, in the present model the

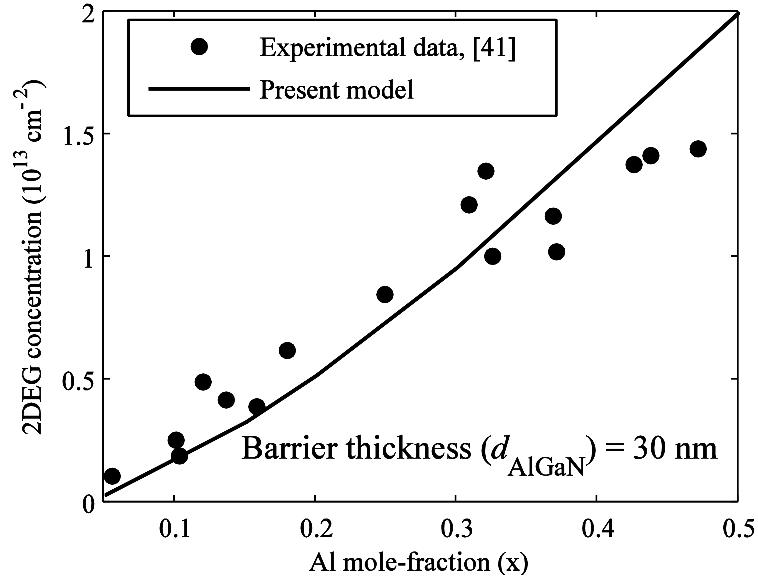

Figure 3.5 Comparison of the simulated 2DEG concentrations and experimental data obtained from [39] for AlGaN/GaN heterojunctions with barrier thickness (d_{AlGaN}) of 30 nm. The relaxation of the built-in strain in the barrier is not taken into account in the present model.

strain relaxation has not been incorporated. This explains the mismatch with the experimental data in Figure 3.5, for those values of Al mole-fraction which render a built-in strain exceeding values that support the un-relaxed growth of 30 nm thick AlGaN barrier.

The variation of subband energy levels with background donor concentration in the channel/buffer-layer is presented in Figure 3.6. The value of donor concentration is varied between the level of typically achieved unintentional doping and the ideal zero concentration. As illustrated in this figure, with increasing the background donor concentration, the subband energy levels only slightly increase (i.e., ~ 5%). However, more importantly the electron sheet concentration is found to be fairly constant within the same range of background dopant concentrations. This trend is also observed in [21].

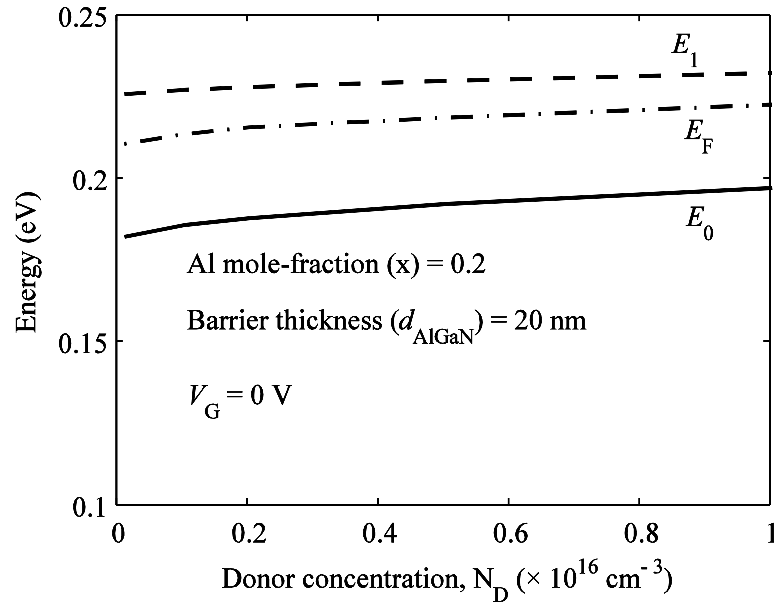

Figure 3.6 Variation of the Fermi level (dash-dotted line), first (solid line) and second (dashed line) subband energy levels with background donor concentration in an AlGaN/GaN heterojunction with Al mole-fraction of 0.2 and barrier thickness of 20 nm.

Evidently, applying a voltage on the gate contact changes the barrier height and hence modifies the position of the energy states, Fermi energy level, and the electron concentration under the gate region. Figure 3.7 illustrates the variation of the 2DEG carrier-concentration, the first two subband energy levels and Fermi energy levels with the gate voltage for a gated AlGaN/GaN heterojunction with barrier thickness of 20 nm and Al mole-fraction of 0.3. According to this figure, Fermi level lies below the first subband energy level at the gate voltages below −3V and less, which indicates a considerable reduction of the 2DEG concentration of the gated-channel. It is worth noting that, based on the simulation results presented in Figures 3.3, 3.4 (a), and 3.7, the subband energy levels decrease with reducing the 2DEG carrier-concentration.

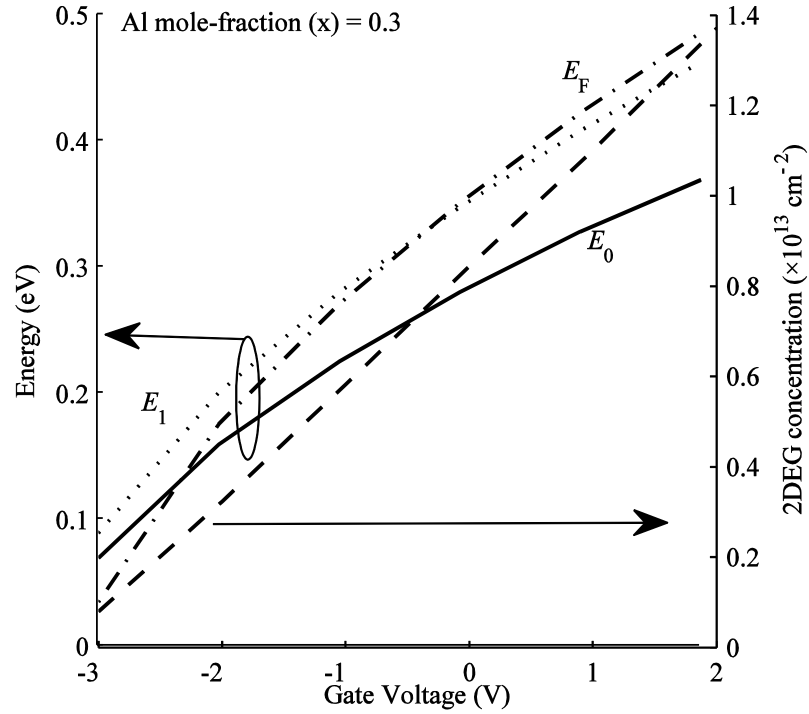

Figure 3.7 Variation of the 2DEG carrier concentration (dashed line), first (solid line) and second (dotted line) subband energy levels (E_0 and E_1), and Fermi energy level E_F (dash-dotted line) of a gated AlGaN/GaN heterojunction with gate voltage.

In the calculations reported based on the simplifying assumption of a triangular potential profile, the first and second subband energy levels are calculated according to,

$$E_{0,1} = \gamma_{0,1} n_s^{2/3} \tag{3.29}$$

where γ_0 and γ_1 are 2.12×10^{-12} and 3.73×10^{-12} eVm$^{4/3}$ [19], [20]. At relatively low 2DEG carrier-concentrations (e.g., Al mole-fraction of 0.15 and barrier thickness of 20 nm), the calculated subband energy levels based on the presented variational method and the triangular quantum well approximation are expected to match closely. This expectation is fed by the weaker polarization and consequently less pronounced band bending of the channel at lower values of Al mole-fraction and barrier thickness. However, as illustrated in Figure 3.2, at higher 2DEG concentrations applying the

triangular quantum well approximation results in miscalculation of the first excited subband energy level (i.e., higher than the conduction-band discontinuity). In other words, application of equation (3.29) with constant values of $\gamma_{0,1}$ is not capable of providing reasonable values for subband energy levels in AlGaN/GaN material system. This is specifically true when x > 0.15.

Table 3.1 The first and second subband energy levels as functions of 2DEG concentration, n_s (cm^{-2}), for different Al mole-fractions and barrier thicknesses. The functions are extracted through the interpolation of calculated values according to the proposed model. The spontaneous and piezoelectric constants used in these calculations are based on corrected values in [35].

Al mole-fraction	Energy levels	d_{AlGaN} = 10 nm	d_{AlGaN} = 20 nm	d_{AlGaN} = 30 nm
0.15	E_0	$-6\times10^{-26}n_s^2+10^{-13}n_s+0.0035$	$2\times10^{-39}n_s^3-10^{-26}n_s^2+6\times10^{-14}n_s+0.0226$	$10^{-39}n_s^3-10^{-26}n_s^2+6\times10^{-14}n_s+0.025$
	E_1	$2\times10^{-26}n_s^2+5\times10^{-14}n_s+0.0354$	$2\times10^{-39}n_s^3-2\times10^{-26}n_s^2+9\times10^{-14}n_s+0.0272$	$2\times10^{-39}n_s^3-10^{-26}n_s^2+8\times10^{-14}n_s+0.0309$
0.2	E_0	$-10^{-39}n_s^3-5\times10^{-28}n_s^2+5\times10^{-14}n_s+0.0292$	$7\times10^{-40}n_s^3-9\times10^{-27}n_s^2+6\times10^{-14}n_s+0.0257$	$6\times10^{-40}n_s^3-8\times10^{-27}n_s^2+6\times10^{-14}n_s+0.0262$
	E_1	$2\times10^{-39}n_s^3-2\times10^{-26}n_s^2+9\times10^{-14}n_s+0.0282$	$10^{-39}n_s^3-10^{-26}n_s^2+8\times10^{-14}n_s+0.0318$	$8\times10^{-40}n_s^3-10^{-26}n_s^2+8\times10^{-14}n_s+0.032$
0.3	E_0	$5\times10^{-40}n_s^3-8\times10^{-27}n_s^2+6\times10^{-14}n_s+0.0267$	$2\times10^{-40}n_s^3-4\times10^{-27}n_s^2+5\times10^{-14}n_s+0.0319$	$2\times10^{-40}n_s^3-4\times10^{-27}n_s^2+5\times10^{-14}n_s+0.033$
	E_1	$8\times10^{-40}n_s^3-10^{-26}n_s^2+8\times10^{-14}n_s+0.0333$	$3\times10^{-40}n_s^3-6\times10^{-27}n_s^2+7\times10^{-14}n_s+0.0422$	$2\times10^{-40}n_s^3-5\times10^{-27}n_s^2+6\times10^{-14}n_s+0.0412$
1.0	E_0	$5\times10^{-42}n_s^3-6\times10^{-28}n_s^2+3\times10^{-14}n_s+0.0572$		
	E_1	$6\times10^{-42}n_s^3-7\times10^{-28}n_s^2+4\times10^{-14}n_s+0.0771$		

As more accurate substitutes for equation (3.29), in evaluation of subband energy levels, a set of closed-form expressions, calculated on the basis of curve fitting among the data obtained through the proposed variational model, is provided in Table 3.1. As indicated earlier, since increase in Al mole-fraction limits the maximum thickness of the un-relaxed barrier [1], [56], in this table only a set of typically used barrier thicknesses and Al mole-fractions, which are not prone to strain relaxation, are considered.

3.4 Conclusion

A model based on the variational method for calculation of the first and second energy states, 2DEG carrier-concentration, and Fermi energy level of AlGaN/GaN heterojunctions is developed. Accordingly, variations of the aforementioned quantities with respect to barrier thickness, Al mole-fraction, background donor concentration, and gate voltage are studied for gated AlGaN/GaN heterojunctions. The applicability of the triangular quantum well approximation to AlGaN/GaN heterojunctions is also investigated by comparing the results of the variational method and this simplifying approximation. This investigation reveals the unsuitability of applying the triangular quantum well approximation to AlGaN/GaN heterojunctions. On the basis of the proposed variational method, closed-form expressions for the dependency of E_0 and E_1 on n_s, for a full set of experimentally realizable heterostructures, are proposed[4].

[4] These conclusions are reported in [57].

Chapter 4

Temperature-dependent investigation of low-frequency noise characteristics of Mesa-, Fin, and Island-Isolated AlGaN/GaN HFETs

4.1 Introduction

As alluded earlier, high breakdown-voltage, low switching loss, high electron saturation-velocity, and high sheet-carrier-concentration have made AlGaN/GaN HFET a suitable candidate for microwave and power electronics applications [9], [10]. As observed in chapter 2, the high sheet-carrier-concentration is the result of a sizeable discontinuity of the spontaneous polarization at the AlGaN/GaN heterointerface and a large piezoelectric polarization. It was also noted in chapter 2 that, this piezoelectric polarization is caused

by the combination of the sizeable built-in strain of the pseudomorphically grown AlGaN/GaN heterostructure and large piezoelectric coefficients in this material system [6]. This high sheet-carrier-concentration normally results in normally-on operation of AlGaN/GaN HFETs.

Increasing the value of the threshold-voltage , and the transition of the operation mode of these normally-on transistors to normally-off, have been proven to be challenging [11], [12]. Valizadeh and AlOtaibi have proposed that the concentration of the two dimensional electron gas can be selectively engineered by varying the size of the isolation mesa [18]. Accordingly, they have demonstrated fin- and island-isolated AlGaN/GaN HFETs for which the threshold-voltage is less negative (i.e., about 10% reduction in the threshold-voltage value), whereas the maximum DC current-density and gate transconductance are maintained at the same level. According to [18], the positive shift of the threshold-voltage observed in fin- and island-isolated AlGaN/GaN HFETs is the result of further development of peel forces around the edges of the islands and fins. Based on previous observations in SiGe technology [58], depending on the lateral dimensions of the mesa, development of these forces has been deemed capable of reducing the built-in strain even in the middle of the isolation feature by as much as fifty percent, and in-turn positive-shifting of the threshold-voltage in the polar AlGaN/GaN 2DEG channel. The extrinsic gate transconductance of these three aforementioned devices are shown in Figure 4.1. This figure clearly shows the positive shift in threshold-voltage from mesa- to fin- and island-isolated devices [18].

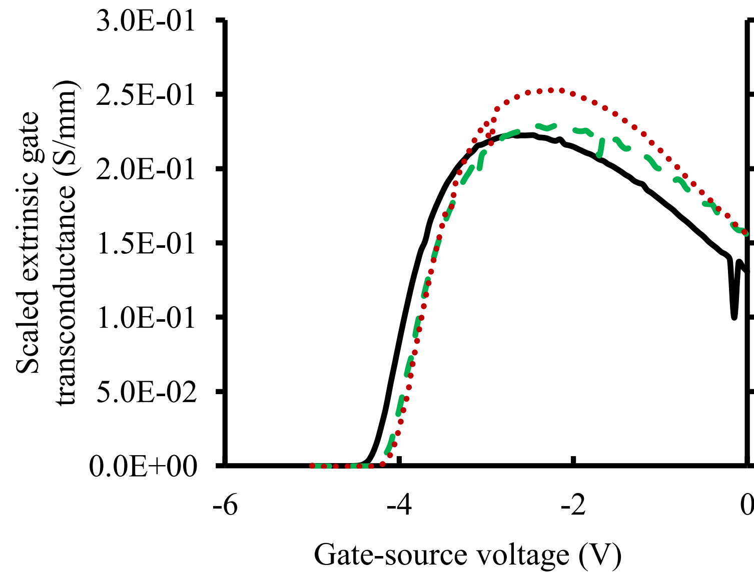

Figure 4.1 Scaled extrinsic gate transconductance versus gate voltage for three different device types of conventional mesa size (solid line), fin-isolated (dashed line), and island-isolated (dotted line) at room temperature, VDS is equal to 5 V [18].

An extended body of work hints towards a strong correlation between device technology, 1/f noise level, and emergence of generation–recombination bulge signatures [23], [26], [44], [45], [50], [59], [60]. This correlation has been demonstrated to provide a very sensitive basis for reliability and performance evaluation of electron devices [23], [26], [44]. Observation of G–R signatures and temperature-dependency of their corner frequencies have been used in evaluation of the energy levels of trap sites in a variety of semiconductor devices, including AlGaN/GaN HFETs [50]. Based on the proven suitability of low-frequency noise for performance evaluation of electronic devices, it is deemed necessary to study the low-frequency noise characteristics of the newly-proposed fin- and island-isolated AlGaN/GaN HFETs and compare these to conventional mesa-isolated devices. These studies specifically intend to reveal possible setbacks in performance that AlGaN/GaN HFET technology might face through replacing mesa-isolation by fin-, or island-isolation.

This work aims to investigate the drain and gate LFN-current characteristics of the newly-proposed devices at various temperatures (i.e., 150, 300, and 450 K) in order to address the possible difficulties in performance of the newly-proposed devices. The experimental results were analyzed using the number-fluctuation noise theory [45].

4.2 Device specifications and experimental setup

In this work, the LFN characteristics of AlGaN/GaN HFETs of three different structures are investigated. The first device type, which is referred to as "mesa-isolated", was fabricated on large mesa of size 70 µm × 100 µm. The second device type, which is referred to as "fin-isolated", was fabricated on long and narrow small mesa of size 16 µm × 40 µm, and the third device type, which is referred to as "island-isolated", was fabricated on an array of 14 small mesas of size 16 µm × 7 µm [18]. Figure 4.2 illustrates the schematics of these three device types. As shown in this figure, in island-isolated devices the gate, source, and drain electrodes, overlap larger etched surfaces in comparison to mesa- and fin-isolated devices. These surfaces include sidewalls of the islands and also etched surfaces of the buffer-layer. All these devices have gate length of 1 µm, gate-drain separation of 2 µm, and gate-source separation of 1.1 µm. Drain and source contacts were realized through a two-step metallization. The first metal layer overlaps the top surface of the isolation structure (i.e., mesa, fin, and island) only. Rapid thermal annealing was performed immediately after the first metallization step. As a result, the drain and source electrodes illustrated in Figure 4.2, make ohmic contacts to the top surface of the mesa, fin, and islands only.

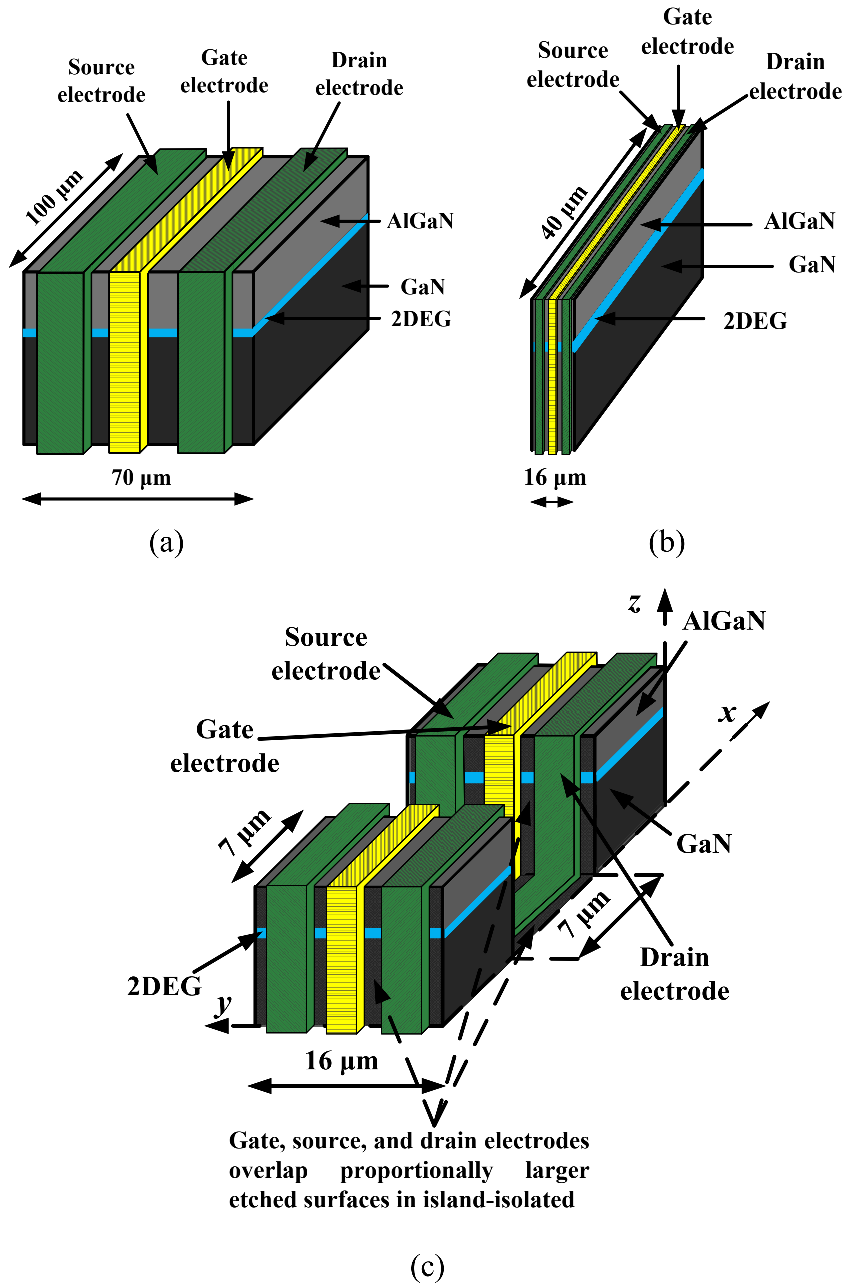

Figure 4.2 Three dimensional schematic of a conventional mesa-isolated device (a), a fin-isolated device (b), and an island-isolated device (c). Schematics illustrate that a proportionally larger overlap exists between the gate and ohmic electrodes and the additionally etched surfaces in the island-isolated devices. In case of the island-isolated device, the schematic is showing only the connection to two of the islands. Drawings are not in scale.

The second step of metallization, realizes the connection between the ohmic contacts and the measurement pads of each device. Further details are provided in [18].

On-wafer LFN characterization was performed by using a standard in-house developed measurement setup (Figure 4.3). The samples were placed in the temperature-controlled chamber of a MMR-LTMP4 probe station. This probe station can reliably maintain the lattice temperature at any temperature between 80 and 500 K. In order to eradicate the effect of undesired noise sources, batteries and wire-wound resistors were used as part of the bias circuit. Moreover, coaxial cables were used in order to prevent interfering noise sources. A low-noise amplifier with a voltage gain of 60 dB was used to amplify the noise spectral density. The amplified noise power spectral density was acquired by the dynamic signal analyzer HP35670A (using the Hanning window and 100 averages for the frequency range of 1 Hz–100 kHz and 50 averages for the frequency range of 0.1–1 Hz). The dynamic signal analyzer was calibrated by measuring the thermal noise of wire-wound resistors. Capacitors C_1 and C_2 are decoupling capacitors, which prevent possible unwanted noise from batteries and potentiometers from mixing with internal device noise. Capacitors C_3 and C_4 are AC coupling capacitors. The DC characteristics of the devices were collected by the semiconductor characterization system Keithley 4200-SCS. The drain (gate) noise-current was measured, while the gate (drain) terminal was AC grounded.

As it was mentioned in section 2.6, linear mode of operation is usually chosen for conducting low-frequency noise studies. Therefore, in this study a set of bias points in the early linear regime of operation is used in device characterization at three different temperatures of 150, 300, and 450 K. Considering the low-power dissipation under this

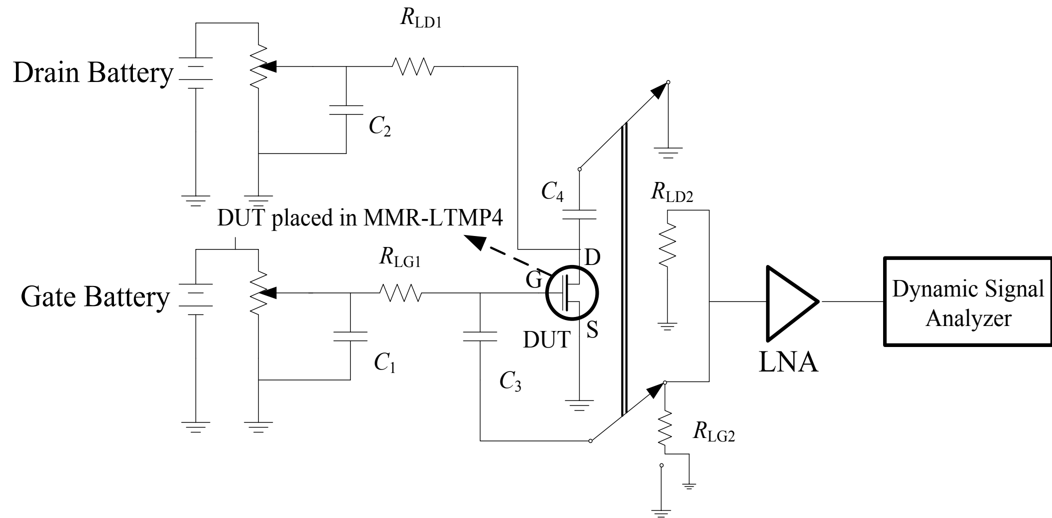

Figure 4.3 Standard low frequency noise measurement setup.

bias condition, self heating was not consequential. It is necessary to mention that the measurements were conducted in the order of room- , low-, and high-temperature for acquiring drain and gate noise-current characteristics. During measurements, the probe station chamber was operated under low pressure (i.e., less than 1 m Torr) and the chamber temperature was controlled and monitored by a temperature controller (MMR-K20). The prolonged period of time needed for performing measurements below 10 Hz rendered the noise studies of this frequency range at 150 K impossible. This is because the temperature controller could not maintain the low-temperature stability for this long period of time.

On each die, two devices of each type were chosen for characterization. In total, ten dies were used in this evaluation. The room-temperature DC characteristics of the devices of each type were identical (with less than two percent variation). The presented noise data are representative of the trends observed among these devices. It is necessary to mention that the variations of extrinsic gate-transconductance of the three aforementioned device

types versus gate voltage at room temperature show an equivalent positive transition of the threshold-voltage in the fin- and island-isolated devices with regards to mesa-isolated HFETs. These DC characteristics were presented in [18] by Valizadeh et al.

4.3 Experimental results and analysis

In the frequency range of 1 Hz–100 kHz a $1/f^{\gamma}$ characteristic, with a frequency exponent (i.e., γ) varying within the range of 0.9–1.2, was observed on the drain noise-current of all three device types at all temperatures. Figure 4.4 shows the temperature variation of the drain noise-current power spectral density, normalized drain noise-current[5] (at 10 Hz), and the frequency exponent for the aforementioned device types (i.e., mesa-, fin-, and island-isolated) for V_{DS} of 0.4 V, and two values of V_{GS} (i.e., 0 and -2 V).

In terms of the mobility-fluctuation noise theory, variation of the normalized 1/f noise level with the normalized effective gate-source voltage (defined as $(V_{GS}-V_T)/V_T$), has been shown to have the possibility of pinpointing the dominant noise source and resistance in the channel of a non-self-aligned field effect transistor [26]. Table 4.1 summarizes the framework of this evaluation. In this framework, S_{Access} and S_{ch} stand for noise spectral

Table 4.1 Summary of the criteria developed in [26] for determination of the dominant noise source S_R and dominant resistance along the channel R of a non-self-aligned FET.

		Noise Source	Dominant Resistance
$\frac{S_{ID}}{I_D^2} \propto$	$(V_{GS}-V_T)^2$	$S_R \cong S_{Access}$	$R \cong R_{Ch}$
	$(V_{GS}-V_T)^0$	$S_R \cong S_{Access}$	$R \cong R_{Access}$
	$(V_{GS}-V_T)^{-1}$	$S_R \cong S_{Ch}$	$R \cong R_{Ch}$
	$(V_{GS}-V_T)^{-3}$	$S_R \cong S_{Ch}$	$R \cong R_{Access}$

[5] Normalized noise-current is defined by the ratio of noise-current spectral density and the square of the DC current of the terminal (i.e., in case of drain noise current: S_{ID}/I_D^2).

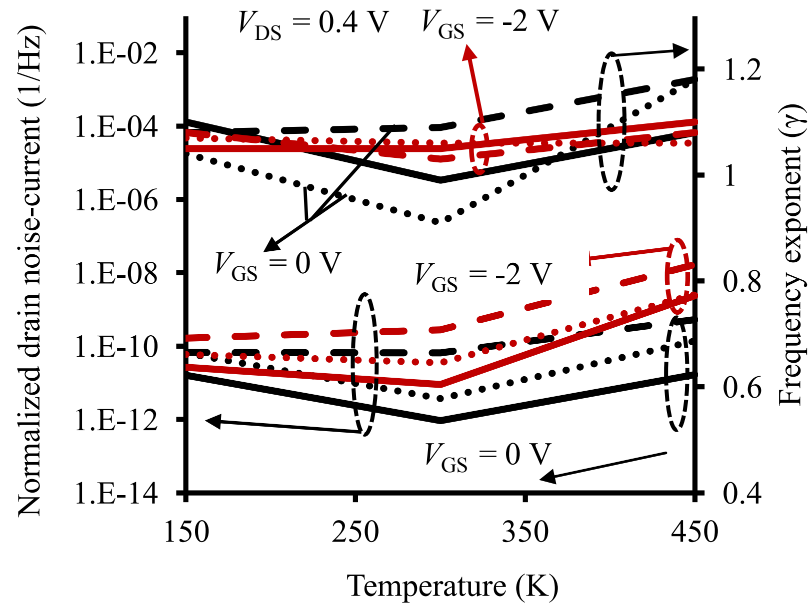

(a)

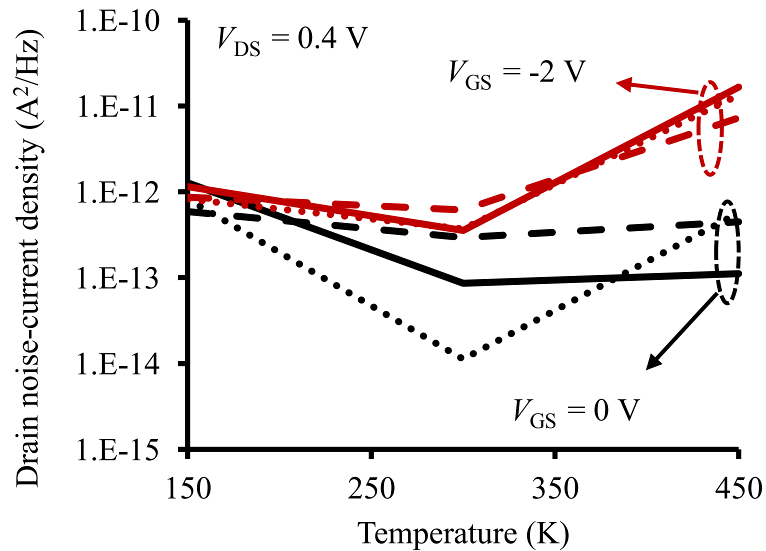

(b)

Figure 4.4 Variation of the normalized drain noise-current level and frequency exponent (i.e., γ) at 10 Hz versus temperature for mesa-isolated (solid line), fin-isolated (dashed line), and island-isolated devices (dotted line) at two different bias points, V_{GS} = 0, V_{DS} = 0.4 V and V_{GS} = -2, V_{DS} = 0.4 V (a). Drain noise-current power spectral density is presented in (b).

density of the access- and the gated-channel, respectively. In addition, R_{Access} and R_{ch} stand for the resistance of the access- and the gated-channel, respectively.

In order to assess the applicability of this noise theory, the observed low-frequency noise profiles have been investigated according to this framework. While this framework is based on the mobility fluctuation theory, the disagreements observed between the expected trends of this framework and the experimental data, hinted towards the adoption of the alternative LFN theory (i.e., number fluctuation theory).

According to this investigation, Figure 4.5(a) demonstrates that, at room temperature, the normalized drain noise-current of all three device types have an exponential dependency on the normalized effective gate-source voltage with an exponent of about -3 (the exponent is about -1.7 for fin-isolated device at lower gate voltages). This indicates that, at room temperature, for mesa- and island-isolated device types, the dominant resistance is the access-channel resistance and the dominant noise source is that of the gated-channel. This observation is true for the fin-isolated device at higher gate voltages. As shown in Figure 4.5 (b), a noticeable difference is, however, observed at 150 and 450 K. According to this framework, Figure 4.5 (b) indicates that as the temperature was reduced from 300 K to 150 K, in mesa- and fin-isolated HFETs, the gated-channel resistance became larger than the resistance of the access region (whereas this part of the channel maintains its dominance on noise spectral density). However, with this reduction in temperature, an improvement in carrier mobility and a proportionally equal improvement in the conductivity of both parts of the channel (i.e., access- and gated-channel) are expected. As a result, a swap in the dominance of R_{ch} and R_{access} is not expected. In addition to this discrepancy, it is observed that the exponents indicated in Figure 4.5 (b) at 450 K are not expected from the framework presented in Table 4.1. According to these observations, it is concluded that the low-

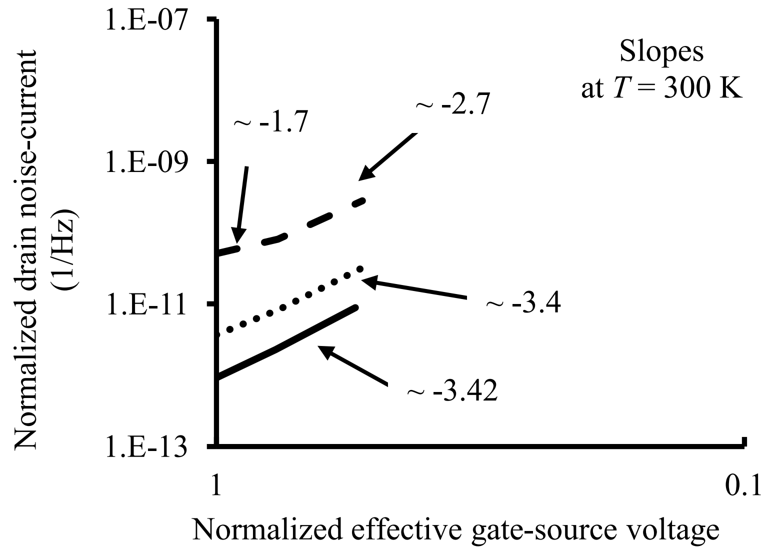

(a)

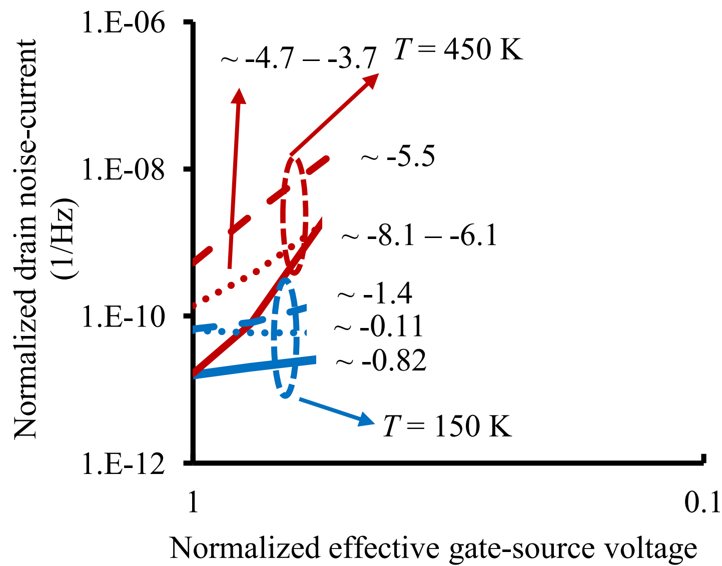

(b)

Figure 4.5 (a) Variation of the normalized drain noise-current level at 10 Hz versus normalized effective gate-source voltage, at room temperature, for V_{GS} = 0, -1, and -2 V and V_{DS} = 0.4 V, for mesa- , fin- , and island-isolated devices. (b) Variation of the normalized drain noise-current level at 10 Hz versus normalized effective gate-source voltage, at 150 and 450 K for the same devices as (a). Mesa-, fin-, and island-isolated devices are represented by solid-, dashed-, and dotted-lines, respectively.

frequency noise characteristics of these devices are incompatible with the mobility fluctuation noise theory.

In spite of the adoption of this theory, dimensionless Hooge's parameter (i.e., α_0) is also calculated. The calculated value of this parameter is about 10^{-4}, which is within the range reported by others [50].

In spite of the observation of a drain LFN characteristics closely following the 1/f power spectral density at frequencies above 1 Hz, low-frequency noise measurements in lower frequency decades revealed a $1/f^2$ spectral density in island-isolated HFETs.

As interestingly observed in Figure 4.6, although both mesa- and fin-isolated devices show a 1/f noise spectrum within the entire frequency range, the island-isolated device shows a G–R bulge signature in the first frequency decade, with a corner frequency lower than 0.1 Hz.

According to the device structures illustrated in Figure 4.2, the drain-, source-, and gate-electrodes of the island-isolated devices have proportionally larger interfaces with etched surfaces on GaN buffer-layer and also larger number of etched sidewalls. The link between the physical dry etch and defect formation in a semiconductor has been reported by many investigators [61] - [65]. Whereas the only difference in the fabrication process of the three device types is with respect to the lateral definition of the isolation feature, it seems convincing that any difference in performance can be safely linked to this unique difference in fabrication technology. Accordingly, it is deemed that the excess G–R noise observed in the lower frequency decades of the drain LFN of island-isolated devices is due to the involvement of the relatively deep trap levels, introduced by the physical etch, in fluctuation of the number of carriers through a trapping/de-trapping mechanism.

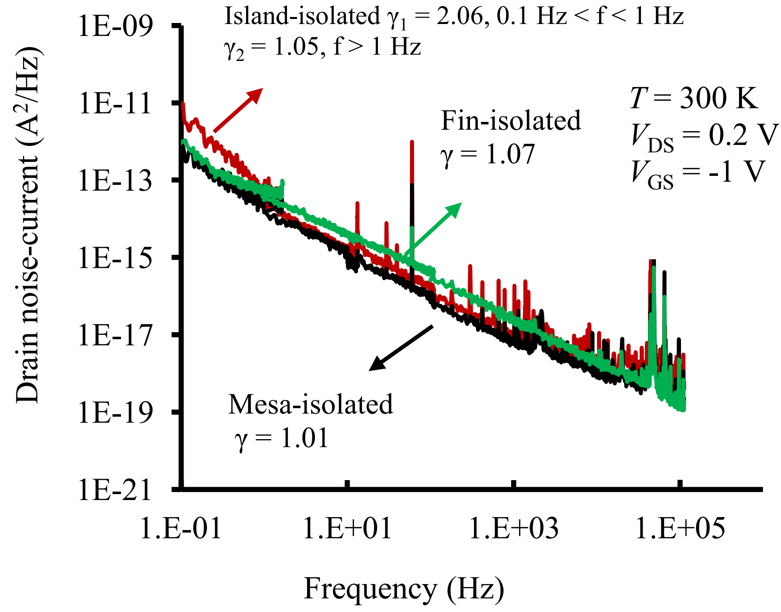

Figure 4.6 A comparison of room temperature drain noise-current spectral density among the three different device structures biased at V_{GS} = -1 V, V_{DS} = 0.2 V.

According to number fluctuation theory, the spectrum of the G–R noise follows a Lorentzian profile of (2.12). The corner frequency of (2.12), which is identified by this relaxation time constant, is temperature-dependent according to the modified Arrhenius characteristics of the form,

$$\tau = \frac{\beta}{T^2} \exp\left(\frac{E_A}{kT}\right), \tag{4.1}$$

where E_A is the trap energy level and β is the proportionality constant.

As a result, studying the temperature-dependent variation of this corner frequency can be used in evaluation of the energy level of the responsible trap site. According to (2.12) and (4.1), with elevation in temperature, the corner frequency caused by a single trap level is increased, while the amplitude of the Lorentzian reduces. Consequently, reducing the temperature below 300 K, results in the shift of the corner frequency further below 0.1 Hz. As indicated earlier, performing low-frequency noise measurements at low

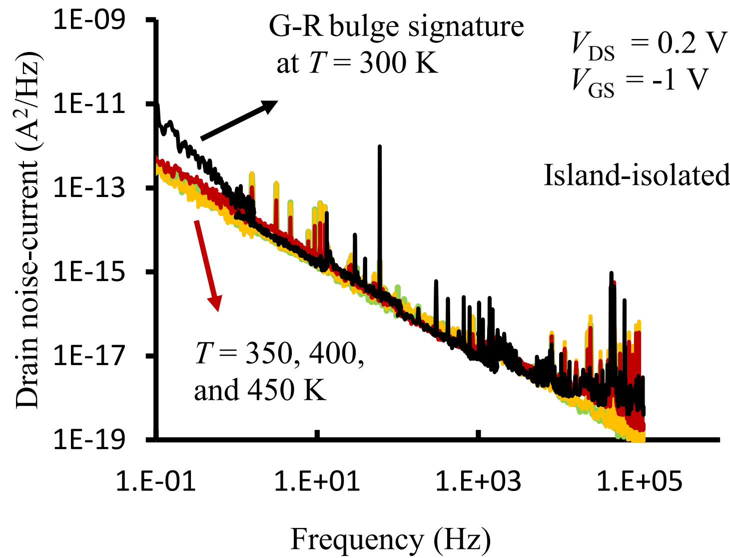

Figure 4.7 Drain noise-current level of the island-isolated HFET at 300, 350, 400, and 450 K. A G–R bulge signature is detected at room temperature.

temperatures for this frequency range was not possible. As a result, in order to observe and track the variation of the corner frequency with temperature, the drain LFN current at a number of temperatures higher than 300 K was studied. However, as shown in Figure 4.7, at temperatures above 300 K the G–R signature is submerged by the 1/f noise spectrum. This is due to the aforementioned reduction of the G–R noise level with increased temperature. Consequently, in spite of the observation of a $1/f^2$ spectrum, the drain LFN profile does not yield the possibility of observing a clear corner frequency. Since it is speculated that this G–R signature is the outcome of a proportional increase in overlap between the electrodes and the etched surfaces of an island-isolated device, the gate noise-current is expected to be able to complement these observations.

Figure 4.8 shows the variation of the normalized and un-normalized gate noise-current of the three device types. As illustrated in this figure, at 150 K the island-isolated HFET shows a pronounced Lorentzian profile with a clear corner frequency at 120 Hz. Lack of observation of Random Telegraph Signal (RTS) noise in time domain observations of the

gate current, confirms that this Lorentzian is caused by a G–R noise. As shown in Figure 4.8, at temperatures higher than 150 K this G–R signature is also submerged under a 1/f spectrum. Although this prevents us from calculating the trap-energy level responsible for this G–R bulge signature, observation of this clear corner frequency can be used to evaluate the possibility of high frequency operation of these devices. The approach of applying the Arrhenius characteristic to LFN measurements for AlGaN/GaN HFETs, in order to investigate trap characteristics, has been also reported in [65].

As illustrated in Figure 4.8 (a), island-isolated devices present the highest level of gate noise-current. However, due to higher gate-leakage current of these devices, they present a lower level of normalized gate noise-current among the three device types.

Current dispersion and gate-lag are among the limiting factors in commercialization of AlGaN/GaN HFETs [66] - [70]. These effects are partially linked to the presence of surface states at the exposed AlGaN or GaN surfaces. Whereas presence of G–R signatures in the drain and gate noise-current of the newly-proposed island-isolated HFETs, is suggestive of the existence of charge trapping/de-trapping centers, it seems convincing that presence of this observation in island isolated HEFTs and lack of it in the other two device types should be linked

to the difference in their fabrication technology. Since the only difference in the fabrication technology of these three device types can be summarized in terms of the further exposure of electrodes to GaN etched surfaces and isolation-feature sidewalls in island-isolated devices (shown in Figure 4.2), it is convincing that these trapping/de-trapping centers have been created by the damaging effect of dry-etching process on these surfaces. The existence of such surface-

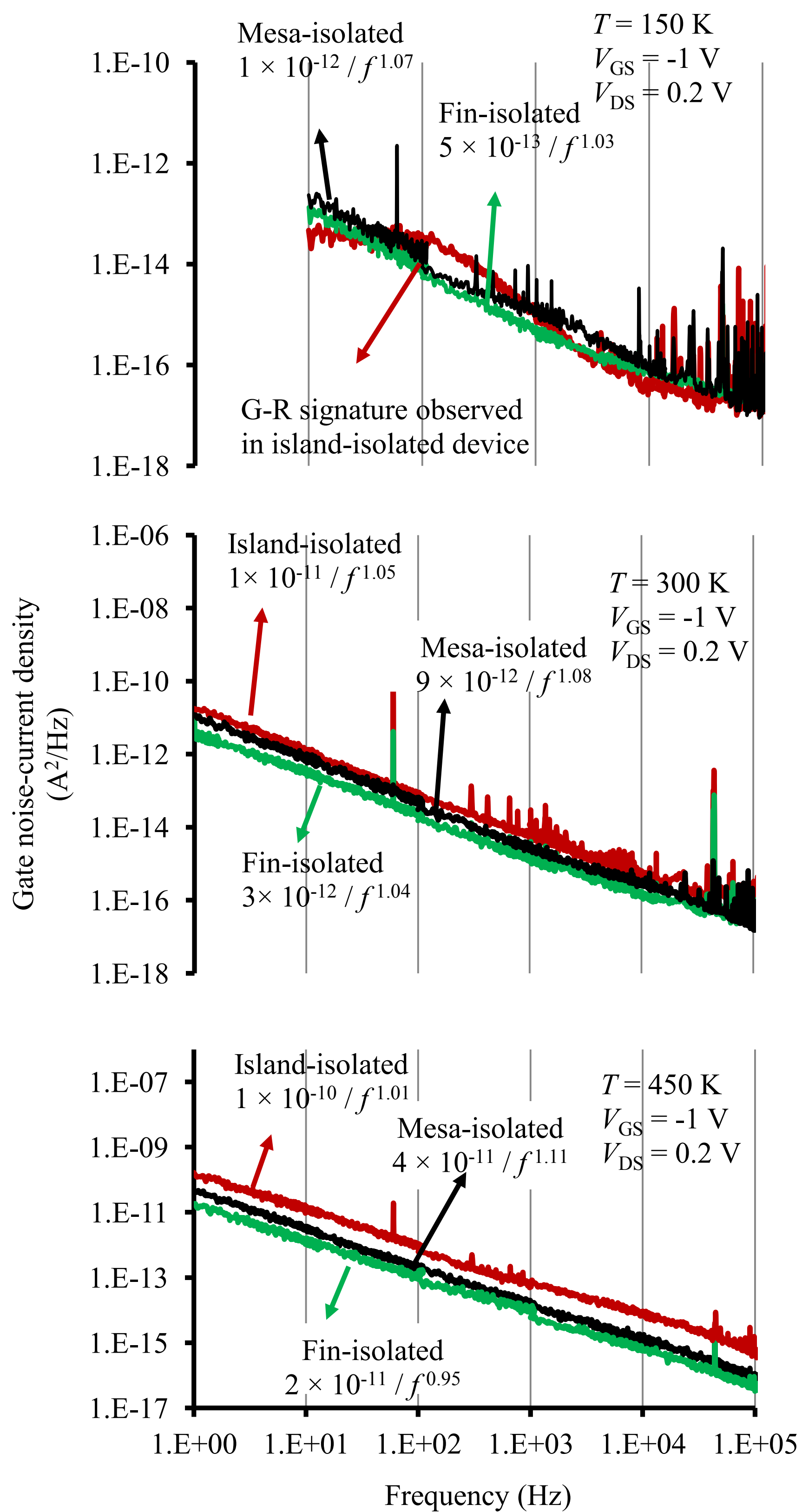

(a)

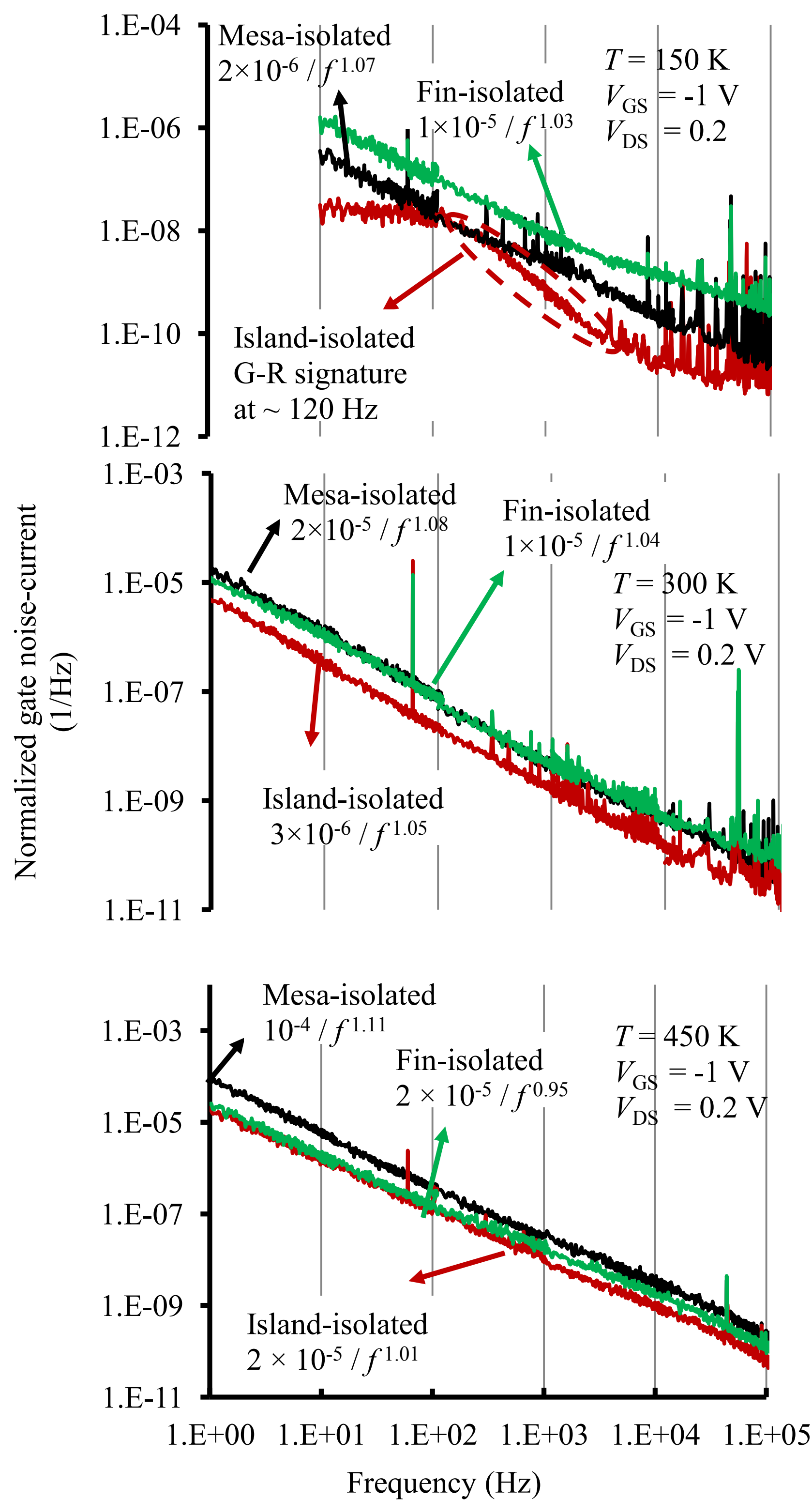

(b)

Figure 4.8 Gate noise-current power spectral density of mesa-, fin-, and island-isolated devices at T = 150, 300, and 450 K at V_{GS} = -1 V and V_{DS} = 0.2 V (a). The normalized characteristics are presented in (b).

states provides the possibility of evaluating a range of limiting trapping/de-trapping time constants, contributing to high frequency drain current dispersion in these devices.

The trapping/de-trapping time constants affecting this device type are calculated based on a number of reported trap levels. These trap levels are tabulated in Table 4.2. With exception of trap levels reported from [65], others have been clearly linked to ICP etching of GaN.

According to (4.1), a link between the trap relaxation time constants at two different temperatures of measurement and trap energy level can be established in the form,

$$E_A = \frac{k}{\frac{1}{T_2} - \frac{1}{T_1}} Ln\left(\frac{\frac{\tau_2}{\tau_1}}{\left(\frac{T_1}{T_2}\right)^2}\right) \tag{4.2}$$

Whereas the 150 K gate noise-current suggests a corner frequency of 120 Hz (i.e., a relaxation time constant of about 8.3 ms), the relaxation time constant at a different temperature can be calculated using (4.2). Table 4.3 shows the result of evaluation of these trapping/de-trapping time constants at 300 and 450 K, based on the assumption of a few of the trap levels identified in Table 4.2. It should be mentioned that the calculation of trapping/de-trapping time constants using Table 4.2 is only a zero-order attempt. Because the corner frequency of the G–R signature observed in Figure 4.8 is relatively high, only a few of the shallow traps are considered. As shown in this table, extensive ICP etching in the vicinity of the active area of an island-isolated HFET and overlap of the electrodes with these surfaces result in trapping/de-trapping time constants as long as a few microseconds at room temperature. This can have adverse effects on the high frequency operation of these devices.

Table 4.2 Reported values of trap levels due to ICP dry etching of the buffer-layer.

Reference	Trap energy level (eV)
[63], [65]	E_C-(0.17)
[61]	E_C-(0.211)
[64]	E_C-(0.23)
[62], [63], [65]	E_C-(0.25)
[61]	E_C-(0.253)
[65]	E_C-(0.33)
[63]	E_C-(0.34)
[63], [65]	E_C-(0.44)
[64]	E_C-(0.55, 0.58)
[63]	E_C- (0.61)
[62]	E_C-(0.62)
[65]	E_C-(0.71)
[63]	E_C-(0.72, 0.9)

Table 4.3 Calculated time constants at 300 and 450 K based on the relaxation time constant at 150 K and relatively shallow trap levels.

Energy level (eV)	Time constant at 150 K (ms)	Time constant at 300 K (μs)	Time constant at 450 K (ns)
0.17	8.3	2.93	140
0.211	8.3	0.6	17.5
0.23	8.3	0.28	6.5
0.25	8.3	0.13	2.3
0.253	8.3	0.11	2

Whereas according to [18] island- and fin-isolated AlGaN/GaN HFET technologies perform equally well with regards to positive shifting of the threshold-voltage, island-

isolation shows a slightly superior DC gate-transconductance and self-heating performance. From the high frequency operation point of view, however, the current study reveals signatures of performance limitation in island-isolated HFETs. In terms of the data presented in this study, the operation of island-isolated AlGaN/GaN HFETs are expected to be more limited by the gate-lag and current dispersion. These effects have been illustrated to limit the transistor's dynamic load-line at microwave frequencies, and as a result reduce the high-frequency power gain to values much smaller than expected from the DC characteristics [70]. In the traditional mesa-isolated AlGaN/GaN HFET technology, passivation of the exposed AlGaN surfaces has been demonstrated to have the possibility of partially eliminating these problems [66]. As a result, for improving the island-isolated AlGaN/GaN HFET technology surface passivation of the etched surfaces before metallization is recommended.

4.4 Conclusion

Low-frequency noise characteristics of conventional mesa-isolated and the newly-proposed fin- and island-isolated AlGaN/GaN HFETs were experimentally studied in a wide range of temperatures. At room temperature, the island-isolated device showed a G–R bulge signature in its drain low-frequency noise characteristics with a corner frequency below 0.1 Hz. Another G–R signature with a corner frequency of about 120 Hz was also observed in the gate noise-current characteristic of this device type at 150 K. These types of signatures were absent from the gate and drain low-frequency noise spectra of mesa- and fin-isolated HFETs. As a result, observation of G–R signatures is believed to be the result of the larger interface of the device electrodes to additionally dry-etched sidewalls

of the islands and GaN surfaces. Whereas fin- and island- isolated HFETs have been both presented as equivalent alternatives for positive-shifting the threshold-voltage, the G–R signatures revealed in this study provide evidence for superiority of high-frequency operation of fin-isolation technology[6].

[6] These conclusions are published in [71].

Chapter 5

Physics-based analysis of low-frequency drain noise-current in $Al_xGa_{1-x}N/GaN$ HFETs

5.1 Introduction

As mentioned already in chapter 2, the study of low-frequency noise characteristics of III-V heterojunction field effect transistors under the early linear regime of operation is known to be one of the most promising and reliable approaches for pinpointing device reliability issues [23] -[26]. As a result of the growing interest in high-frequency/high-power applications of polar $Al_xGa_{1-x}N/GaN$ HFETs and in the wake of the proven existence of crystal imperfections and reliability concerns in this relatively new technology, the investigation of LFN characteristics of these devices has gained

significant attention.

The origins of the low-frequency noise, particularly 1/f noise, have been the topic of a vibrant scientific endeavor, which has resulted in a number of competing theories [44]. Among these theories, carrier-number fluctuation [45] and mobility fluctuation [46] are the two most accepted theories. The first theory is based on the superposition of the carrier Generation-Recombination Lorentzian profiles, with a fairly dense distribution of fluctuation time constants. The interpretation of this process in various technologies including III-V HFETs is possible through incorporation of thermally-activated trapping and de-trapping in the buffer-layer, and electron tunneling to the trap levels within both the buffer and barrier-layers [72] - [79]. As pointed out earlier in section 2.6 of this thesis, the interpretation of mobility-fluctuation theory, however, is based on an empirical relationship and is not supported by a solid theory. Since the results presented in chapter 4, favor the application of the number fluctuation noise theory, the present model follows the principles of this theory.

The theoretical noise calculations that have been so far presented in AlGaN/GaN HFET technology attempt to address the presence of non-fundamental 1/f noise purely on the basis of number fluctuation theory considering the tunneling of the carriers of two dimensional electron gas channel to trap sites of GaN [78], [79]. In addition, the theoretical calculations discussed in chapter 3, which emphasized on the presence of very strong piezoelectric effect and spontaneous polarization at polar AlGaN/GaN heterointerface have revealed a conduction-band bending much less lenient than other III-V HFETs to the approximations of rectangular or triangular potential wells.

In this work, a realistic non-fundamental low-frequency noise model is developed for

AlGaN/GaN polar HFETs by calculating the first and second subband energy levels of the 2DEG channel and considering both components of number fluctuation noise theory (i.e., tunneling and thermally-activated processes) and fundamental differences between polar AlGaN/GaN HFETs and other field effect transistor technologies[7]. These fundamental differences, as expressed in chapter 3, are taken into account through incorporation of the sizeable spontaneous and piezoelectric polarizations at the AlGaN/GaN heterointerface, which result in a significant distinction of the conduction-band bending, 2DEG carrier-concentration, and also carrier confinement in these HFETs. The theoretical model is validated through experimental means. An extensive set of experimental LFN data in a wide range of temperatures is employed for this purpose.

5.2 Theoretical model

The theoretical approach of this work starts with identifying the potential profiles, 2DEG carrier-concentration, and position of the first and second subband energy levels in 2DEG system in the buffer-layer near AlGaN/GaN interface. This task is initially carried out under thermal equilibrium. Following this, the impact of bias is then factored-in in calculating these parameters at different positions along the channel of the device. Then the two aforementioned thermally-activated and tunneling trapping/de-trapping processes of charge carriers are used to evaluate the variation of LFN spectrum with varying bias and temperature.

As mentioned in chapter 3, assuming a triangular potential well inside the channel/buffer-layer (i.e., GaN) and at the heterointerface does not yield a realistic basis for the

[7] This model has been published in [80] and [81].

calculations of the subband energy levels and 2DEG carrier-concentration. Therefore, the potential profile, the first, and the second subband energy levels are calculated by using the variational method, which considers the actual potential profile.

5.2.1 Carrier-concentrations in 2DEG

Figure 5.1 provides a schematic cross-sectional view of a non-self-aligned AlGaN/GaN HFET. As illustrated in this figure, the 2DEG channel, formed at the AlGaN/GaN heterointerface, consists of three regions (i.e., gated-channel, source-, and drain-access).

Thermal equilibrium behavior of the device is evaluated through calculation of the total 2DEG concentration (n_s), Fermi energy level (E_F), and the first and second subband energy levels (E_0 and E_1) with respect to the lower edge of the conduction-band of GaN at the heterointerface along the channel. While the foundations of these calculations for a gated HFET are already provided in chapter 3, with reference to those discussions, in this section the differences in light of presence of access regions and drain-source bias are elaborated.

Starting from an initial position assumed for the Fermi level (i.e., the lower edge of the conduction-band of GaN at the heterointerface), (3.26) is applied.

The polarization-induced 2D charge density at the polar AlGaN/GaN heterointerface is provided by (3.27). As expressed in chapter 3, considering the density of states of the first two sub-bands formed at the polar AlGaN/GaN heterointerface, (3.28) must also be satisfied.

The Fermi energy level E_F at thermal equilibrium is calculated by gradually increasing its initial position (i.e., the bottom of the conduction-band of GaN at the heterointerface)

until (3.26) and (3.28) converge. The overall flowchart of the method used in recursive calculations of n_s and the subband energy levels, which will be used for the calculation of noise, is presented in Figure 5.2.

The process of finding Fermi energy level, the subband energy levels, and the 2DEG carrier-concentration, which is repeated in each of the three regions of the channel, is indicated as process P in the flowchart of Figure 5.2. In these calculations, the threshold-voltage is considered as the gate-source voltage required to deplete the channel of polarization-induced 2DEG (i.e., $n_s << \sigma/e$). Considering (3.26), the threshold-voltage is calculated according to,

$$V_T = -\sigma \frac{d_{AlGaN}}{\varepsilon_0 \varepsilon_{GaN}} + E_F + \frac{e\varphi_b - \Delta E_C}{e} \tag{5.1}$$

The linear regime of operation is deemed most useful for the analysis of LFN characteristics. This is because ambiguities contributed by factors present in saturation

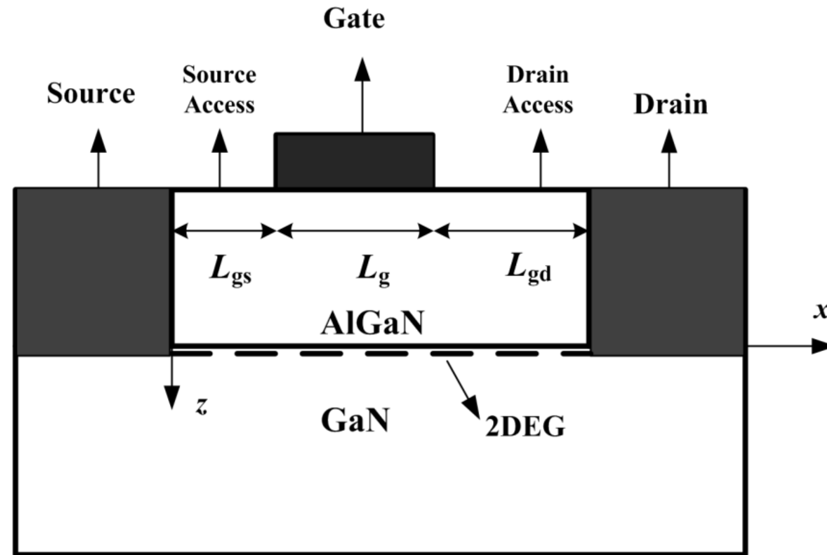

Figure 5.1 Cross-sectional view of a non-self-aligned polar AlGaN/GaN HFET. The lengths of gated-channel, source- and drain-access regions are identified as L_g, L_{gs}, and L_{gd}, respectively.

mode of operation such as velocity saturation, pinch-off, and self-heating render the noise analysis unnecessarily complicated and unreliable. Under early linear regime of operation for HFETs of relatively long gate length, it is simply expected that the current inside the channel is a low-field drift-only current. As a result, the channel potential at the boundaries of each of the three regions of the channel is evaluated in terms of the voltage-division in a linear resistive ladder. Accordingly, based on the length and 2DEG carrier-concentration calculated at thermal equilibrium in each region of the channel, the drain voltage-drop in each region under non-thermal equilibrium condition ($V_{\mathrm{DS}} > 0$) is calculated. Evolution of a finite potential across the channel (i.e., $\varphi_{ch}(x)$), however, requires this potential to be considered in calculation of 2DEG carrier-concentration.

This is done through modifying $\varphi_b - V_{GS}$ to $\varphi_b - V_{GS} - \varphi_{ch}(x)$ in (3.26).

Whereas in this section a generic framework has been presented, it is note-worthy that the process of calculating the quantum well characteristics is carried out according to the technologically-defined parameters of the device (i.e., Al mole-fraction, barrier thickness, Schottky barrier height, etc.). These technological parameters influence the calculated variational parameter b, and hence the 2DEG characteristics.

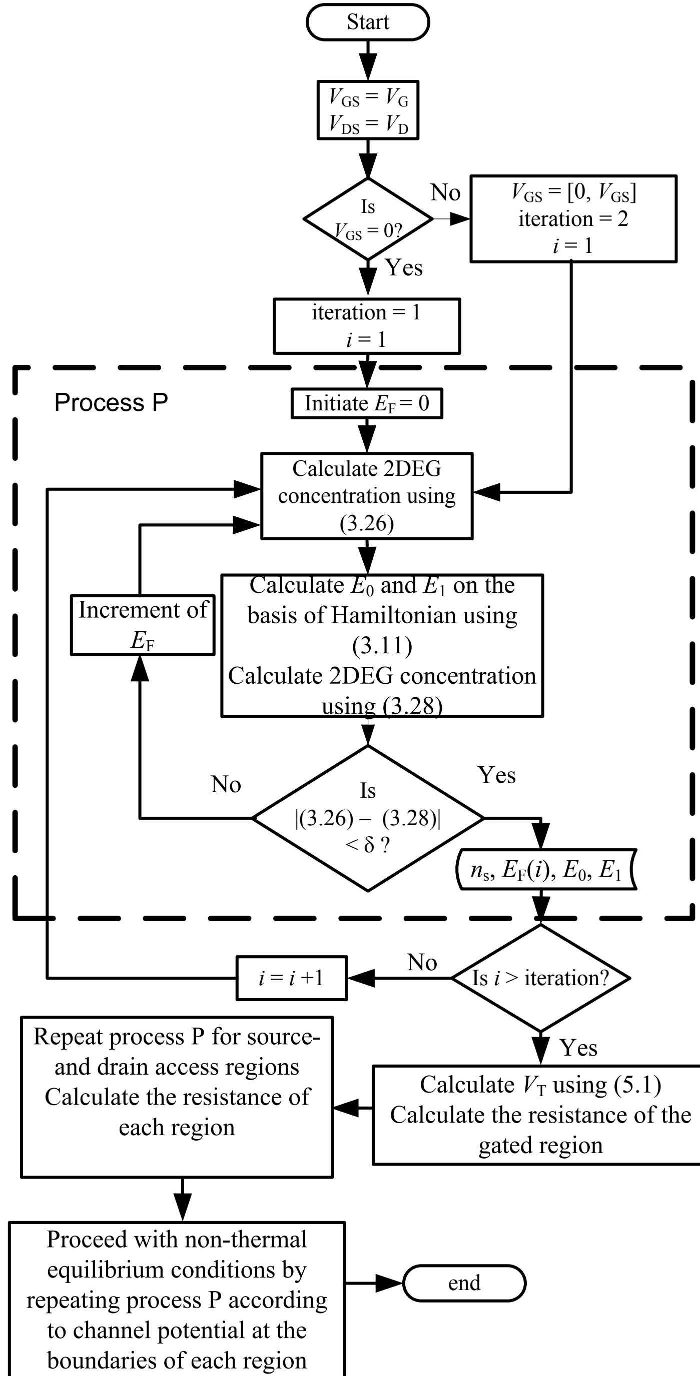

Figure 5.2 Overall flowchart indicating the method used in the calculation of the first and second subband energy levels (E_0 and E_1), Fermi level (E_F), threshold-voltage (V_T), and quasi Fermi level (i.e., E_{Fn}). These calculations are carried out before evaluation of low-frequency noise profile. Process P is repeated for all three regions of the channel under thermal equilibrium and non-thermal equilibrium according to the potential drop in each region.

5.2.2 Low-frequency drain noise-current

As mentioned earlier, the low-frequency noise can be interpreted in terms of the number fluctuation noise theory, which takes into account the effect of two processes: 1) the thermally-activated process, which considers the accumulative effect of G-R noise caused by trapping/de-trapping of the carriers into and out of a continuous band of trap sites inside the buffer-layer, which is spatially confined in the vicinity of the heterointerface, and 2) tunneling of the 2DEG carriers directly into and out of trap sites located in the barrier-layer.

The Lorentzian power spectral density represents the mean-square fluctuation in the carrier population attributed to an individual trap level and is calculated as,

$$S_N(f) = \frac{4\,\overline{\Delta N^2}\,\tau}{1+4\pi^2 f^2 \tau^2}, \tag{5.2}$$

where, $\overline{\Delta N^2}$ is the variance of the fluctuation in the number of carriers, τ is the relaxation time constant assigned to a single trap level, and f is the frequency [43]. A G-R spectrum caused by multiple discrete trap levels, however, can be calculated according to [76],

$$S_N(f) = \sum_i \frac{4\,\overline{\Delta N_\iota^2}\,\tau_i}{1+4\pi^2 f^2 \tau_i^2}, \tag{5.3}$$

where $\overline{\Delta N_\iota^2}$and τ_i are the variance of the fluctuation in the number of carriers and fluctuation time constant of each single trap level, respectively.

In evaluation of noise power spectral density due to the presence of a continuous distribution of relaxation time constants, (5.3) evolves to,

$$S_N(f) = \int_{\tau_l}^{\tau_h} \frac{4\,\overline{\Delta N^2}\,\tau g(\tau) d\tau}{1+4\pi^2 f^2 \tau^2}, \tag{5.4}$$

where $g(\tau)d\tau$ is the distribution function of the relaxation time constants [44], and τ_l and τ_h are the boundary values of the fluctuation time constants.

5.2.2.1 Tunneling process

Evaluation of the tunneling mechanism starts by defining a trap distribution N_{T-tn} inside the barrier-layer. In an elemental volume dV and in a narrow band of traps (i.e., dE), we have

$$d\overline{\Delta N^2} = N_{T-tn}.f_t.(1-f_t)dVdE, \tag{5.5}$$

where f_t is the occupation probability of a trap state defined according to Fermi-Dirac statistics.

Figure 5.3 illustrates the conduction band diagram of an AlGaN/GaN HFET (Figure 5.3(a)), along with a schematic which illustrates the difference between the height of the barrier seen by impinging carriers resulting in noise at very low- and relatively higher frequencies (Figure 5.3(b)). The tunneling fluctuation time constant associated with the i-th subband energy level with respect to z is given by [48],

$$\tau_{tn_i} = \frac{1}{C_i(\frac{n_{s_i}}{\Delta d_i})}, \tag{5.6}$$

where Δd_i is the approximate thickness of the i-th subband energy level (based on the calculation of the average thicknesses for the first and second subband energy levels), and C_i is the capture probability of traps located in the barrier at distance z from the heterointerface, which is associated with the i-th subband energy level and calculated according to WKB approximation,

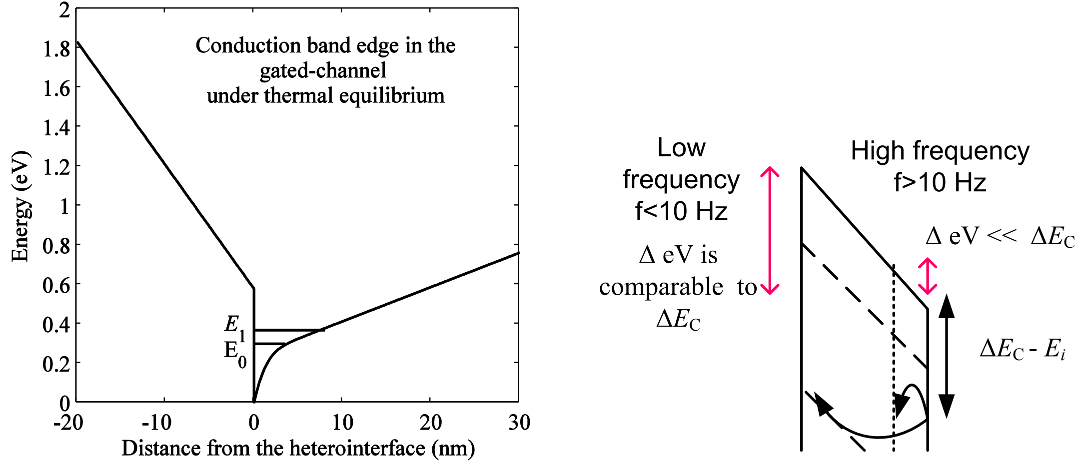

Figure 5.3 (a) Calculated conduction-band diagram of an AlGaN/GaN heterojunction with indication of the first and second subband energy levels and (b) Comparison of the barrier seen by an impinging electron at relatively low and high frequency ranges in the tunneling model of the LFN. At very low frequencies (e.g., f <10 Hz) the height difference in conduction-band edge of the barrier becomes comparable to the barrier (e.g., $\Delta E_C - E_i$).

$$C_i(z) = C_0 \exp\left[-\frac{4\sqrt{2m^*_{AlGaN}}}{3.eF.\hbar}.\left((eF.z + \Delta E_C - E_i)^{\frac{3}{2}} - (\Delta E_C - E_i)^{\frac{3}{2}}\right]\right. \tag{5.7}$$

where F is the electric-field inside AlGaN (i.e., $F = \frac{\sigma - e.n_S}{\epsilon_0 \epsilon_{AlGaN}}$), E_i is the i-th subband energy level, and C_0 is the capture coefficient. Using principle of detailed balance [82]

$$C_0 = \frac{\nu_0(T)}{N_{C(AlGaN)}}, \tag{5.8}$$

where $N_{C(AlGaN)}$ is effective density of states at the lower edge of the conduction-band of the barrier, and ν_0 is the attempt-to-escape frequency (assumed as 10^{12} Hz at room temperature, which varies with temperature according to $\upsilon_0(T) = \upsilon_0(300K).(T/300)^2$). According to (5.6) – (5.8), the fluctuation time constants associated with the tunneling of the 2DEG carriers (in both subband energy levels) into and out of the trap sites inside the barrier-layer are only z-dependent.

Considering the accumulative effect of tunneling process, the normalized noise power spectral density due to the tunneling mechanism is

$$\frac{S_{I-TN}(f)}{I_D{}^2} = \frac{S_{N-TN}(f)}{N_{tot}^2} = \frac{1}{W^2\left(\int_0^{L_{gs}+L_g+L_{gd}} n_s(x)dx\right)^2} \times$$

$$\int_0^{L_{gs}+L_g+L_{gd}} \int_0^{d_{AlGaN}} \int_0^{\Delta E_C} \frac{4\, W\, \tau_{tn}(x,z) N_{T-tn}(z,E)\; f_t(x).[1-f_t(x)]}{[1+4\pi^2 f^2 \tau_{tn}^2(x,z)]} dEdz \quad (5.9)$$

where $S_{I-TN}(f)$ is the total noise power spectral density due to the tunneling process, I_D is the drain dc current, $n_s(x)$ is the 2DEG carrier-concentration at position x along the channel, W is the width of the HFET, $L_{gs} + L_g + L_{gd}$ is the total length of the channel, and τ_{tn} is the fluctuation time constant due to the tunneling process in the channel.

5.2.2.2 Thermally-activated process

Evaluation of the elemental charge fluctuations, $d\overline{\Delta N^2}$, according to the thermally-activated trapping/de-trapping process is formulated through employing a 2D trap density N_{T-th} inside the buffer-layer and in the fine proximity of 2DEG. Moreover, a quasi Fermi level for the trap centers inside the buffer-layer (E_{Ft}) is introduced, which determines the dominant band of trap centers ($E_{Ft} \pm 2kT$).

The fluctuation time constant of the thermally-activated trapping/de-trapping process to the states identified by the aforementioned 2D distribution can be calculated based on the modified Arrhenius characteristic in (4.1),

$$\tau_{th} = \upsilon_0{}^{-1} \exp\left(\frac{E_A}{kT}\right), \quad (5.10)$$

where E_A, the activation energy of the corresponding trap level, is defined as $E_0 - E_t$.

According to (5.10), the fluctuation time constant of the thermally-activated process is energy dependent. Therefore, a distribution function of the fluctuation time constant $g_{th}(\tau_{th})$ associated with a continuous band of trap centers in the proximity of the quasi Fermi level of the traps is considered. The noise power spectral density due to thermally-activated process is calculated by applying the same approach as (5.9) in the aforementioned three regions of the channel.

The normalized drain noise power spectral density due to thermally-activated process across the channel is calculated by

$$\frac{S_{I-TH}(f)}{{I_D}^2} = \frac{S_{N-TH}(f)}{N_{tot}^2} = \frac{1}{W^2\left(\int_0^{L_{gs}+L_g+L_{gd}} n_s(x)dx\right)^2} \times$$

$$\int_{E_{V-GaN}}^{E_{C-GaN}} \frac{4\,W\left(L_{gs}+L_g+L_{gd}\right)\,N_{T-th}(E) g_{th}\left(\tau_{th}(E)\right)\frac{d\tau_{th}}{dE}\,\tau_{th}(E) f_{t-th}\cdot[1-f_{t-th}]}{[1+4\pi^2 f^2 \tau_{th}^2(E)]}\,dE, \qquad (5.11)$$

where $S_{I-TH}(f)$ is the power spectral density due to thermally-activated process, $f_{t\text{-}th}$ is defined as the probability of a dominant energy level inside the buffer-layer being occupied using Fermi-Dirac statistics, and $g_{th}(\tau_{th}(E))$ is defined as the distribution function of time constants in the energy domain. It should be mentioned that the distribution functions follow the condition of

$$\int_{\tau_l}^{\tau_h} g_{th}(\tau_{th}) d\tau_{th} = 1. \qquad (5.12)$$

As pointed out in the discussions of sections 5.2.2.1 and 5.2.2.2, the calculation of the noise contributions of the thermally-activated and tunneling processes in terms of (5.9) and (5.11) requires information on the energies of the involved subband energy levels and 2DEG concentration. These essential pieces of information, with the inclusion of their variation along the length of channel, are calculated on the basis of the model presented in section 5.2.1 (Figure 5.2).

5.3 Results and discussions

The proposed model developed in section 5.2, has been applied to the new category of devices referred to as island-isolated AlGaN/GaN HFET. These devices were also experimentally explored in chapter 4.

The structures of these devices were presented in section 4.2. These technologically-defined parameters are introduced into the generic formalism presented in section 5.2, first in calculation of 2DEG characteristics, and subsequently in LFN calculations. Further details on the fabrication process and DC behavior of these devices can be found in [18]. As indicated in chapter 4, the reason for investigation of this device category is the extensive use of dry etching in the active region of the device and consequently higher chance of encountering $1/f^2$ LFN profiles. Under non-thermal equilibrium conditions of early linear regime of operation, the quasi Fermi level of the channel varies linearly across the three already identified regions of the channel. The calculated values of the threshold-voltage (which is in agreement with experimental results [18]) and the first and second subband energy levels in the gated-channel of this device are ~ - 3.9 V, ~ 0.30 eV, and 0.37 eV, respectively. The total 2DEG carrier-concentration (n_s) of the gated-channel at V_{GS} = 0 V is found to be ~1.2×10^{13} cm^{-2}, which is populated in the first and second subband energy levels with the ratio of approximately 4:1. An unintentional donor concentration in the order of 10^{14} cm^{-3} is assumed in the buffer-layer.

The tunneling process between the 2DEG and trap levels distributed in the barrier-layer can offer a fairly wide range of time constants necessary for providing the 1/f noise spectrum. On the contrary, in the thermally-activated process, only a narrow band of traps in the proximity of the quasi Fermi level ($E_{Ft} \pm 2kT$) are involved. Consequently, the noise

contribution of this process is expected to follow a Lorentzian as in (2.12). Concurrent existence of the 1/f spectrum caused by the tunneling process and the Lorentzian originating from the thermally-activated process of trapping/de-trapping of electrons will have the possibility of predicting the bulge signatures often observed in LFN spectra. It is assumed that there is no interaction between the trap centers involved in the two aforementioned mechanisms. The exact trap distribution in the barrier-layer is unknown. In this evaluation of the LFN contribution of the tunneling process, among a number of other distribution profiles the following hypothetical trap distribution profile inside the barrier-layer (i.e., AlGaN) is assumed,

$$N_{T-tn}(z,E) = C_1 \frac{(E-\Delta E_C/2)^2}{(\Delta E_C/2)^2} + C_2 \frac{(z-d/2)^2}{(d/2)^2} + C_3 \quad (5.13)$$

where, C_1, C_2, and C_3 are constants. Figure 5.4(a) illustrates an upward parabolic trap distribution according to (5.13) inside the barrier-layer. In this distribution, C_3 which represents the minimum trap distribution (occurring in the middle of the barrier and at energies about half the conduction-band discontinuity) is calculated through matching of the model to the experimental LFN data to be about 10^{17} $cm^{-3}eV^{-1}$. As speculated earlier, assumption of this distribution profile produced a 1/f noise spectrum. The tunneling-contributed LFN spectrum is also calculated on the basis of the assumption of three other trap distributions. Uniform (an average value in the order of 10^{17} $cm^{-3}eV^{-1}$) and two other trap distribution profiles according to 5.13 (Figure 5.4(b) and Figure 5.4(c)). The calculated LFN spectrum, based on these trap distributions, were observed to produce little difference. In all three distributions of Figure 5.4 the values of C_1 and C_2 have been selected so that a maximum of an order of magnitude variation in trap distribution will result.

According to the experimental results from the island-isolated HFETs, a $1/f^2$ bulge signature was observed with a corner frequency below 0.1 Hz at room temperature. Lack of observation of Random Telegraph Signal (RTS) noise in time domain observations of the drain LFN current, confirms that this $1/f^2$ signature is the result of a G-R noise. In evaluation of the LFN contribution of the thermally-activated process, a dominant single trap level in the buffer-layer is considered by defining $g_{th}(\tau_{th})$ in the form of a Gaussian distribution,

$$g_{th}(\tau_{th}) = \frac{1}{\sqrt{2\pi}\lambda} \exp\left[-\frac{1}{2}\left(\frac{\tau_{th}-\tau_0}{\lambda}\right)^2\right], \tag{5.14}$$

where λ is the standard deviation of the distribution function and τ_0 is the fluctuation time constant associated with the dominant trap level of the buffer-layer.

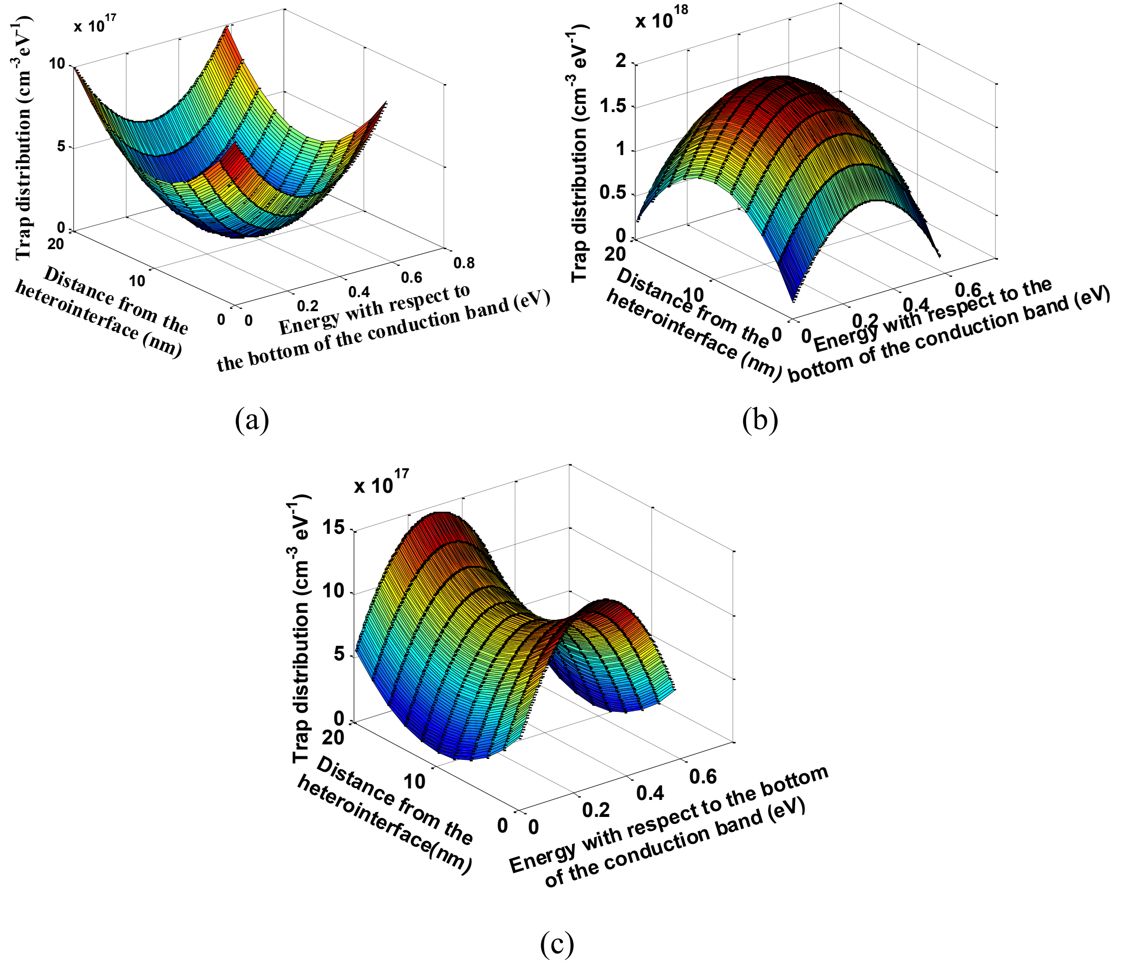

Figure 5.4 Hypothetical trap distributions in the barrier-layer (i.e., AlGaN) illustrating parabolic profiles as a function of energy with respect to the bottom of the conduction-band and distance with respect to the heterointerface. (a), (b) Parabolic trap distributions with a minimum and maximum value as a function of z and E, respectively. (c) Saddle-shape trap distribution as a function of z and E.

Whereas the $1/f^2$ was detected at room temperature, the bulge signature disappears into the 1/f spectrum with increasing the lattice temperature. The reason is that the corner frequency caused by a single/dominant trap level increases while the amplitude of the noise level reduces with increasing temperature.

Figure 5.5(a) illustrates the calculated contributions of tunneling and thermally-activated processes to LFN spectrum of an island-isolated HFET at room temperature which is biased at V_{GS} = -1 V and V_{DS} = 0.2 V. In agreement with the experimental observation of

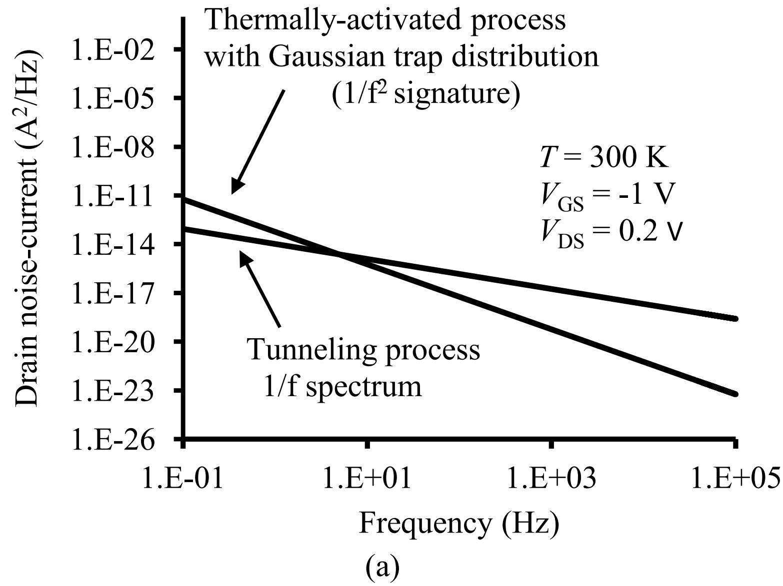

(a)

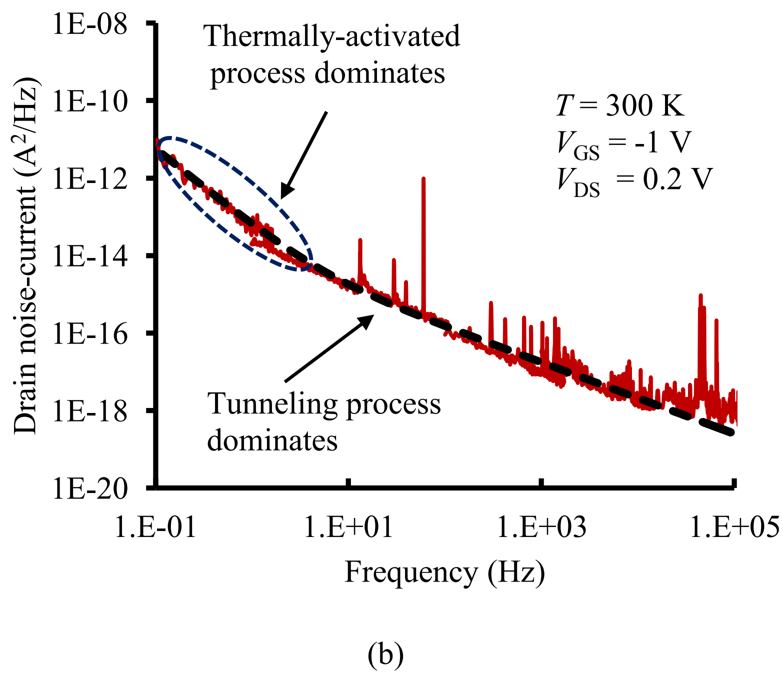

(b)

Figure 5.5 (a) Calculated LFN profiles according to the two processes of thermally-activated and tunneling. (b) Comparison of the simulation result (dashed-black line) and experimental data (red). Both figures belong to island-isolated device biased at V_{GS} = -1 V and V_{DS} = 0.2 V at room temperature.

the bulge signature, the value of the dominant trap level in the buffer-layer is taken as 1

eV with respect to the first subband energy level. The corresponding τ_{th} is calculated using (5.10). The total trap density of the buffer-layer is found to be 10^6 cm^{-2}. As illustrated in Figure 5.5(a), noise due to the thermally-activated process dominates at lower frequencies (resulting in a $1/f^2$ signature), whereas the tunneling process results in the 1/f spectrum at higher frequencies (f > 10 Hz at room temperature). Figure 5.5(b) illustrates a comparison between the theoretical model and experimental results.

Figure 5.6 shows the theoretical drain-noise current solely due to the thermally-activated process, for the same device and bias point as Figure 5.5 at elevated temperatures (i.e., T = 350, 400, and 450 K). As evident from Figure 5.6, the corner frequency of the G-R Lorentzian increases while the noise level of the $1/f^2$ signature decreases with elevated temperatures. As a result, the bulge signature of the thermally-activated process is

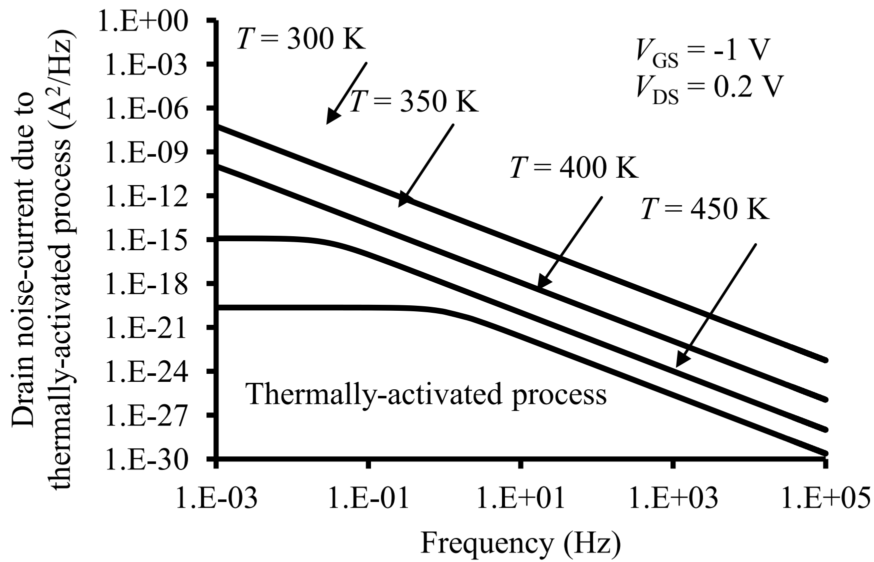

Figure 5.6 Calculated LFN contribution of thermally-activated process at elevated temperatures (i.e., T = 350, 400, and 450 K). The device and bias point are the same as in Figure 5.5.

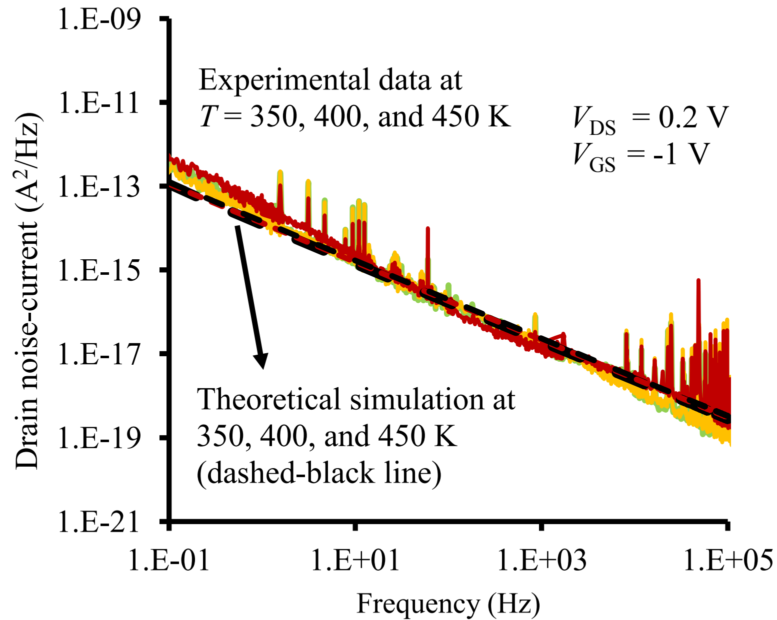

Figure 5.7 Comparison of theoretically calculated LFN spectrum (dashed black line) and experimental drain noise-current spectrum of the island-isolated HFET biased at V_{GS} = -1 V and V_{DS} = 0.2 V, at elevated temperatures (i.e., T = 350, 400, and 450 K).

masked by the tunneling mechanism at these elevated temperatures, which is also experimentally observed.

Considering the same device and bias points, Figure 5.7 shows the comparison between the experimental results and the theoretically calculated noise profiles at elevated temperatures. As illustrated in this figure, the theoretical results at elevated temperatures are in agreement with experimental data. Whereas the noise levels demonstrate an acceptable agreement, a relative mismatch between the frequency exponents (γ) of the experimental and theoretically-calculated profiles is observed. However, the frequency exponent of the theoretically-calculated profile, although smaller than the experimental results demonstrated in Figure 5.7 (i.e., 0.93 compared to the experimentally-observed value of about 1.16), is well within the range of variations of this factor among idential

devices. Due to device variability, such varitations among the experimentally-observed values of noise spectral density and frequency exponent are often enountered among AlGaN/GaN HFETs [83]. As shown in Figure 5.7, a relatively negligible change is detected in the level of the LFN spectrum for changing the temperature from 350 to 450 K. This result indicates that the 1/f spectrum is not very sensitive to temparature.

Moreover, the theoretical results are compared to the experimental data at different gate voltages of V_{GS} = 0 V (Figure 5.8 (a)) and V_{GS} = -2 V (Figure 5.8 (b)) for identical drain of 0.2 V at room temperature. Theoretical results show a good match with experimental data and predict both $1/f^2$ bulge signature and 1/f spectrum at room temperature.

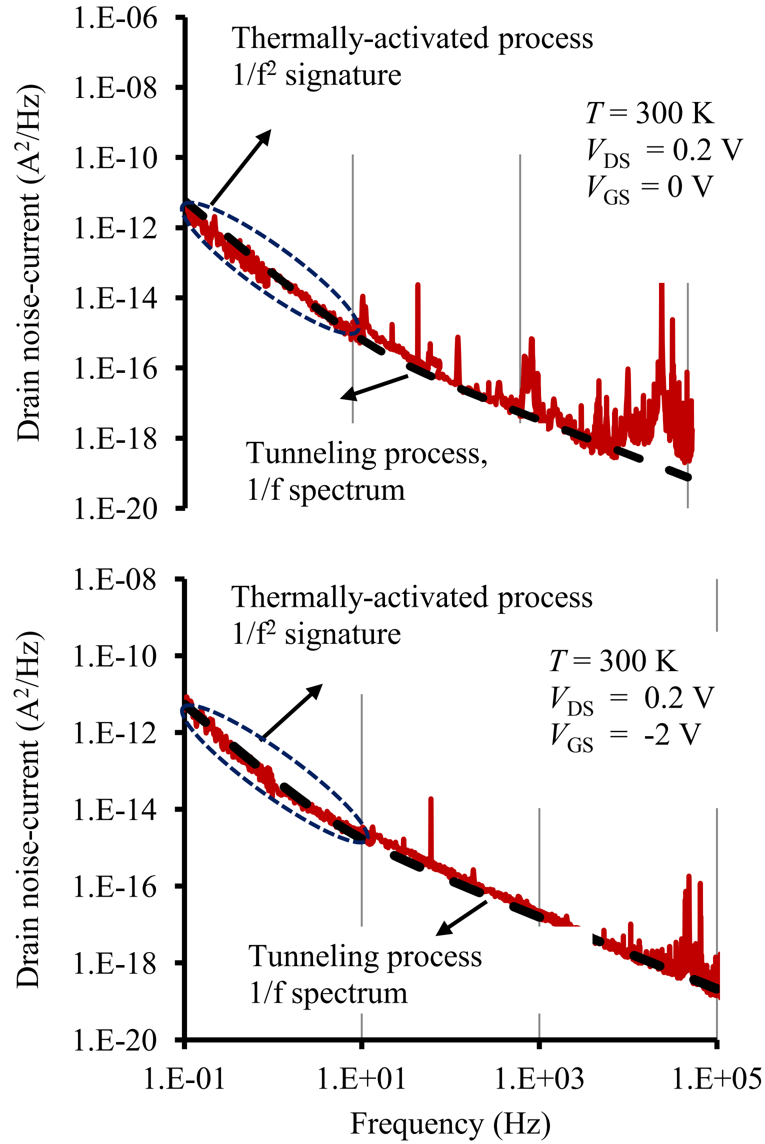

Figure 5.8 Comparison of the simulation results (dashed-black line) and experimental data (red) of drain noise-current at room temperature and two different bias points of V_{GS} = 0 V and -2 V with identical drain voltage of 0.2 V. All other parameters are the same as in Figure 5.5.

In addition to a normal distribution of $g_{th}(\tau_{th})$ identified in (5.14), a few arbitrary distribution functions (e.g., uniform, τ^{-1}, and τ^{-2}) are also considered in the evaluation of the LFN contribution of the thermally-activated process. The theoretical results

demonstrate that none of these specified distribution functions of $g_{th}(\tau_{th})$ are competent in terms of the matching of the theoretical LFN characteristics with experimental data (Figure 5.9).

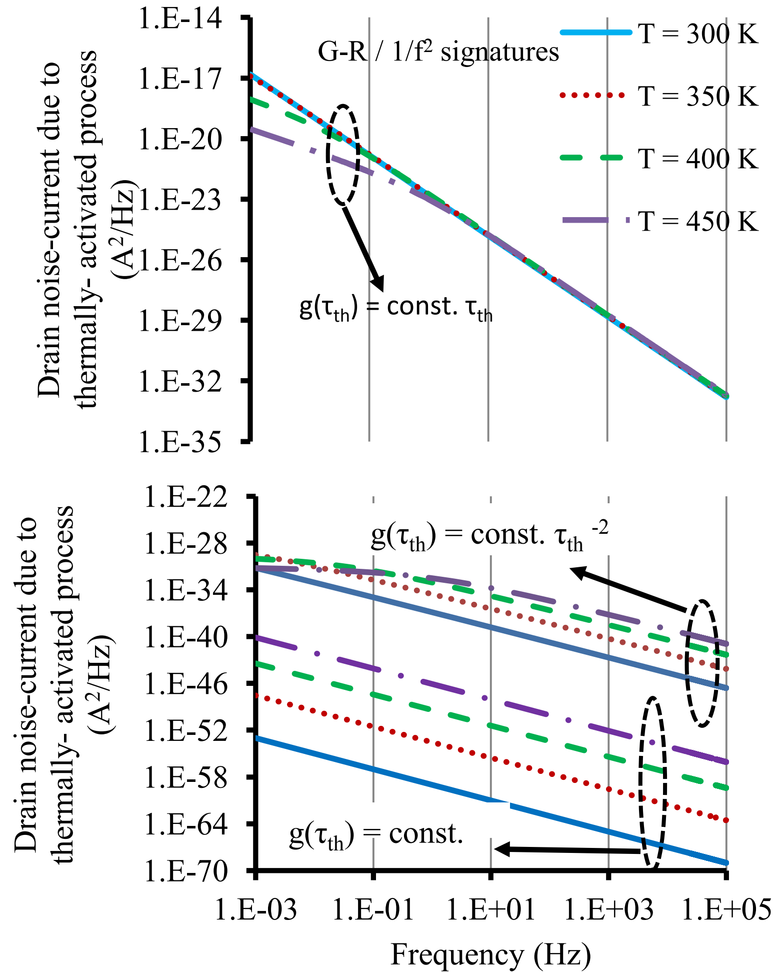

Figure 5.9 Calculated LFN contributions of the thermally-activated process at T = 300 (solid-blue), 350 (dotted-red), 400 (dashed-green), and 450 K (dashed-dotted purple) for the device biased at V_{GS} = -1 V and V_{DS} = 0.2 V. The calculations consider three different distribution functions for the buffer-layer trap levels.

5.4 Conclusion

A physics-based theoretical model is developed to investigate the low-frequency drain noise-current characteristics of polar AlGaN/GaN HFETs in early linear regime of operation by considering number fluctuation noise theory. The theoretical model is founded on the calculations of the first and second subband energy levels of the 2DEG carriers under thermal and non-thermal equilibrium based on variational method. Consequently, modeling of the carrier number fluctuation is realized by including both tunneling and thermal trapping/de-trapping of the 2DEG carriers from the two subband energy levels into and out of the trap sites of the barrier- and buffer-layer.

Fittings of the theoretical model with the experimental observations of island-isolated AlGaN/GaN HFETs at various temperatures reveal that the thermally-activated process of trapping/de-trapping of the 2DEG carriers to states in the buffer-layer is dominant in the frequency range where the $1/f^2$ bulge signature is observed, while the electron tunneling to states in the barrier-layer is responsible for 1/f noise spectrum. Based on temperature-dependent experimental observations, a relatively deep trap level is responsible for the $1/f^2$ bulge signature at room temperature. However, the bulge signature of the thermally-activated process is masked by the tunneling mechanism at elevated temperatures because the corner frequency of the G-R Lorentzian increases while the noise level of the $1/f^2$ signature decreases with elevated temperature.

Chapter 6

Concluding remarks, contributions, and future work suggestions

The research work of this thesis is focused on reliability-driven electrical characterization and physics-based modeling of AlGaN/GaN HFETs. The modeling and characterization of this category of devices attempt to not only improve the existing knowledge of fundamental heterojunction characteristics by proposing a generic physics-based model (chapter 3), but also evaluate and analyze potential reliability concerns of recently-proposed GaN technologies (chapter 4) [18]. In order to theoretically comprehend the physical phenomena capable of producing various experimentally acquired low-frequency noise signatures (e.g., G-R and 1/f spectra), the drain low-frequency noise characteristics is analyzed by physics-based modeling of the carrier transport in these

devices. This model pays close attention to carrier trapping/de-trapping into/out of the trap centers in the buffer- and barrier- layer through both thermally-activated and tunneling processes (chapter5).

6.1 Concluding remarks

In chapter 3, a generic variational-based model for calculating the fundamental characteristics of the quantum well including the first two subband energy levels, carrier-concentrations, and Fermi energy level of AlGaN/GaN heterojunctions is proposed. In addition, the 2DEG characteristic dependence on different technological parameters including barrier thickness, Al mole-fraction, background dopant concentration, and gate-source voltage are evaluated for gated AlGaN/GaN heterostructures. Theoretical results are validated by comparing the 2DEG characteristics with the results of self consistent method as well as experimental data reported in the literature. Moreover, the results of the variational method are compared with those obtained through applying the simplifying triangular quantum well approximation. This theoretical study has revealed that applying the triangular quantum well approximation to AlGaN/GaN heterojunctions does not lead to a realistic evaluation of the 2DEG characteristics. Therefore, from device modeling point of view, the conventional closed form relationships between subband energy levels and 2DEG concentrations applicable to GaAs heterojunctions are not suitable for modeling heterostructures with high carrier concentration such as AlGaN/GaN. In addition, according to the proposed approach, closed form empirical expressions for the dependency of E_0 and E_1 on n_s, for a full set of experimentally realizable heterostructures, are proposed.

In chapter 4, the variations of the low-frequency drain and gate noise-current characteristics of conventional mesa-isolated and newly-proposed fin- and island-isolated AlGaN/GaN HFETs were experimentally studied in a wide range of temperatures and in the early linear regime of operation. At room temperature, both mesa- and fin-isolated devices exhibit 1/f noise characteristics, whereas the island-isolated device has shown a Generation-Recombination bulge signature with a corner frequency below 0.1 Hz. At higher temperatures, this G-R signature was found to be masked by the 1/f noise characteristics. In addition, a G-R signature with a clear corner frequency of about 120 Hz was observed in the low-frequency gate noise-current characteristic of the island-isolated device at 150 K. This observation identified the existence of a relatively shallow trap level in the vicinity of the gate electrode. The appearance of the G-R bulge signatures in both drain and gate noise-current characteristics of island-isolated HFET are believed to be the result of the larger interface of the device electrodes to additionally dry-etched sidewalls of the islands and GaN surfaces. Based on the clear observation of the corner frequency in the gate noise-current of the island-isolated device at 150 K and the possible ICP-induced trap levels, a range of trapping/de-trapping time constants at 300 and 450 K are calculated using the modified Arrhenius characteristics. Accordingly, it is proposed that the deposition of a passivation layer can eliminate G-R signatures and hence improve the noise and high frequency performance of this novel category of devices.

In Chapter 5, According to the number fluctuation noise theory, a physics-based theoretical model is developed to investigate the low-frequency drain noise-current characteristics of polar AlGaN/GaN HFETs in early linear regime of operation. Linking

the theoretical model to the experimental observations of island-isolated AlGaN/GaN HFETs at various temperatures, the thermally-activated process of trapping/de-trapping of the 2DEG carriers to states in the buffer-layer is found to be dominant in the frequency range where $1/f^2$ bulge signature is observed, while the electron tunneling to states in the barrier-layer is found responsible for 1/f noise spectrum. Based on temperature-dependent experimental observations, a relatively deep trap level is found responsible for the $1/f^2$ bulge signature at room temperature. Accordingly, a normal distribution of fluctuation time constants associated with the thermally-activated process, which peaks at this relatively deep trap level, is found capable of predicting the experimental results at different temperatures.

6.2 Contributions

Chapter 3:

This work provides a comprehensive generic approach for modeling the fundamental 2DEG characteristics of III-nitride-based devices, which can be plugged into models and simulation tools used in analysis of these devices.

The contributions of this work include the followings,

- Developed a physics-based model for calculating first two subband energy levels of various gated $Al_xGa_{1-x}N$/GaN heterojunctions by the variational method.
- The 2DEG characteristics of various gated $Al_xGa_{1-x}N$/GaN heterostructures are modeled and analyzed.
- The applicability of triangular approximation in this material system is evaluated.

- Closed form empirical expressions are developed for the calculations of 2DEG concentrations.

Chapter 4:

In this task, the reliability of two recently-proposed GaN-based devices (i.e., proposed in [18]) is investigated by the means of low-frequency noise as an ultra sensitive spectroscopy tool. According to this investigation, an extra step in the fabrication process is proposed to alleviate the detected concern based on the analysis of low-frequency noise signatures.

The main contributions of this work are as follows,

- The low-frequency noise performance of two novel GaN technologies is investigated.
- Observed G-R signatures in gate and drain noise of island-isolated HFETs are reported.
- A range of relevant time constants is speculated for the island-isolated HFETs.
- The need for employing an extra passivation step for island-isolated HFETs is proposed.

Chapter 5:

Founded on the proposed model in chapter 3, a low-frequency noise model for the drain noise-current is proposed in this work, which takes into account the two most accepted mechanisms of carrier number fluctuation theory (i.e., tunneling and thermally-activated processes). This work intended to shed light on the origins of different signatures of low-frequency noise spectra.

The major contributions of this chapter are as follows,

- A generic low-frequency drain noise-current model is developed by incorporating both tunneling and thermally-activated mechanisms.

- The developed low-frequency noise model is applied to recently-proposed GaN-based HFETs.
- It is found that the thermally-activated process is responsible for $1/f^2$ noise spectrum, whereas the $1/f^\gamma$ noise stems from the tunneling process.
- According to the theoretical model, a relatively deep trap level in the buffer-layer is found to be responsible for the emergence of G-R bulge signature at very low-frequency range.

6.3 Future work suggestions

The following future works are suggested for the continuing study of III-nitride HFETs,

1. Study of correlations between low-frequency gate and drain noise characteristics

As mentioned in section 6.2, a part of this research work was dedicated to thorough investigations of the low-frequency noise-current characteristics of recently-proposed AlGaN/GaN HFETs that were introduced in [18]. However, the correlations between low-frequency gate and drain noise-current characteristics of III-nitride HFETs are yet to be further elaborated. Such an experimental investigation can be considered as a complementary study.

2. Physics-based modeling of low-frequency gate noise characteristics

It was pointed out in section 1.4, that the existence of physics-based models of low-frequency noise characteristics of a device is helpful in further understanding of the origins of experimentally acquired low-frequency noise signatures of a device. Such a theoretical investigation of low-frequency gate noise-current in combination with

physics-based studies of drain noise-current characteristics can further develop the existing knowledge of this detrimental phenomenon in FETs.

3. InN-based Devices

➢ Polarization-engineered $Al_yIn_xGa_{1-x-y}N/GaN$ HFETs

As mentioned earlier in chapters 1 and 4, due to large polarization effect, III-nitride based devices normally operate in depletion-mode. In order to realize enhancement-mode devices in this technology, reduction of the carrier-concentration of the channel is required. The modification of the carrier-concentration can be achieved through either appropriate device processing or design of the epitaxial layers, which were pointed out in chapter 1. It was also mentioned in section 1.4 that a recently-proposed approach introduces the use of quaternary III-nitride semiconductor as the barrier-layer. In case of AlGaN/GaN HFET, the AlGaN barrier-layer can be replaced by a quaternary alloy layer of AlInGaN, which in turn modifies the polarization vectors and reduces the sheet charge. However, few theoretical models have been so far applied to this recently-proposed category of devices. The proposed model can be applied to such novel device structures in order to further investigate the basic device parameters with respect to the device technological aspects and hence find the optimum physical properties of the device.

➢ AlInN/GaN HFETs

AlInN/GaN HFETs have attracted a great deal of attention for the high frequency/high power applications due to their superior transconductance values and high current-density. The major difference between this material system and AlGaN/GaN heterostructures is that AlInN can be grown lattice-matched to GaN, which provides a strain-free barrier. The large spontaneous polarization in this material system can

compensate the piezoelectric polarization and hence develop a 2DEG with a concentration as large as that of AlGaN/GaN system. This material system, however, is still immature compared to AlGaN/GaN HFETs in terms of developed theoretical model and investigations of the 2DEG characteristics versus technological aspects including barrier thickness and Al mole-fraction.

4. AlGaN/GaN/AlGaN double HFETs

Since the introduction of polar AlGaN/GaN HFETs, considerable efforts have been dedicated to the study of single heterojunction HFETs. Both theoretical and experimental parts of this thesis were also focused on single heterojunction AlGaN/GaN HFETs.

Due to the lower potential barrier of GaN, formed at the heterointerface of a single AlGaN/GaN heterojunction (referred to as insufficient confinement), the 2DEG carriers are likely to overflow from the quantum well to the buffer-layer, degrade the two dimensional confinement, and hence degrade the carrier transport of the device. This phenomenon is more pronounced for higher 2DEG concentration. One approach to alleviate this problem is using AlGaN/GaN/AlGaN double heterojunctions. The additional barrier-layer underneath the channel-layer helps to improve the carrier confinement and therefore reduce the carrier overflow to the channel-layer. Modifying the proposed theoretical model to consider the double AlGaN/GaN HFET will be a novel contribution.

Bibliography

[1] U. K. Mishra and J. Singh, Semiconductor device physics and design, Springer, 2008.

[2] A. Lidow, J. Strydom, M. de Rooij, and Y. Ma, GaN transistors for efficient power conversion, The eGaN FET journey continues, Power Conversion Publications, El Segundo CA, 2012.

[3] M. Razeghi and M. Henini, Optoelectronic devices: III-Nitrides, Elsevier, 2004.

[4] http://www.triquint.com/products/all/standard-products/gan-fets, 2013.

[5] F. Bernardini, V. Fiorentini, and D. Vanderbilt, "Spontaneous polarization and piezoelectric constants of III-V nitrides," *Phys. Rev. B*, vol. 56, no. 16, pp. R10024-R10027, Oct. 1997.

[6] O. Ambacher, B. Foutz, J. Smart, J. R. Shealy, N. G. Weimann, K. Chu, M. Murphy, A. J. Sierakowski, W. J. Schaff, L. F. Eastman, R. Dimitrov, A. Mitchell, and M. Stutzmann, "Two dimensional electron gases induced by spontaneous and piezoelectric polarization in undoped and doped AlGaN/GaN heterostructures," *J. Appl. Phys.*, vol. 87, no. 1, pp. 334-344, Jan. 2000.

[7] http://www.gansystems.com/why_gallium_nitride.php, 2013.

[8] M. E. Levinshtein, S. L. Rumyantsev, and M. S. Shur, Properties of advanced semiconductor materials, John Wiley and Sons, 2001.

[9] Meneghesso, G. Verzellesi, F. Danesin, F. Rampazzo, F. Zanon, A. Tazzoli, M. Meneghini, and E. Zanoni, "Reliability of GaN high-electron-mobility transistors: state of the art and perspectives," *IEEE Trans. Device Mater. Rel.*, vol. 8, no. 2, pp. 332-343, June 2008.

[10]. K. Mishra, P. Parikh, and Y.-F. Wu, "AlGaN/GaN HEMTs—An overview of device operation and applications," *Proc. IEEE*, vol. 90, no. 6, pp. 1022-1031, June 2002.

[11] N. Tripathi, V. Jindal, F. Shahedipour, S. Rajan, and A. Vert, "Turn-on voltage engineering and enhancement mode of operation of AlGaN/GaN high electron mobility transistor using multiple heterointerfaces," *Solid-State Electronics*, vol. 54, no. 11, pp. 1291-1294, Nov. 2010.

[12] T. Mizutani, M. Ito, S. Kishimoto, and F. Nakamura, "AlGaN/GaN HEMTs with thin InGaN cap layer for normally off operation," *IEEE Electron Device Lett.*, vol. 28, no. 7, pp. 549-551, July 2007.

[13] W. Lanford, T. Tanaka, Y. Otoki, and I. Adesida, "Recessed-gate enhancement-mode GaN HEMT with high threshold-voltage," *Electronics Lett.*, vol. 41, no. 7, pp. 449-450, Mar. 2005.

[14] Y. Cai, Y. Zhou, K. Lau, and K. Chen, "High performance enhancement mode AlGaN/GaN HEMTs using fluoride-based plasma treatment," *IEEE Electron Device Lett.*, vol. 26, no. 7, pp. 435-437, July 2005.

[15] R. Xuan, W. H. Kuo, C. W. Hu, S. F. Lin, and J. F. Chen, "Enhancing threshold-voltage of AlGaN/GaN high electron mobility transistors by nano rod structure: from depletion to enhancement mode," *Appl. Phys. Lett.*, vol. 101, no. 11, pp. 112105-1–112105-3, Sep. 2012.

[16] R. Chu, Z. Chen, S. P. DenBaars, and U. K. Mishra, "V-gate GaN HEMTs with engineered buffer for normally off operation," *IEEE Electron Device Lett.*, vol. 29, no. 11, pp. 1184-1186, Nov. 2008.

[17] H. Hahn, B. Reuters, A. Wille, N. Ketteniss, F. Benkhelifa, O. Ambacher, H. Kalisch, and A. Vescan, "First polarization-engineered compressively strained AlInGaN barrier enhancement-mode MISHFET," *Semicond. Sci. Technol.*, vol. 27, no. 5, pp. 1-6, Mar. 2012.

[18] P. Valizadeh and B. AlOtaibi, "Fin- and Island-Isolated AlGaN/GaN HFETs," *IEEE Trans. Electron Devices*, vol. 58, no. 5, pp. 1404-1407, May 2011.

[19] S. Khandelwal, N. Goyal, and T. A. Fjeldly, "A Physics-based analytical model for 2DEG charge density in AlGaN/GaN HEMTs devices," *IEEE Trans. Electron Devices*, vol. 58, no. 10, pp. 3622-3625, Oct. 2011.

[20] S. Khandelwal, Y. S. Chauhan, and T. A. Fjeldly, "Analytical modeling of surface-potential and intrinsic charges in AlGaN/GaN HEMT devices," *IEEE Trans. Electron Devices*, vol. 59, no. 10, pp. 2856-2860, Oct. 2012.

[21] K.-S. Lee, D.-H. Yoon, S.-B. Bae, M.-R. Park, and G.-H. Kim, "Self-consistent subband calculations of AlGaN/GaN single heterojunctions," *ETRI J.*, vol. 24, no. 4, pp. 270-279, Aug. 2002.

[22] K.-S. Lee, "Variational method for the lowest conduction subband of undoped AlGaN/GaN single heterojunctions," *J. Korean Phys. Soc.*, vol. 45, no. 6, pp. 1683-1686, Dec. 2004.

[23] L. K. J. Vandamme, "Noise as a diagnostic tool for quality and reliability of electron devices," *IEEE Trans. Electron Devices*, vol. 41, no. 11, pp. 2176-2187, Nov. 1994.

[24] M. E. Levinshtein and S. L. Rumyantsev, "Noise spectroscopy of local levels in semiconductors," *Semicond. Sci. Technol.*, vol. 9, no. 6, pp. 1183-1189, June 1994.

[25] N. V. Dyakonova, M. E. Levinshtein, S. Conteras, W. Knap, B. Beaumont, and P. Gilbart, “Low frequency noise in n-GaN,” *Semiconductors*, vol. 32, no. 3, pp. 257-260, Mar. 1998.

[26] J. Peransin, P. Vignaud, D. Rigaudand, and L. K. J. Vandamme, “1/f noise in MODFETs at low drain biases,” *IEEE Trans. Electron Devices*, vol. 37, no. 11, pp. 2250-2253, Oct. 1990.

[27] Z. C. Feng (Ed), III-Nitride semiconductor material, Imperial College Press, 2006.

[28] N. Grandjean and J. Massies, “GaN and Al_x Ga_{1-x} N molecular beam epitaxy monitored by reflection high-energy electron diffraction,” *App. Phys. Lett.*, vol. 71, no. 13, pp. 1816-1818, July 1997.

[29] S. M. Hubbard, “Metalorganic vapor phase epitaxy (MOVPE) growth and characterization of III-Nitride heterostructures for applications in electronic devices,” Ph.D. dissertation, Dept. Elect. Eng., The University of Michigan, 2005.

[30] S. M. Hubbard, G. Zhao, D. Pavlidis, W. Sutton, and E. Cho, “High-resistivity GaN buffer templates and their optimization for GaN-based HFETs,” *J. Crystal Growth*, vol. 284, pp. 297-305, Nov. 2005.

[31] Z. H. Feng, B. Liu, F. P. Yuan, J. Y. Yin, D. Liang, X. B. Li, Z. Feng, K, W. Yang, and S. J. Cai, “Influence of Fe-doping on GaN grown on sapphire substrates by MOCVD,” *J. Crystal Growth*, vol. 309, no. 1, pp. 8-11, Nov. 2007.

[32] F. J. Xu, J. Xu, B. Shen, Z. L. Miao, S. Huang, L. Lu, Z. J. Yang, Z. X. Qin, and G. Y. Zhang, “Realization of high-resistance GaN by controlling the annealing pressure of the nucleation layer in metal-organic chemical vapor deposition,” *J. Thin Solid Films*, vol. 517, no.2 , pp. 588-591, Nov. 2008.

[33] M. Boćkowski, I. Grzegory, B. Łucznik, T. Sochacki, M. Kryśko, P. Strąk, I. Dzięcielewski, E. Litwin-Staszewska, and S. Porowski, “High nitrogen pressure solution growth of bulk GaN in “feed-seed” configuration,” *Phys. Status Solidi A*, vol. 208, no. 7, pp. 1507-1510, May 2011.

[34] M. Boćkowski, B. Łucznik, T. Sochacki, G. Nowak, E. Litwin-Staszewska, and I. Grzegory, “High nitrogen pressure solution growth of GaN in multi feed seed configuration,” *Phys. Status Solidi C*, vol. 9, no. 3-4, pp. 453-456, Feb. 2012.

[35] F. Bernardini, V. Fiorentini, and D. Vanderbilt, “Accurate calculation of polarization-related quantities in semiconductors,” *Phys. Rev. B*, vol. 63, no. 19, pp. 193201-1–193201-4, Apr. 2001.

[36] W. Q. Chen and S. K. Hark, “Strain induced effects in (111) oriented InAsP/InP and InGaAs/InAlAs quantum wells on InP substrates,” *J. Appl. Phys.*, vol. 77, no. 11, pp. 5747-5750, June 1995.

[37] A. D. Bykhovski, B. L. Gelmont, and M. S. Shur, “Elastic strain relaxation and piezoeffect in GaN-AlN, GaN-AlGaN and GaN-InGaN superlattices,” *J. Appl. Phys.*, vol. 81, no. 9, pp. 6332-6338, May 1997.

[38] O. Ambacher, J. Smart, J. R. Shealy, N. G. Weimann, K. Chu, M. Murphy, W. J. Schaff, L. F. Eastman, R. Dimitrov, L. Wittmer, M. Stutzmann,W. Rieger, and J. Hilsenbeck, “Two-dimensional electron gases induced by spontaneous and piezoelectric polarization charges in N- and Ga-face AlGaN/GaN heterostructures,” *J. Appl. Phys.*, vol. 85, no. 6, pp. 3222-3233, Mar. 1999.

[39] H. Angerer, D. Brunner, F. Freudenberg, O. Ambacher, M. Stutzmann, R. Höpler, T. Metzger, E. Born, G. Dollinger, A. Bergmaier, S. Karsch, and H.-J. Körner, “Determination of Al mole-fraction and the bandgap bowing of epitaxial $Al_xGa_{1-x}N$ films,” *Appl. Phys. Lett.*, vol. 71, no. 11, pp. 1504-1506, Sep. 1997.

[40] F. Bernardini and V. Fiorentini, “Nonlinear macroscopic polarization in III-V nitride alloys,” *Phys. Rev. B.*, vol. 64, no. pp. 085207-1–085207-7, Aug. 2001.

[41] V. Fiorentini, F. Bernardini, and O. Ambacher, “Evidence for nonlinear macroscopic polarization in III-V nitride alloy heterostructures,” *Appl. Phys. Lett.*, vol. 80, no. 7, pp. 1204-1207, Jan. 2002.

[42] M. von Haartman and M. Östling, Low-frequency noise in advanced MOS devices, Springer, 2007.

[43] C. T. Sah, “Theory of low-frequency generation noise in junction-gate field effect transistors,” *Proc. IEEE*, vol. 52, no. 7, pp. 795-814, 1964.

[44] L. K. J. Vandamme and F. N. Hooge, “What do we certainly know about 1/f noise in MOSTs?,” *IEEE Trans. Electron Devices*, vol. 55, no. 11, pp. 3070-3085, Nov. 2008.

[45] A. L. McWhorter, “1/f noise and germanium surface properties,” *in semiconductor surface Physics*, University of Pennsylvania, Philadelphia, pp. 207-228, 1957.

[46] F. N. Hooge, T. G. M. Kleinpenning, and L. K. J. Vandamme, “Experimental studies on 1/f noise,” *Rep. Prog. Phys.*, vol. 44, no. 5, pp. 479-532, May 1981.

[47] A. Van der Ziel, “Unified presentation of 1/f noise in electronic devices: fundamental 1/f noise sources,” *Proc. IEEE*, vol. 76, no. 3, pp. 233-258, Mar. 1988.

[48] S. Christensson, I. Lundström, and C. Sevensson, “Low frequency noise in MOS transistors-I theory,” *Solid-State Electronics*, vol. 11, no. 9, pp. 797-812, Sep. 1968.

[49] J. Sikula and M. Levinshtein, Advanced experimental methods for noise research in nanoscale electronic devices, Kiuwer Academic Publishers, 2004.

[50] S. L. Rumyantsev, N. Pala, M. S. Shur, E. Borovitskaya, A. P. Dimitriev, M. E. Levinshtein, R. Gaska, M. A. Khan, J. Yang, X. Hu, and G. Simin, "Generation-Recombination noise in GaN/AlGaN heterostructure field effect transistors*," IEEE Trans. Electron Devices*, vol. 48, no. 3, pp. 530-534, Mar. 2001.

[51] A. Madan, J. D. Cressler, and S. J. Koester, "Low frequency noise in buried-channel SiGe n-MODFETs," *Solid-State Electronics*, vol. 53, no. 8, pp. 901- 904, Aug. 2009.

[52] R. Jos, "A semi-analytical two dimensional model for AlGaN/GaN high-electron-mobility-transistor Schottky currents at high reverse voltages," *J. Appl. Phys.*, vol. 114, no. 7, pp. 074512-1–074512-9, Aug. 2013.

[53] H. C. Chiu, C. H Chen, C. W. Yang, H. L. Kao, F. H. Huang, S. W. Peng, and H. K. Lin, "Highly thermally stable in situ SiN_x passivation AlGaN/GaN enhancement-mode high electron mobility transistors using TiW refractory gate structure," *J. Vac. Sci. Technol. B*, vol. 31, no. 5, pp. 051212-1–051212-4, Sep. 2013.

[54] B. K. Ridley, Electrons and Photons in Semiconductor Multilayers, Cambridge University, Press p. 50, 1997.

[55] T. Ando, A. B. Fowler and F. Stern, "Electronic properties of two-dimensional systems," *Rev. Mod. Phys.*, vol. 54, no. 2, pp. 437-672, Apr. 1982.

[56] D. Ji, Y. Lu, B. Liu, and J. Liu, "Converse piezoelectric effect induced misfit dislocation scattering in metal/AlGaN/GaN heterostructures," *Appl. Phys. Lett.*, vol. 102, no. 13, pp. 132106-1–132106-3, Apr. 2013.

[57] F. Manouchehri, P. Valizadeh, and M. Z. Kabir, "Determination of subband energies and 2DEG characteristics of $Al_xGa_{1-x}N$/GaN heterojunctions using variational method," *J. Vac. Sci. Technol. A*, vol. 32, no. 2, pp. 021104-1–021104-8, Mar. 2014.

[58] A. Fischer, H. Kühne, B. Roos, and H. Richter, "Elastic strain relaxation in patterned heteroepitaxial structures," *Semicond. Sci. Technol.*, vol. 9, no. 12, pp. 2195-2198, July 1994.

[59] P. Valizadeh and D. Pavlidis, "Effects of RF and DC stress on AlGaN/GaN MODFETs: a low frequency noise-based investigation," *IEEE Trans. Device Mater. Rel.*, vol. 5, no. 3, pp. 555-563, Sep. 2005.

[60] P. Valizadeh, "High-temperature very low frequency noise-based investigation of slow transients in AlGaN/GaN MODFETs," *IEEE Trans. Device Mater. Rel.*, vol. 8, no. 2, pp. 265-271, June 2008.

[61] L. Fang, S. Bo, L. L. Wu, L. X. Yu, W. Ke, X. F. Jun, W. Yan, M. Nan, and H. Jun, "Identification and elimination of inductively coupled plasma-induced defects in $Al_xGa_{1-x}N$/GaN heterostructures," *Chinese Phys. B*, vol. 20, no. 7, pp. 1-6, Mar. 2011.

[62] H. K. Cho, F. A. Khan, I. Adesida, Z-Q Fang, and D. C. Look, "Deep level characteristics in n-GaN with inductively coupled plasma damage," *J. Phys D: Appl. Phys.*, vol. 41, no. 15, pp. 155314-1–155314-4, July 2008.

[63] Z. -Q. Fang, D. C. Look, X. -L. Wang, J. Han, F. A. Khan, and I. Adesida, "Plasma etching-enhanced deep centers in n-GaN grown by metalorganic chemical-vapor deposition," *Appl. Phys. Lett.*, vol. 82, no. 10, pp. 1562-1564, Mar. 2003.

[64] K. J. Choi, H. W. Jang, and J. L. Lee, "Observation of inductively coupled-plasma-induced damage on n-type GaN using deep-level transient spectroscopy," *Appl. Phys. Lett.*, vol. 82, no. 8, pp. 1233-1235, Feb. 2003.

[65] C. Kayis, C. Y. Zhu, M. Wu, X. Li, Ü. Özgür, and H. Markoç, "Field-assisted emission in AlGaN/GaN heterostructure field-effect transistors using low-frequency noise technique," *J. Appl. Phys.*, vol. 109, no. 8, pp. 084522-1–084522-5, Apr. 2011.

[66] R. Vetury, N. Q. Zhang, S. Keller, and U. K. Mishra, "The impact of surface states on the DC and RF characteristics of AlGaN/GaN HFETs," *IEEE Trans. Electron Devices*, vol. 48, no. 3, pp. 560–566, Mar. 2001.

[67] O. Mitrofanov and M. Manfra, "Mechanisms of gate lag in GaN/AlGaN/GaN high electron mobility transistors," *Superlattices Microstruct.*, vol. 34, no. 1-2, pp. 33-53, Dec. 2003.

[68] K. Horio and A. Nakajima, "Buffer-trap and surface-state effects on gate lag in AlGaN/GaN HEMTs," *J. Phys. Status Solidi C*, vol. 7, no. 7-8, pp. 1931-1933, July 2010.

[69] J. Bernát, R. Pierobon, M. Marso, J. Flynn, G. Brandes, G. Meneghesso, E. Zanoni, and P. Kordoš, "Low current dispersion and low bias-stress degradation of unpassivated GaN/AlGaN/GaN/SiC HEMTs," *J. Phys. Status Solidi C*, vol. 2, no. 7, pp. 2676-2679, May 2005.

[70] B. M. Green, V. Tilak, V. S. Kaper, J. A. Smart, J. R. Shealy, and L. F. Eastman, "Microwave power limits of AlGaN/GaN HEMTs under pulsed-bias conditions," *IEEE Trans. Microwave Theory Tech.*, vol. 51, no. 2, pp. 618-623, Feb. 2003.

[71] F. Manouchehri, P. Valizadeh, and M. Z. Kabir, "Temperature-dependent investigation of low frequency noise characteristics of mesa-, fin-, and island-isolated AlGaN/GaN HFETs," *Solid-State Electronics*, vol. 89, pp. 1-6, July 2013.

[72] J. Graffeuil, "Low-frequency noise of GaAs FETs," *Electronics Lett.*, vol. 17, no. 11, pp. 387, May 1981.

[73] S. Kuglar, "Generation-recombination noise in the saturation regime of MODFET structures," *IEEE Trans. Electron Devices*, vol. 35, no. 5, pp. 623-628, May 1988.

[74] P. Viktorovitch, P. Rojo-Romeo, J. L. Leclercq, X. Letartre, J. Tardy, M. Oustric, and M. Gendry, "Low frequency noise sources in InAlAs/InGaAs MODFET's," *IEEE Trans. Electron Devices*, vol. 43, no. 12, pp. 2085-2100, Dec. 1996.

[75] L. Dobrzanski and Z. Wolosiak, "On the origin of low frequency noise in GaAs metal–semiconductor field-effect transistors," *J. Appl. Phys.*, vol. 87, no. 1, pp. 517-521, Jan. 2000.

[76] S. Mohammadi and D. Pavlidis, "A nonfundamental theory of low-frequency noise in semiconductor devices," *IEEE Trans. Electron Devices*, vol. 47, no. 11, pp. 2009-2017, Nov. 2000.

[77] Y. Chen, C. M. VanVliet, G. L. Larkins, and H. Markoç, "Generation-recombination noise in nongated and gated $Al_xGa_{1-x}As$/GaAs TEGFETs in the range 1 Hz to 1 MHz," *IEEE Trans. Electron Devices*, vol. 47, no. 11, pp. 2045-2053, Nov. 2000.

[78] S. L. Rumyantsev, Y. Deng, E. Borovitskaya, A. P. Dmitriev, W. Knap, N. Pala, and M. S. Shur, "Low frequency noise in GaN/AlGaN heterostructure field effect transistors at cryogenic temperatures," *J. Appl. Phys.*, vol. 92, no. 8, pp. 4726-4730, Oct. 2002.

[79] A. P. Dmitriev, M. E. Levinshtein, S. L. Rumyantsev, and M. S. Shur, "Tunneling mechanism of the 1/f noise in GaN/AlGaN heterojunction field-effect transistors," *J. Appl. Phys.*, vol. 97, no. 12, pp. 123706-1–123706-4, June 2005.

[80] F. Manouchehri, P. Valizadeh, and M. Z. Kabir, "Non-fundamental low frequency noise theory: Drain noise-current modeling of AlGaN/GaN HFETs," *Proc. 21st Int. Conf. Noise and Fluctuations (ICNF)*, pp. 220-222, June 2011.

[81] F. Manouchehri, P. Valizadeh, and M. Z. Kabir, "Physics-based analysis of low frequency drain noise-current in $Al_xGa_{1-x}N$/GaN HFETs," *J. Phys. D: Appl. Phys.*, vol. 47, pp. 085104-1–085104-8, Feb. 2014.

[82] S. A. Mahmood, M. Z. Kabir, O. Tousignant, H. Mani, J. Greenspan, and P. Botka, "Dark current in multilayer amorphous selenium x-ray imaging detectors," *Appl. Phys. Lett.*, vol. 92, no. 22, pp. 223506-1–223506-3, June 2008.

[83] P. Valizadeh, D. Pavlidis, K. Shiojima, T. Makimura, and N. Shigekawa, "Low frequency noise of AlGaN/GaN MODFETs: A comparative study of surface, barrier and heterointerface effects," *Solid-State Electronics*, vol. 49, no. 8, pp. 1352-1360, Aug. 2005.